The Bi-directional Spatial Spectrum for MIMO Radar and Its Applications

by

Jason Yu

Department of Electrical and Computer Engineering
Duke University

Date: _____

Approved:

_____
Jeffrey Krolik, Supervisor

_____
Loren Nolte

_____
Matthew Reynolds

_____
Geoffrey San Antonio

_____
Olaf Von Ramm

Dissertation submitted in partial fulfillment of
the requirements for the degree of Doctor of Philosophy in the Department of
Electrical and Computer Engineering in the Graduate School
of Duke University

2013

ABSTRACT

The Bi-directional Spatial Spectrum for MIMO Radar and Its Applications

by

Jason Yu

Department of Electrical and Computer Engineering
Duke University

Date: _____

Approved:

_____
Jeffrey Krolik, Supervisor

_____
Loren Nolte

_____
Matthew Reynolds

_____
Geoffrey San Antonio

_____
Olaf Von Ramm

An abstract of a dissertation submitted in partial
fulfillment of the requirements for the degree
of Doctor of Philosophy in the Department of
Electrical and Computer Engineering in the Graduate School
of Duke University

2013

Abstract

Radar systems have long applied electronically-steered phased arrays to discriminate returns in azimuth angle and elevation angle. On receiver arrays, beamforming is performed after reception of the data, allowing for many adaptive array processing algorithms to be employed. However, on transmitter arrays, up until recently pre-determined phase shifts had to applied to each transmitter element before transmission, precluding adaptive transmit array processing schemes. Recent advances in multiple-input multiple-output radar techniques have allowed for transmitter channels to separated after data reception, allowing for virtual non-causal ("after-the-fact") transmit beamforming. The ability to discriminate in both direction-of-arrival and direction-of-departure allows for the novel ability to discriminate line-of-sight returns from multipath returns. This works extends the concept of virtual non-causal transmit beamforming to the broader concept of a bi-directional spatial spectrum, and describes application of such a spectrum to applications such as spread-Doppler multipath clutter mitigation in ground-vehicle radar, and calibration of a receiver array of a MIMO system with ground clutter only. Additionally, for this work, a low-power MIMO radar testbed was developed for lab testing of MIMO radar concepts.

Contents

List of Tables

List of Figures

List of Abbreviations and Symbols

Symbols

Many mathematical equations appear throughout this dissertation and a plethora of mathematical variables appear within them. The variables will be defined as they appear in the text. The typesetting of the letters within a mathematical equation defines whether the variable is a scalar value, a vector value, a matrix, or a standard mathematical function.

a	A letter in italics represents a scalar value
$\mathbf{a}$	A bold-face, lower-case letter represents a vector
$\mathbf{A}$	A bold-face, upper-case letter represents a matrix
$\mathrm{abs}(x)$	A non-italic, non-boldface set of letters represents a standard mathematical function, such as sine (sin), cosine (cos), minimum (min), maximum (max), etc.

Abbreviations

SIMO	single-input multiple-output
MIMO	multiple-input multiple-output
GMTI	ground moving target indicator
RF	radio frequency
DoA	direction of arrival
DoD	direction of departure
STAP	space-time adaptive processing

LFM	linear frequency modulated
WRI	waveform repetition interval
WRF	waveform repetition frequency
CPI	coherent processing interval
CIT	coherent integration time
SLO-MO	slow-time MIMO
VSWR	voltage standing wave ratio
RCS	radar cross-section
OTH	over the horizon
SNR	signal-to-noise ratio
SCNR	signal-to-clutter-plus-noise ratio
CNR	clutter-to-noise ratio
GSC	generalized sidelobe canceller
CAMPAC	clutter-based adaptive MIMO phased-array calibration
MVDR	minimum variance distortionless response
PCB	printed circuit board
COTS	commercial off the shelf
VCO	voltage-controlled oscillator
DSB	double sideband

Acknowledgements

There are many individuals who have provided me with immense support, assistance, and encouragement throughout my graduate career. First and foremost, I would like to thank my dissertation adviser, Dr. Jeffrey Krolik. Dr. Krolik has been an outstanding mentor, a phenomenal teacher, and a steadfast encourager. I'm extremely grateful for the opportunity he has given me to research such interesting and challenging problems. Additionally, I'm especially grateful for the unwavering support he provided me in developing a radar array testbed, a project which at the outset had an uncertain outcome.

I would like to thank Dr. Matthew Reynolds for taking significant amounts of time to mentor me in the process of developing RF hardware and lending his considerable expertise in the area. Without him, large portions of this research would not be possible.

I would like to thank Dr. Loren Nolte and Dr. Olaf Von Ramm for serving on my dissertation committee and providing valuable advice and support.

I would like to thank Joseph Thomason, Dr. Brian Freburger, Dr. Geoffrey San Antonio, and Serafin Rodriguez at the Naval Research Laboratory in Washington, D.C, in sponsoring me for a doctoral co-op in 2009 and 2010. I learned so much from each of them and the co-op experience was an essential part of my career. I would like to also thank Dr. Geoffrey San Antonio for serving on my dissertation committee and continuing to support me after I had completed my official time at

the Naval Research Laboratory.

I would like to thank the Office of Naval Research and the Naval Research Laboratory for funding my graduate career.

I would like to thank Dr. Jeffrey Krolik, Dr. Michael Papazoglou, Dr. Granger Hickman, and Michelle Shrott at STRAD Corporation in Chapel Hill, North Carolina, for supporting me in my endeavor to develop the STRADAR testbed. I would like to especially thank Dr. Granger Hickman for his patience with me as I took over sections of his office with lab equipment.

I would like to thank my former colleagues Dr. Hailiang Tao, Dr. Oguz Kazanci, Dr. Vito Mecca, Dr. Jeffrey Rogers, Dr. Ryan Goldhahn, and Dr. William Lee for welcoming me into graduate school and mentoring me as a beginning student. I would like to thank colleagues Jonathan Odom and Li Li, who were with me most of the time I was a graduate student, for their support and advice and for serving as academic sounding boards for concepts I was working through. I would like to thank more recent colleagues Itay Cnaan-on, Jonathan Soli, Juan Ramirez Jr., and Xu Chi for providing an collegial environment and for their assistance on my later experiments. I would also like to thank Christopher Potts and Jeffrey Doyle for their support.

I would like to thank Dr. Kyle Bradbury, Dr. Christopher Ratto, Philip Brown, Sara Duran, and Dr. Stewart Thomas, for their friendship and companionship as together we started a new chapter in our lives at the Department of Electrical and Computer Engineering at Duke University. The first couple years of graduate school were some of the most difficult and stressful times in my life, and without their camaraderie. I would like to especially acknowledge Dr. Kyle Bradbury, my best friend and colleague who was not only with me through six years of graduate school at Duke University, but also for the preceding four at Tufts University.

I would like to thank Father Michael Martin, Father John McDonagh, Father

Matthew Monnig, Catherine Preston, Emma Miller, Michelle Barreto, Ruth Anne Kennedy, Nicole Nash, Andrew Witchger and his family, and all of the staff and volunteers at the Duke Catholic Center, which provided me with spiritual support and moral guidance throughout my graduate career. I would like to thank Dr. Kevin Gonzales, Dr. Amanda Quiring Gonzales, Dr. Kyle Bradbury, Allison Curseen, and Justin Migacz for their indispensable support through our weekly Bible Studies.

I would like to thank my many colleagues in the "Krzyzew's Chefs" and the ECE basketball ticket group for many an enjoyable evening and weekend.

Lastly, but most importantly, I would like to express my boundless thanks for my family, specifically my father James Yu, my mother Jeanne Chapman, and my younger brother, Benjamin Yu, for their unwavering love and support throughout my entire life, in all of my endeavors.

1

Overview

In radar systems, propagation is often assumed to be line-of-sight. This assumption is often true for radars monitoring the sky, or for airborne radar surveying non-urban terrain. However, in certain environments, such as a ground-vehicle-mounted radar in an urban environment, an airborne or helicopter-mounted radar surveying an urban environment, or a radar used indoors, multipath propagation becomes a significant effect. Multipath propagation, by definition, is a propagation path resulting from scattering off of two or more scatterers. Multipath propagation can be especially inhibiting when it becomes spread in Doppler, as most radars discriminate targets (backscatter off of scatterers of interest) from clutter (backscatter off of scatterers not of interest; often times these include the ground, walls and ceilings, environmental obstructions, etc.) from their respective Doppler shifts. Line-of-sight backscatter off of stationary clutter either has zero-Doppler shift (if the radar platform is stationary), or an easily modeled and predictable relationship between Doppler shift, azimuth angle, and elevation angle (if the radar platform is moving). However, multipath propagation off of clutter is highly environment-specific and may be very difficult to model. If either the radar or the clutter has a non-zero velocity, then the resulting

multipath will become shifted or spread in Doppler, and has the potential to cause false alarms or to obscure legitimate targets.

Recent developments in multipath-input multipath-output (MIMO) radar have shown promise in both mitigating and characterizing multipath propagation. These developments will be discussed in detail in Chapter 2, which provides a thorough literature review of MIMO radar. A MIMO radar is a radar which has multiple receiver channels and multiple transmitter channels, and in which each of the transmitter channels is excited with a waveform that is orthogonal to each of the waveforms exciting the other transmitter channels. Because the transmitted waveforms are orthogonal, they can be separated after reception with signal processing techniques, such as matched filtering. One novel application of MIMO radar is often referred to as "virtual non-causal transmit beamforming". Beamforming is the process of forming a weighted sum of multiple array elements to emphasize or suppress specific spatial frequencies (which correspond to spatial angles). On the receiver side, beamforming is performed after transmission and reception, and many beamforming techniques have developed, both adaptive and non-adaptive. On the transmit side, before the advent of MIMO radar, beamforming had to be performed before transmission, that is, a predetermined set of weights were applied to each transmitter channel before transmission. MIMO radar allows for the multiple transmit channels to be separated after transmission and reception via signal processing techniques, and thus transmit beamforming weights can be applied "after-the-fact" (hence the name "non-causal transmit beamforming"). Receive beamforming discriminates in direction-of-arrival (DoA), and transmit beamforming discriminates in direction-of-departure (DoD). Any line-of-sight propagation path has a DoA that is identical to its DoD. Therefore, joint transmit-receive beamforming, made possible via MIMO radar, can discriminate between returns that propagated line-of-sight versus returns that did not. With this ability, multipath propagation returns can be identified and

suppressed.

The work of this dissertation can be divided into roughly four components. The first, defines the joint transmit-receive "bi-directional spatial spectrum" made possible by MIMO radar. The bi-directional spectrum is a function of DoA angle and DoD angle and is property of a propagation environment. A MIMO radar system can be used to estimate the bi-directional spatial spectrum for a given environment. Combined with traditional radar range and Doppler processing, a comprehensive view of the environment can be obtained. In this domain, spectral components in which the DoD angle equals the DoA angle correspond to line-of-sight propagations, and components in which the DoD angle does not equal the DoA angle correspond to multipath propagations. Thus, adaptive beamformers in this bi-directional spatial domain can be designed to suppress multipath propagations, particularly multipath clutter. One particularly useful application of the bi-directional spatial spectrum is the ability to estimate the rank of the clutter covariance matrix, which is essential to designing partially adaptive beamforming algorithms.

The second segment of this work focuses on applying multipath clutter suppression algorithms to ground-vehicle-mounted ground-moving-target-indicator (GMTI) radars. GMTI radars are radars whose purpose is to detect and track moving targets on the ground. (The 'G' in GMTI refers to the target's location, not that of the radar. In practice, most GMTI radars are mounted to aircraft). On ground vehicles in urban environments, GMTI radar is precluded by the prevalence of multipath propagation off of a variety of objects (buildings, highway guardrails, parked cars, etc.), and since the vehicle is moving, these multipath clutter returns are spread in Doppler. With the ability of MIMO radar to suppress multipath propagation returns, this problem is mitigated. One issue with MIMO radars, is that due to the high number of degrees of freedom, very large training data sets are required to implement fully adaptive algorithms. This work proposes a partially adaptive multipath suppres-

sion algorithm with realistic training requirements, based off of work proposed for non-MIMO radar systems. Simulation results are presented which demonstrate that this algorithm with a MIMO radar performs significantly better than a traditional non-MIMO radar due to the ability to suppress the multipath.

The third segment exploits a feature of the bi-directional spatial spectrum for array calibration. Array calibration typically requires artificial point sources to be placed in precisely known locations around the array, and to calibrate the array based off of these known sources. This process can be tedious, and in certain scenarios artificial point sources may not be available. Since MIMO radar allows for after-the-fact beamforming on both transmit and receive, ground clutter can be exploited as a source of opportunity for calibration. Ground clutter typically exists at all azimuth angles surrounding the array. Barring the presence of large, close by scatterers, backscatter, ground clutter propagates line-of-sight. (It is important to note that the desired application for this segment of the work is different from the that of the previous section. In the previous segment, the application was a moving vehicle in a multipath-rich environment. The application for this segment, MIMO-based array calibration, the desired application is a stationary radar in a relatively multipath-free environment.) In either the transmit or receive spatial domains, ground clutter appears at all angles, but in the joint bi-directional domain ground clutter appears along the "direct-path diagonal" of the two-dimensional surface. This sidelobes of this diagonal provide a metric to be calibrated against, and thus calibration scheme is proposed for a MIMO radar system without the need for artificial point targets is proposed.

The fourth segment of this work describes the development of a low-power, portable, S-band MIMO radar testbed with 16 receiver channels and 4 MIMO transmitter channels. This system was developed by the author in conjunction with STRAD Corporation (based in Chapel Hill, North Carolina), and professors Jeffrey

Krolik and Matthew Reynolds at Duke University. Custom radio frequency (RF) transmitter and receiver boards were designed and fabricated, and integrated with an off-the-self National Instruments Data Acquisition (boards). A custom, portable, and attractive enclosure was designed to house all of these components. The device, named the STRADAR, can be controlled via any personal computer (PC) running the MATLAB software package, making it an accessible tool for research. Details of the system, its capabilities, and some sample uses are documented.

The overarching theme of this work is the use of MIMO radar to differentiate between line-of-sight propagations and multipath propagations. The novel contributions of this work are:

1. Development of a statistical definition of the bi-directional spatial spectrum and how it relates to MIMO radar, including the ability to estimate the rank of the clutter covariance matrix

2. Development of a partially adaptive multipath suppression algorithm using MIMO radar and realistic training requirements

3. Development of a calibration scheme based off of ground clutter via MIMO radar

4. Development of a low-power, portable, MATLAB-compatible, S-band MIMO radar testbed with 16 receiver channels and 4 transmitter channels

The remainder of this dissertation is organized as follows: Chapter 2 is an in-depth review of the concept of MIMO radar in the technical literature. Chapter 3 is a discussion of the MIMO bi-directional spatial spectrum. Chapter 4 is a discussion of the problem of multipath clutter for ground-vehicle-mounted GMTI radars, and proposes a partially adaptive algorithm to suppress multipath clutter. Chapter 5 proposes a calibration scheme using MIMO radar and ground clutter. Chapter 6

describes the STRADAR testbed system and real results collected from the system. Chapter 7 describes a set of experiments performed with the STRADAR. Chapter 8 is the conclusion.

2

Multiple-input multiple-output (MIMO) radar

The concept of a multiple-input multiple-output (MIMO) radar system was first proposed in 2004 in [1]. Since then, substantial research has been conducted on the concept. This chapter will present an overview of radar signal processing principles, an overview of the concept of MIMO radar, and a review of the technical literature relating to MIMO radar.

2.1 Linear Frequency Modulated Continuous Wave Radar

One common radar waveform is the linear frequency-modulated waveform, sometimes referred to a chirp. A LFM waveform is a sinusoid with a frequency that changes linearly with time. This waveform has the form:

$$x_p(t) = e^{j2\pi(f_c - \frac{B}{2})t + j\pi\frac{B}{T_0}t^2} \qquad 0 \leqslant t < T_0 \tag{2.1}$$

where f_c is the RF center frequency (Hz), B is the RF swept bandwidth (units of Hz), T_0 is the time duration of one chirp (units of s), and t is the time variable (units of s). Radars typically repeat waveforms periodically. A train of M LFM waveforms

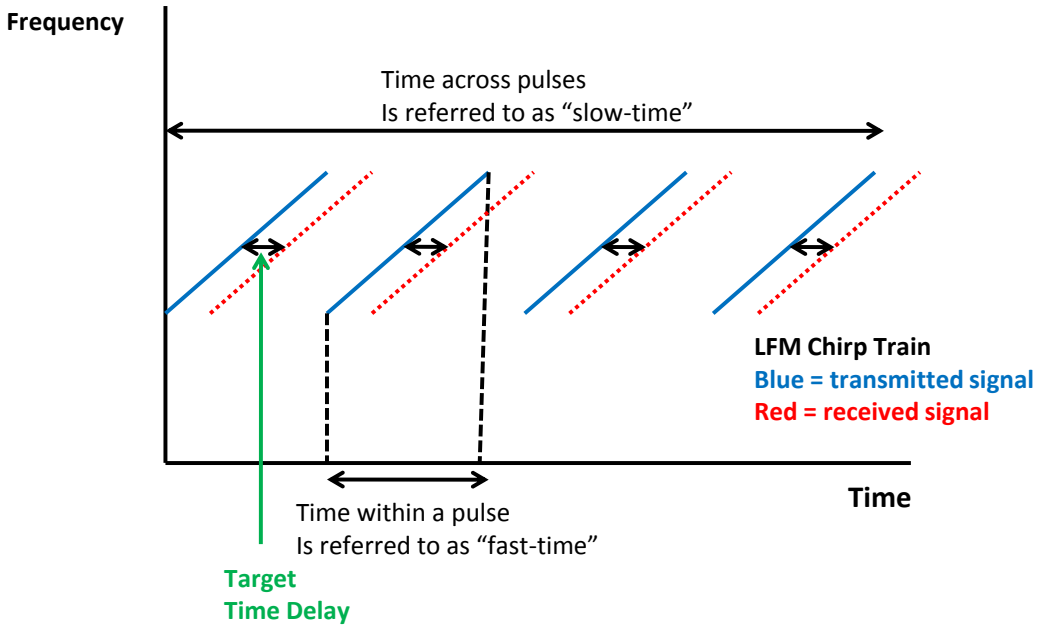

FIGURE 2.1: LFM Waveform in the Time-Frequency Domain

has the form:

$$x(t) = \sum_{m=0}^{M-1} x_p(t - mT_p) \tag{2.2}$$

where T_p is referred to as the waveform repetition interval (WRI, units of s). The ratio of $\frac{T_0}{T_p}$ is referred to as the duty cycle and often expressed as a percentage. In continuous wave (CW) systems the duty cycle is 100%, and thus $T_0 = T_P$. The quantity $\frac{1}{WRI}$ is referred to as the waveform repetition frequency (WRF, units of Hz). The quantity MT_p is referred to as the coherent processing interval (CPI, units of s) or the coherent integration time (CTI, units of s). In common radar terminology, time within a single pulse is referred to as “fast-time” and time across pulses is referred to as “slow-time”. An illustration of the waveform $x(t)$ (2.2) in time-frequency space and the notion of “fast-time” and “slow-time” is shown in Figure 2.1.

The received return can be modeled as the sum of many point scatterers. The return from each point scatterer is the transmitted waveform delayed and Doppler-

shifted. The time delay is proportional to the slant range of the point scatterer. If the waveform is sufficiently narrowband ($B \ll f_c$), and the maximum scatterer velocity is much less than the speed of light, the Doppler shift can be modeled as a frequency modulation that is proportional to the scatterer's tangential velocity. The radar received signal is:

$$y(t) = \sum_i \alpha_i x(t - \tau_i) e^{j2\pi F_{Di} t} \tag{2.3}$$

where α_i is a complex amplitude coefficient that is proportional to the radar cross-section (RCS) of the i^{th} point scatterer, τ_i is the time delay of the return from the i^{th} point scatterer, and F_{Di} is the Doppler shift associated with i^{th} point scatterer. The range of the i^{th} scatterer is proportional to its time delay: $r_i = \frac{c\tau_i}{2}$, where c is the speed of light. The standard radar detector is the matched filter, which is the optimal detector for a signal in the presence of uncorrelated random noise. For a single point scatterer, the matched filter output will have a peak at the time delay associated with the scatterer. To account for Doppler shift, a matched filter can be designed for each hypothesized Doppler shift. A surface can be formed from the matched filter outputs:

$$z(t, F_D) = \int_{-\infty}^{\infty} y(s) x^*(s - t) e^{-j2\pi F_{Di} s} ds \tag{2.4}$$

The amplitude of this surface is referred to as an amplitude-range-Doppler (ARD) surface. In systems without full digital signal processing available across the entire bandwidth, sub-optimal techniques that can be implemented in analog circuitry can be employed instead. These techniques will be discussed later in Chapter 6, which covers the experimental apparatus fabricated for this work.

An important metric for radar waveforms is the ambiguity function. The ambi-

guity function is defined as the magnitude of the output of matched filter designed for a waveform $x(t)$, when the input is the function $x(t)$ with a Doppler shift:

$$A(t, F_D) = \left| \int_{-\infty}^{\infty} x(s) e^{j2\pi F_D s} x^*(s-t) ds \right| \tag{2.5}$$

Note that ambiguity function of (2.5) is very similar to the matched filter output of (2.4). From the ambiguity function, important radar parameters such as range resolution, Doppler resolution, and the presence and location of any ambiguities in range and/or Doppler can be derived. It is well-known [2] that the ambiguity function of the single LFM pulse of (2.1), demodulated to baseband, is:

$$A_{LFM}(t, F_D) = \left| \frac{\sin(\pi(F_D + Bt/T_0)(T_0 - |t|))}{T_0 \pi (F_D + Bt/T_0)} \right| \qquad -T_0 \leqslant t \leqslant T_0 \tag{2.6}$$

The ambiguity function of the waveform train of (2.2) is:

$$A_{train} = \sum_{m=-(M-1)}^{M-1} A_{LFM}(t - mT_p, F_D) e^{j\pi F_D (M-1+m) T_p} \frac{\sin(\pi F_D (M - |m|) T_p}{\sin(\pi F_D T_p)} \tag{2.7}$$

From the ambiguity function, it can be determined that for the LFM chirp train waveform of (2.2), the range resolution $\Delta r = \frac{c}{2B}$, the Doppler resolution $\Delta F_D = \frac{1}{MT_p} = \frac{1}{CPI}$, the maximum unambiguous range $R_{max} = \frac{cT_p}{2}$, and the maximum unambiguous Doppler $F_{D,max} = \frac{1}{2T_p} = \frac{WRF}{2}$.

The preceding section consists of commonly known radar signal processing techniques. More details can be found in [2–4].

2.2 Multiple-input Multiple-Output (MIMO) Radar

Radar systems often employ electronically-steered antenna arrays to be able to discriminate in spatial frequency, which corresponds to spatial angle. A special case

of an array is a multiple-input multiple-output (MIMO) system. A MIMO has system has both multiple receiver elements and multiple transmitter elements, and each transmitter element is fed with a waveform that is orthogonal to all of the waveforms fed to the other transmitter elements. Mathematically, two waveforms $s_1(t)$ and $s_2(t)$ are orthogonal if:

$$\int_{-\infty}^{\infty} s_1(t)s_2^*(t) = 0 \tag{2.8}$$

It is important to note that in radar, the received waveforms return time-delayed and Doppler-shifted, and no two waveforms are orthogonal for all possible time delays and all possible Doppler shifts. However, there does exist sets of waveforms which achieve orthogonality for some limited set of time delays and Doppler shifts. The orthogonality condition allows the various transmitter channels to be separated after reception. If identical waveforms were fed to each of the transmitter elements, there would be no method of separating the signals from the different transmitter elements.

Two intuitively simple ways of achieving waveform orthogonality are to stagger the waveforms in time or in frequency. With time-staggering, each waveform is time-delayed by a unique amount of time. With frequency staggering, each waveform is modulated by an unique frequency shift. Since radar returns are time-delayed and Doppler-shifted, the time-staggered waveforms are orthogonal for all scatterer delays less than the minimum difference in pre-applied time delays, and the frequency-staggered waveforms are orthogonal for all scatterer Doppler shifts less than the minimum difference in pre-applied frequency modulations. In [5], a set of MIMO waveforms were proposed that did not change the waveform structure within a pulse. Instead, a linear phase modulation was applied across pulses ("slow-time"), and the slope of the phase modulation was different for each channel. Due to the vast difference of scale between "fast-time" and "slow-time" ($\tau \ll T_p$) this has the effect

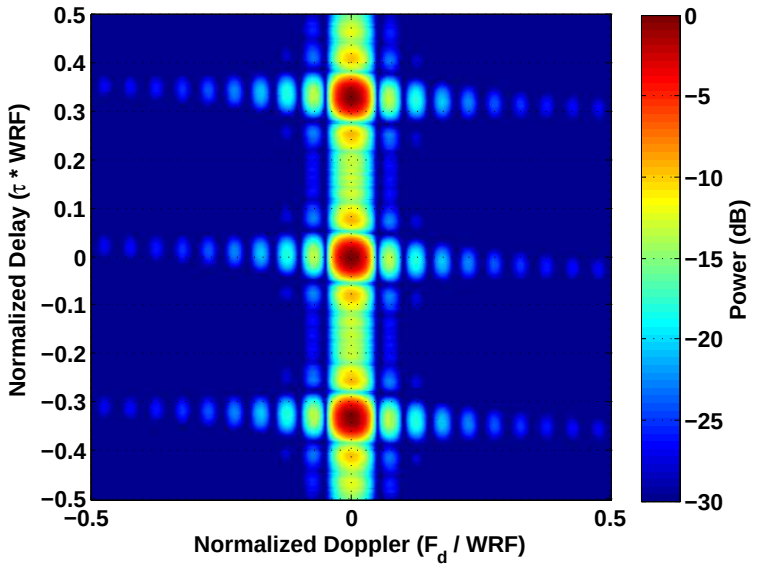

FIGURE 2.2: MIMO Time-Staggered Ambiguity Function

of imposing a different Doppler-shift onto each channel, while not changing the RF bandwidth and center frequency. These waveforms were called the "SLO-MO" waveforms (short for "slow-time MIMO"). The major advantage of both time-staggered and SLO-MO waveforms is that the radar receiver hardware does not need to be modified to handle these waveforms. Fig. 2.2 shows the normalized ambiguity function of the time-staggered MIMO waveforms, and Fig. 2.3 shows the normalized ambiguity of the SLO-MO waveforms. Observe that the time-staggered waveforms are separated in time delay and that the SLO-MO waveforms are separated in Doppler shift.

2.3 Review of MIMO Radar in the Technical Literature

Many different applications of MIMO radar have been proposed in the technical literature. Broadly speaking, the existing literature in MIMO radar can be divided into four categories:

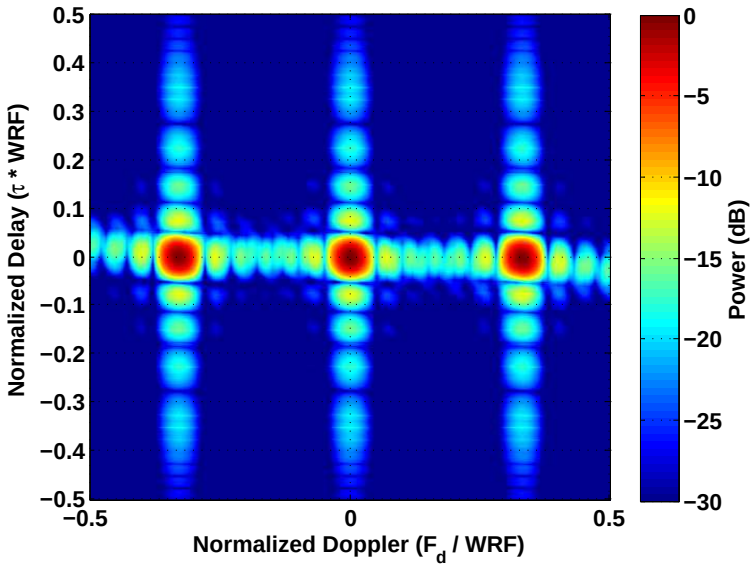

FIGURE 2.3: MIMO SLO-MO Ambiguity Function

- **MIMO waveform design and analysis** proposes and analyzes the performance of various MIMO waveforms

- **MIMO radar with widely separated antennas for spatial diversity** studies the scenario in which the individual transmit and receive elements are separated by large distances. In this situation, MIMO radar can be used to exploit spatial diversity for improved target detection.

- **MIMO radar with co-located antennas for aperture synthesis** uses MIMO radar with co-located transmit and receive arrays to virtually extend the array aperture. This application of MIMO radar can result in improved spatial resolution and/or lower spatial sidelobes using sparsely populated arrays, compared to the performance of traditional arrays.

- **MIMO radar with co-located antennas for non-causal transmit beamforming** uses MIMO radar with co-located transmit and receive arrays to perform non-causal ("after-the-fact") adaptive beamforming on the transmit side

Each of these categories will be briefly summarized. The application of MIMO radar most relevant to this work, MIMO radar with co-located antennas for non-causal transmit beamforming, with be discussed last in more detail.

2.3.1 MIMO waveform design and analysis

Yang and Blum provide a technique for generating MIMO waveforms for multistatic radar systems by maximizing the mutual information between the waveform and the target's impulse response, which they show is equivalent to minimizing the mean square error of the estimated target impulse response [6]. Since target impulse responses vary, they extended their method to a robust "mini-max" criterion which minimizes the maximum mean squared error over a set of targets [7]. Yang, Blum, He, and Fuhrmann update their previous work to include structural constraints on the MIMO waveforms and propose an alternative projection algorithm to solve for the waveforms [8]. Friedlander introduced a technique to generate optimal MIMO waveforms based upon target and clutter statistics [9]. San Antonio and Fuhrmann extended Woodward's radar ambiguity function to MIMO radar [10], and have analyzed the effect of waveform correlation on the MIMO transmit beamforming [11]. Abramovich has determined bounds on the volume and height of the MIMO ambiguity function [12, 13]. Deng used simulated annealing to generate polyphase codes that have low sidelobes [14]. Mecca, Krolik, and Robey developed the previously mentioned slow-time MIMO ("SLO-MO") waveforms [5, 15–18]. Frazer, Abramovich, and Johnson [19–21] have noted that certain MIMO waveforms may cause VSWR (voltage standing wave ratio: a measurement of how much power is reflected back from the transmitter antennas to the amplifiers) issues, and therefore MIMO waveform design must take this into account. Li, Xu, Stoica, Forsythe, and Bliss [22] analyzed the effect of range compression on the optimal MIMO waveforms. Chen and Vaidyanathan [23] derive additional properties of the MIMO ambiguity function

and a method to design MIMO waveforms to optimize the MIMO ambiguity function. They also propose a method [24] to generate MIMO waveforms that optimize the signal-to-interference-plus-noise-ratio (SINR) of an extended target in clutter given prior knowledge of the target and clutter statistics. Forsythe and Bliss analyze the performance of various MIMO waveforms for MIMO GMTI in the presence of clutter, and how the waveform selection is limited by that performance [25]. Tang, Tang, and Peng propose a method for generating MIMO waveforms in the presence of colored noise [26, 27]. Rabideau proposes a metric to quantify the clutter cancellation performance of MIMO waveforms [28]. Babur, Krasnov, Yarovoy, and Aubry analyze the orthogonality of time-staggered LFM waveforms [29].

2.3.2 MIMO radar with widely separated antennas for spatial diversity

Fishler, Haimovich, et al. have proposed what they term "Statistical MIMO Radar" [1, 30–33] to improve radar target detection for multistatic radar systems. Multistatic radar systems are defined as radar systems with transmitter and receiver elements widely separated from each other. Target detection performance is reduced by fluctuations of the target's RCS (radar cross section) [2–4]. Target RCS fluctuations are often characterized by a probabilistic Swerling model. The proponents of multistatic MIMO radar make an analogy between target RCS fluctuations in radar and channel fading in communications, and propose a solution based on the MIMO communications concept. They propose using a set of widely spaced transmit elements and receive elements, and transmitting orthogonal waveforms on each of the the transmit elements. They claim that each transmitter-receiver pair constitutes an independent radar. The data from the "independent radars" are then treated as independent observations to improve the performance of a traditional Bayesian detector. Since the data from each transmitter-receiver pair is processed non-coherently, there is no SNR gain from traditional, coherent array processing techniques.

MIMO radar for spatial diversity has come under criticism by some in the radar community. In [34], Chernyak states that many of the concepts proposed were already commonly known in the multistatic radar community and multistatic MIMO is simply a particular case of the more general multistatic radar concept. He also points out that the energy gain achieved by fluctuation smoothing saturates after the number of transmitter-receiver combinations is about five , which can easily be achieved with a single transmitter and a few receivers, and thus there is no need for MIMO. Additionally, he questions the reasoning behind the uncorrelated assumption and the narrowband assumption that Fishler, et al. employ. Overall, Chernyak states that the work proposed in [1, 30–33] has numerous flaws because it simply translates the MIMO communications concept to radar without taking into account the differences in the radar scenario, and presents "new" conclusions which have been known in the radar field for many years.

2.3.3 MIMO radar with co-located antennas for aperture synthesis

An application of MIMO radar with co-located antennas is the improvement of spatial resolution and sidelobes for direct-path propagation. Forsythe and Bliss [35, 36] and Robey [37] have explored this aspect of MIMO radar. The MIMO virtual aperture can be calculcated by performing the convolution of the real antennas positions of both the transmitter and the receiver. For example, assume a MIMO radar system has a 3-element receive array with Nyquist spacing of $\lambda/2$. Represent this array as $\{1\ 1\ 1\}$, where each entry represents the number of antennas at a location on a $\lambda/2$ grid. If the transmit array also has 3 elements spaced at $\lambda/2$, then the MIMO virtual aperture is $\{1\ 2\ 3\ 2\ 1\}$. In this example, some locations are overrepresented and the full advantage of MIMO is not realized. Following from the above logic, it should be possible to use sparse arrays to obtain a wide MIMO aperture. For example, assume a MIMO system with a 4-element receive array spaced at $\lambda/1$, represented by $\{1\ 1$

1 1}. The transmit array is sparse and spaced by the length of the receive array, given by {1 0 0 0 1 0 0 0 1 0 0 1}. Then the MIMO virtual aperture is {1 1 1 1 1 1 1 1 1 1 1 1 1 1 1 1}, which is a 16 element array with the elements spaced at $\lambda/2$. However, only 8 physical antennas (4 transmit, 4 receive) are needed to achieve this aperture. Bliss et. al [38–41] applied this concept to MIMO ground-moving target-indicator (GMTI) with space-time adaptive processing (STAP) radar to improve spatial resolution. Chen and Vaidyanathan [42], Chong et. al. [43], and Wang and Lu [44] also explore MIMO with space-time adaptive processing. Critically, all of the preceding papers assume direct-path propagation only and no significant multipath. Sun et. al [45, 46] and Ahman et. al. [47] use co-located MIMO radar to obtain better spatial resolution on the synthetic aperture radar (SAR) application. The concept of combined transmit/receive beamforming has been explored before in the concept of coarrays and subarrays ([48],[49]). The advantage of MIMO is that it allows for the weights to be applied in digital processing after reception.

Additionally, Li and Stoica [50] have shown the MIMO radar allows for improved parameter identifiability (more parameters can be identified due to more data points collected), the direction application of adaptive non-parametric parameter estimation algorithms (due to improved covariance matrix estimation due to more data points), and the flexibility of transmit beampatterns.

2.3.4 MIMO radar with co-located antennas for non-causal transmit beamforming

The application MIMO radar that is examined in this work is sometimes referred to as "non-causal" transmit beamforming. Traditionally, when performing transmit beamforming, the transmit weights must be applied to the waveforms before transmission. With MIMO radar, virtual transmit beamforming can be performed after reception on the received data. Because the MIMO waveforms are orthogonal, the transmit channels can be separated at the receiver. Transmit beamforming weights

can be applied to the transmit channels after reception. As MIMO waveforms are orthogonal, the instantaneous transmit beampattern is constantly changing, and thus energy propagates in all directions, making after-the-fact transmit beamforming possible. However, there is a loss of energy compared to the case where the transmit beamforming was performed before-the-fact, as the energy is not focused in one direction. MIMO non-causal transmit beamforming has the key ability to design a different transmit beamformer as a function of range, something that is not possible with traditional transmit beamforming. Additionally, joint non-separable transmit-receive beamformers can be designed, also as a function of range.

Frazer, Abramovich, and Johnson [12, 13, 19–21, 51–54] have used this technique in OTH (over-the-horizon) radar. In OTH radar, the platform is stationary but moving layers of the ionosphere introduce Doppler-spread on backscatter from the ground which travels back to the receiver via multiple paths, which may include the arrival angle of target of interest. In this case, non-causal transmit beamforming provides a means of suppressing receive-mainlobe Doppler-spread clutter by placing a virtual transmit null in one or more direction-of-departure (DoD) which is adapted as a function of slant range. An important feature of the OTH radar problem which can significantly simplify implementation and training of the MIMO radar beamformer weights is the nominally discrete nature of multipath propagation via different layers of the ionosphere at any given slant range. A method for snapshot-starved training in MIMO radar which imposes a Kronecker structure on the bi-directional transmit-receive beamformer is proposed in [54]. Imposing a Kronecker structure on the beamformer reduces the degrees of freedom from $N_r \times N_t$ to $N_r + N_t$, however, it forces the beamformer to be separable in transmit and receive. Such an approach is appropriate for applications where there are limited and discrete modes of propagation, such as OTH radar, and therefore the multipath is approximately separable at a single range bin. However it is not appropriate for applications where the mul-

tipath propagation forms a continuum of DoA and DoD angles. Additionally, the Kronecker MIMO beamformer may overly restrict the number of degrees of adaptive freedom below the rank of the clutter covariance matrix in scenarios with significant multipath propagation.

Mecca, Krolik, and Robey [5, 15–18, 55] and Hickman and Krolik [56] have proposed using slow-time MIMO waveform for MIMO non-causal transmit beamforming and have extended this to MIMO space-time adaptive processing (STAP). STAP [57] jointly processes slow-time samples and receiver channels, which is advantageous when clutter and interferers are not separable in angle-Doppler space. MIMO STAP joint process slow-time samples, receiver elements, and transmit elements. MIMO non-causal transmit beamforming has also been proposed as a means of suppressing multipath-induced artifacts in synthetic aperture radar imaging [58]. With complete knowledge of the clutter and noise covariance matrices, fully adaptive MIMO STAP, which is adaptive over transmit, receive, and Doppler, is the theoretically optimal solution for improving signal-to-clutter-plus-noise ratio (SCNR). However it requires an excessive amount of training data due to the large number of degrees of freedom ($M \times N_r \times N_t$, where M is the number of slow-time pulses, N_r is the number of receivers, and N_t is the number of transmitters). Fully adaptive MIMO STAP also requires training over adjacent range bins, which are assumed to have the same clutter statistics as the range bin under test. In many multipath scenarios, however, it is inappropriate to train over range bins because the multipath clutter varies with range.

The dissertation utilizes the concept of non-causal transmit beamforming to mitigate spread-Doppler multipath clutter in the scenario in which (a) multipath propagation forms a continuum of DoA and DoD angles, (b) the multipath clutter varies with range, and (c) limited training snapshots are available. The proposed scenario is of a ground-vehicle driving in an urban environment implementing GMTI radar.

The next two chapters will explain this scenario in detail.

2.4 Summary

This chapter has explained the basics of LFM radar and MIMO radar. Additionally, a review of MIMO radar in the technical literature was presented. The next chapter focuses on the MIMO signal model and the development of a MIMO bi-directional spectrum to characterize multipath.

3

Signal Model and the MIMO Bi-directional Spectrum

This chapter will describe the MIMO signal model that is the framework for the remainder of this work. It will also introduce the concept of the MIMO bi-directional spatial spectrum, an analytical tool to characterize multipath propagation.

3.1 Slow-Time MIMO Model

Assume a radar system with N_t transmit elements and N_r receive elements. Each transmit element is excited by a pulse train consisting of M pulses, each of which have a duration of T_m. It is assumed here that the signal is sufficiently narrowband, i.e. $\frac{\beta}{f_c} \ll 1$, where β is the RF bandwidth and f_c is the RF carrier frequency. Without loss of generality, assume MIMO is implemented using the SLO-MO waveforms (previously mentioned in Chapter 2). The transmitted signal from the l^{th} transmit element is shown in (3.1).

$$u_l(t) = \sum_{m=0}^{M-1} u_p(t - mT_p) \exp(j2\pi \frac{l}{N_t T_p} t) \tag{3.1}$$

where $u_p(t)$ is the transmitted waveform. To model the return, consider a single signal component leaving the transmitter with the spatial frequency of $\mathbf{k}_t$, which is scattered back to the receiver with spatial frequency of $\mathbf{k}_r$ and a Doppler shift of f_d. After the component is pulse-compressed, range-gated, and the MIMO channels are separated (by demodulating and filtering in slow-time), the m^{th} pulse from the n^{th} receive element and the l^{th} transmit element is:

$$v_{lmn} = e^{j\mathbf{k}_r^T \mathbf{x}_{rn}} e^{-j\mathbf{k}_t^T \mathbf{x}_{tl}} e^{j2\pi f_d m} \tag{3.2}$$

where $\mathbf{x}_{rn}$ is the position of the n^{th} receive element and $\mathbf{x}_{tl}$ is the position of the l^{th} transmit element. A negative sign compensates for the difference between incoming (receive) and outgoing (transmit) angles. For a single pulse, the signal in (3.2) can be represented by a vector, which is the Kronecker product of the transmit and receive wavefront vectors. The complete vector is:

$$\mathbf{v}(\mathbf{k}_r, \mathbf{k}_t) = \mathbf{v}_t(\mathbf{k}_t) \otimes \mathbf{v}_r(\mathbf{k}_r) \tag{3.3}$$

$$\begin{aligned} \mathbf{v}_r(\mathbf{k}_r) &= \left[e^{j\mathbf{k}_r^T \mathbf{x}_{r1}}, ..., e^{j\mathbf{k}_r^T \mathbf{x}_{rN_r}} \right]^T \\ \mathbf{v}_t(\mathbf{k}_t) &= \left[e^{-j\mathbf{k}_t^T \mathbf{x}_{t1}}, ..., e^{-j\mathbf{k}_t^T \mathbf{x}_{tN_t}} \right]^T \end{aligned} \tag{3.4}$$

The combination of outgoing and incoming plane-waves defines a "bi-directional wavefront". In general, the radar return can be represented as a sum of individual bi-directional wavefront vectors. The components of the return can be characterized as targets, clutter, and noise (jamming is not considered in this work). Furthermore, the clutter returns can be divided into types: direct-path clutter and multipath clutter. For direct-path clutter, the direction-of-arrival spatial frequency $\mathbf{k}_r$ equals the direction-of-departure spatial frequency $\mathbf{k}_t$, whereas for multipath clutter the two directions are different. The complete radar return can then be described by the data

vector $\mathbf{z}$ given by:

$$\mathbf{z} = \mathbf{z}_s + \mathbf{z}_{cd} + \mathbf{z}_{cm} + \mathbf{z}_n \tag{3.5}$$

where $\mathbf{z}_s$ represents the target return, $\mathbf{z}_{cd}$ represents the direct-path clutter return, $\mathbf{z}_{cm}$ represents the multipath clutter return, and $\mathbf{z}_n$ represents uncorrelated noise. Assume each component is the sum of one or more bi-directional wavefront vectors with zero-mean complex Gaussian amplitudes. The complete (target-plus-clutter-plus-noise) covariance matrix is shown by:

$$\mathbf{R}_z = \mathbf{R}_s + \mathbf{R}_{cd} + \mathbf{R}_{cm} + \mathbf{R}_n \tag{3.6}$$

where the target-free (clutter-plus-noise) covariance matrix, $\mathbf{R}_I$, is the sum of the direct-path clutter, multipath clutter, and uncorrelated noise covariance matrices:

$$\mathbf{R}_I = \mathbf{R}_{cd} + \mathbf{R}_{cm} + \mathbf{R}_n \tag{3.7}$$

The target signal's covariance matrix for a target with spatial frequencies $\mathbf{k}_s$ and radar cross-section (RCS) σ_s^2 is modeled as a rank-one outer product.

$$\mathbf{R}_s = \sigma_s^2 \mathbf{v}(\mathbf{k}_s, \mathbf{k}_s)\mathbf{v}^H(\mathbf{k}_s, \mathbf{k}_s) \tag{3.8}$$

The target is assumed to arrive by direct-path only; therefore $\mathbf{k}_R = \mathbf{k}_T$. Similarly, the direct-path clutter covariance matrix can be expressed as:

$$\mathbf{R}_{cd} = \int_{\mathbf{k} \in \mathbf{K}_{cd}} \sigma_{cd}^2(\mathbf{k})\mathbf{v}(\mathbf{k}, \mathbf{k})\mathbf{v}^H(\mathbf{k}, \mathbf{k}) d\mathbf{k} \tag{3.9}$$

where σ_{cd}^2 represents the RCS of the clutter patch at spatial frequency $\mathbf{k}$ and $\mathbf{K}_{cd}$ is the set containing all spatial frequencies for which direct-path clutter exists. Because this term represents the direct path clutter, the transmit and receive spatial frequencies are equal. The multipath clutter covariance matrix is:

$$\mathbf{R}_{cm} = \int_{\mathbf{k}_r . \mathbf{k}_t \in \mathbf{K}_{cm}} \sigma_{cm}^2(s)\mathbf{v}(\mathbf{k}_r, \mathbf{k}_t)\mathbf{v}^H(\mathbf{k}_r, \mathbf{k}_t) d\mathbf{k}_r d\mathbf{k}_t \tag{3.10}$$

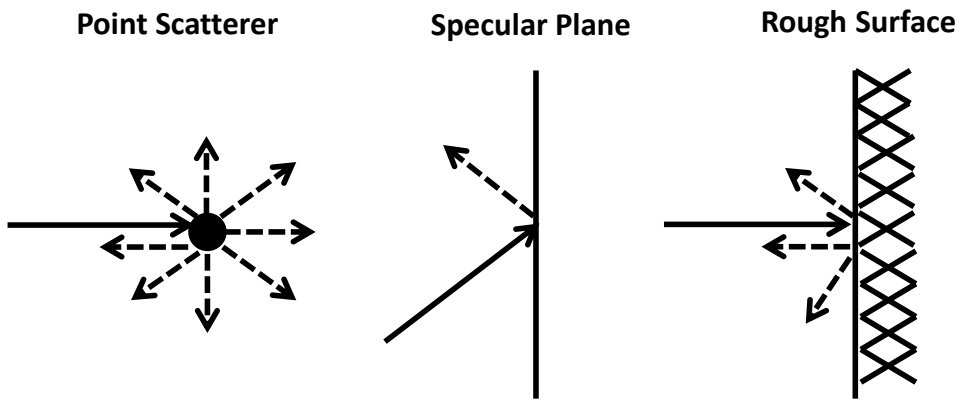

FIGURE 3.1: Three Types of Scatterers

where σ_{cm}^2 represents the RCS of the multipath clutter patch at receive spatial frequency $\mathbf{k}_r$ and transmit spatial frequency $\mathbf{k}_t$. $\mathbf{K}_{cm}$ is the set containing all transmit-receive spatial frequency combinations that exist. Using the principles of physical optics, multipath occurs when a transmit wavefront comes in contact with more than one scatterer before returning to the receiver. Scatterers can be generalized into three categories: point scatterers, specular planes, and rough surfaces. Fig. 3.1 illustrate these types. Point scatterers scatter the incoming wavefront in all directions spherically. Specular planes reflect a planar wavefront to a new direction defined by Snell's law. Rough surfaces scatter the incoming wavefront in all directions in front of the surface (half-spherically). In most radar applications, ground clutter is considered to be a rough surface. The noise is considered to be uncorrelated between all transmit and receive elements. The noise covariance matrix is:

$$\mathbf{R}_n = \sigma_n^2 \mathbf{I} \tag{3.11}$$

3.2 Bi-directional Spatial Spectrum

In [59], the concept of MIMO space-time adaptive processing for multipath clutter mitigation is addressed. MIMO STAP is adaptive in three dimensions: Doppler,

receive, and transmit. It is mentioned that by taking a slice of the Doppler-receive-transmit cube at a single Doppler cell, one could form a "transmit-receive directionality spectrum (TRDS)", and an estimate of this TRDS could be formed using standard spectral estimation techniques. The discussion in [59] assumes range-Doppler processing has already occurred and one range-Doppler cell is under investigation and assumes the covariance matrix is known.

This section generalizes that concept further, by defining a bi-directional spatial spectrum, (where the two directions are direction-of-arrival (DoA) and direction-of-departure (DoD)) for a given environment and generating techniques to estimate this spectrum, especially when a limited number of snapshot observations are available. This spectrum can be then be used not only for mitigating multipath clutter, but for mapping the multipath channel properties of a given environment, which could then be exploited. In [60] and [61], traditional beamforming and array processing are viewed as special cases of a spatial filter. MIMO beamforming, which jointly operates on transmit and receive, can be interpreted as a bi-directional spatial filter, and both adaptive (as this paper addresses) and non-adaptive bi-directional filters can be formulated and the bi-directional filter response analyzed.

The bi-directional wavefront was defined in (3.3). The concept of a bi-directional wavefront assumes a closed system, that is, all energy in the system originates from the transmitters (with the exception of uncorrelated sensor noise). In general, a bi-directional field, $s(\mathbf{x}_r, \mathbf{x}_t)$, is defined as a weighted integral of bi-directional wavefronts:

$$s(\mathbf{x}_r, \mathbf{x}_t) = \int F_s(\mathbf{k}_r, \mathbf{k}_t) \exp\left[j\left(\mathbf{k}_r^T \mathbf{x}_r - \mathbf{k}_t^T \mathbf{x}_t\right)\right] d\mathbf{k}_r d\mathbf{k}_t \tag{3.12}$$

where $\mathbf{x}_r$ represents receiver space, $\mathbf{x}_t$ represents transmit space, and $F_s(\mathbf{k}_r, \mathbf{k}_t)$ is the bi-directional Fourier transform. Imposing the wide-sense stationary condition on the bi-directional field, bi-directional wavefronts with different transmit-receive

combinations are uncorrelated:

$$E\left[F_s\left(\mathbf{k}_{r1},\mathbf{k}_{t1}\right)F_s^*\left(\mathbf{k}_{r2},\mathbf{k}_{t2}\right)\right]= \tag{3.13}$$

$$\begin{cases} E\left[\left|F_s\left(\mathbf{k}_{r1},\mathbf{k}_{t1}\right)\right|^2\right] & \text{if } \mathbf{k}_{r1}=\mathbf{k}_{r2} \text{ and } \mathbf{k}_{t1}=\mathbf{k}_{t2} \\ 0 & \text{otherwise} \end{cases}$$

where $E\left[\ \ \right]$ is the expected value. Then, the bi-directional power spectral density is:

$$S\left(\mathbf{k}_r,\mathbf{k}_t\right)=E\left[\left|F\left(\mathbf{k}_r,\mathbf{k}_t\right)\right|^2\right] \tag{3.14}$$

The bi-directional power spectral density can also be defined in terms of the bi-directional autocorrelation function. Assuming the field is wide-sense stationary, the bi-directional auto-correlation function is:

$$r\left(\mathbf{m}_r,\mathbf{m}_t\right)=E\left[s\left(\mathbf{x}_r+\mathbf{m}_r,\mathbf{x}_t+\mathbf{m}_t\right)s^*\left(\mathbf{x}_r,\mathbf{x}_t\right)\right] \tag{3.15}$$

and the bi-directional power spectral density can be expressed as:

$$S\left(\mathbf{k}_r,\mathbf{k}_t\right)=\int r\left(\mathbf{m}_r,\mathbf{m}_t\right)\exp\left[j\left(\mathbf{k}_r^T\mathbf{x}_r-\mathbf{k}_t^T\mathbf{x}_t\right)\right]d\mathbf{k}_r d\mathbf{k}_t \tag{3.16}$$

The bi-directional field exists for all potential receiver and transmitter locations, therefore, it is only a function of the environment and not a function of element locations. However, in practice, the field can only be measured at discrete receiver and transmitter element locations. Consider a system with N_r receiver elements located at $\mathbf{x}_{r1},\ldots,\mathbf{x}_{rN_r}$ and N_t transmitter elements located at $\mathbf{x}_{t1},\ldots,\mathbf{x}_{tN_t}$. Define the N_r-by-N_t data matrix $\mathbf{Z}$ as:

$$\mathbf{Z}=\begin{bmatrix} s\left(\mathbf{x}_{r1},\mathbf{x}_{t1}\right) & \cdots & s\left(\mathbf{x}_{r1},\mathbf{x}_{tN_t}\right) \\ \vdots & \ddots & \vdots \\ s\left(\mathbf{x}_{rN_r},\mathbf{x}_{t1}\right) & \cdots & s\left(\mathbf{x}_{rN_r},\mathbf{x}_{tN_t}\right) \end{bmatrix} \tag{3.17}$$

and the N_rN_t data vector $\mathbf{z}$

$$\mathbf{z}=\mathrm{vec}\left(\mathbf{Z}\right) \tag{3.18}$$

Without loss of generality, assume both the transmit and receive arrays are uniform linear arrays operating in one-dimensional space, with inter-element spacings of Δ_t and Δ_r respectively. The bi-directional covariance matrix $\mathbf{R}_z = E\left[\mathbf{z}\mathbf{z}^H\right]$ is a block Toeplitz matrix:

$$\mathbf{R}_z = \begin{bmatrix} \mathbf{R}_{r,t=0} & \cdots & \mathbf{R}_{r,t=N_t-1} \\ \vdots & \ddots & \vdots \\ \mathbf{R}_{r,t=-(N_t-1)} & \cdots & \mathbf{R}_{r,t=0} \end{bmatrix} \tag{3.19}$$

and each sub-matrix $\mathbf{R}_{r,t=k}$ is a Toeplitz matrix:

$$\mathbf{R}_{r,t=k} = \begin{bmatrix} r_k(0) & \cdots & r_k\left((N_r-1)\Delta_r\right) \\ \vdots & \ddots & \vdots \\ r_k\left(-(N_r-1)\Delta_r\right) & \cdots & r_k\left(0\right) \end{bmatrix} \tag{3.20}$$

where $r_k\left(m_r\right) = r\left(m_r, k\Delta_t\right)$ are values of the bi-directional auto-correlation function of (3.15).

The bi-directional covariance matrix $\mathbf{R}_z$ is Toeplitz-block Toeplitz, that is, it is a block Toeplitz matrix composed of Toeplitz submatrices. An estimate of the bi-directional spectrum can be formed with the bi-directional wavefront vector that was defined in (3.3) and the bi-directional covariance matrix from (3.19):

$$\hat{S}\left(\mathbf{k}_r, \mathbf{k}_t\right) = \mathbf{v}^H\left(\mathbf{k}_r, \mathbf{k}_t\right) \mathbf{R}_z \mathbf{v}\left(\mathbf{k}_r, \mathbf{k}_t\right) \tag{3.21}$$

or from the bi-directional wavefront vector and the the bi-directional data vector from (3.18):

$$\hat{S}\left(\mathbf{k}_r, \mathbf{k}_t\right) = \left|\mathbf{v}^H\left(\mathbf{k}_r, \mathbf{k}_t\right) \mathbf{z}\right|^2 \tag{3.22}$$

Additionally, with knowledge of the bi-directional covariance matrix, other multi-dimensional spectral estimation techniques can be used to estimate the bi-directional spectrum, many of which are described in [62]. Bi-directional beamforming forms a weighted sum of the bi-directional field sampled at the transmitter and receiver

locations. The bi-directional beamformer output is:

$$y = \sum_{n_r=1}^{N_r} \sum_{n_t=1}^{N_t} w_{n_r,n_t} s\left(\mathbf{x}_{rn_r}, \mathbf{x}_{tn_t}\right) \tag{3.23}$$

Substituting (3.12) into (3.23) and rearranging yields:

$$y = \int_{-\infty}^{\infty} F_s\left(\mathbf{k}_r, \mathbf{k}_t\right) F_w\left(\mathbf{k}_r, \mathbf{k}_t\right) d\mathbf{k}_r d\mathbf{k}_t \tag{3.24}$$

where

$$F_W\left(\mathbf{k}_r, \mathbf{k}_t\right) \equiv \sum_{n_r=1}^{N_r} \sum_{n_t=1}^{N_t} w_{n_r,n_t}^{*} \exp\left[j\left(\mathbf{k}_{rn}^T \mathbf{x}_r - \mathbf{k}_{tm}^T \mathbf{x}_t\right)\right] \tag{3.25}$$

is the bi-directional response for a given set of weights, and $S_w = |F_w|^2$ is the bi-directional beampattern. If the beamforming weights w_{n_r,n_t} are collected into a $N_r N_t$-length vector $\mathbf{w}$, then the bi-directional beampattern can be expressed as:

$$S_W\left(\mathbf{k}_r, \mathbf{k}_t\right) = \left|\mathbf{w}^H \mathbf{v}\left(\mathbf{k}_r, \mathbf{k}_t\right)\right|^2 \tag{3.26}$$

From (3.24) and (3.25), it is revealed that MIMO bi-directional beamforming is a realization of a bi-directional spatial filter, similar to the observation that beamforming has been shown to be a realization of a spatial filter [61]. In a given situation, the bi-directional spatial spectrum estimate can be used to characterize multipath propagations. However, a SIMO (single-input, multiple-output), which has multiple receiver channels but only one distinguishable transmitter channel, cannot distinguish multipath propagations from direct-path propagations. Note that the SIMO covariance matrix and data vector can be expressed as a transformation of the MIMO bi-directional covariance matrix:

$$\mathbf{R}_{SIMO} = \mathbf{H}\mathbf{R}_z\mathbf{H}^H \text{ and } \mathbf{z}_{SIMO} = \mathbf{H}\mathbf{z} \tag{3.27}$$

where the N_r-by-N_rN_t transformation matrix $\mathbf{H}$ is a horizontal concatenation of N_t N_r-by-N_r identity matrices:

$$\mathbf{H} = [\mathbf{I}_{N_r}\mathbf{I}_{N_r}\cdots\mathbf{I}_{N_r}] \tag{3.28}$$

Alternatively, the transformation matrix $\mathbf{H}$ could be defined as a matrix that only considers the data from a single transmitter element and ignores the others. The following transformation matrix deletes all data from all transmitter channels except for the first one:

$$\mathbf{H} = [\mathbf{I}_{N_r}\mathbf{0}\cdots\mathbf{0}] \tag{3.29}$$

In a SIMO system, the signals from the transmitter elements are not separable, so the sum of the return from all transmitter elements appear at each receiver element, and the system loses the ability to discriminate in transmit spatial frequency $\mathbf{k}_t$. Consider a scenario in which there are two transmit-receive propagation wavefronts. The first wavefront, $\mathbf{v}(\mathbf{k}_r = \mathbf{k_0}, \mathbf{k}_t = \mathbf{k}_0)$, is a direct-path wavefront in which $\mathbf{k}_r = \mathbf{k}_t$. The second wavefront $\mathbf{v}'(\mathbf{k}_r = \mathbf{k_0}, \mathbf{k}_t = \mathbf{k}_1)$, is a multi-path wavefront in which $\mathbf{k}_r \neq \mathbf{k}_t$. Note that both wavefronts have the same receive spatial frequency $\mathbf{k}_r$, but different transmit spatial frequencies $\mathbf{k}_t$. In a MIMO bi-directional system, these two wavefronts would be viewed as uncorrelated returns and they would appear as two distinct peaks in the bi-directional spectrum. In a SIMO system, which can only discriminate in $\mathbf{k}_r$, these two wavefronts would be indistinguishable and would appear as one peak on a one-dimensional spatial spectrum.

Additionally, the bi-directional beampattern can be formulated for any MIMO beamformer, whether or not the MIMO beamformer was designed for multipath suppression or under the framework described here. For example, another common use of MIMO co-located arrays is for aperture synthesis [35, 36, 50]. These applications are not concerned about multipath, but the bi-directional beampattern can be generated for these beamformers. Looking upon the "direct-path diagonal" (where $\mathbf{k}_r = \mathbf{k}_t$) of

the bi-directional beampattern provides the synthesized virtual one-directional array pattern for direct-path signals.

In this work, the bi-directional spectrum estimate will be used to characterize multipath propagation, and the bi-directional beampattern will be used to analyze the MIMO beamformers that are formulated to counteract the multipath. One particular useful application of the bi-directional spectrum is the ability to estimate the rank of the MIMO bi-directional covariance matrix.

3.3 Rank of the Bi-Directional Clutter Covariance Matrix

In the previous section, the concepts of the bi-directional spatial field and the bi-directional spatial spectrum were introduced. In chapter 4, a partially-adaptive algorithm for multipath clutter mitigation will be introduced. A key factor in the feasibility of any partially adaptive algorithm is the rank of the interference covariance matrix, as the interference rank determines the number of adaptive degrees of freedom needed to suppress it. Ideally, the number of adaptive degrees of freedom should be greater than or equal to the rank of the clutter covariance matrix. Due to the fact that multipath models are highly environment-dependent, it is unlikely to be able to derive a simple formula for the rank of the multipath clutter, such as Brennan's rule [63] for direct-path clutter in SIMO STAP. In this section, a method for approximating the rank of the clutter covariance using the bi-directional spatial spectrum is presented. In [64] and [59], a method to estimate the clutter rank for unusual geometries or array shapes is presented by counting the number of resolution cells occupied in the spatial spectrum. In this section this technique will be used in conjunction with the bi-directional spatial spectrum to estimate the rank of the bi-directional clutter covariance matrix.

Consider a system with a linear receive array with aperture L_r and a linear transmit array with aperture L_t. Since both arrays are one-dimensional, the spa-

tial frequency vectors can be represented with scalar values (i.e. $\mathbf{k}_r = (k_{rx}, 0, 0)^T$ and $\mathbf{k}_t = (k_{tx}, 0, 0)^T$). It is useful to consider the normalized spatial frequencies, $\hat{k}_{rx} = \frac{k_{rx}\lambda}{2\pi}$ and $\hat{k}_{tx} = \frac{k_{tx}\lambda}{2\pi}$, because the normalized spatial frequencies within $[-1, 1]$ correspond to the visible region, that is, the region of spatial frequencies that correspond to physical propagating waves. The normalized receive spatial frequency resolution is $\mu_r = \frac{\lambda}{L_r}$ and the normalized transmit spatial frequency resolution is $\mu_t = \frac{\lambda}{L_t}$. There are $\eta_r = \text{ceil}\left(\frac{2}{\mu_r}\right) = \text{ceil}\left(\frac{2L_r}{\lambda}\right)$ receive resolution cells and $\eta_t = \text{ceil}\left(\frac{2}{\mu_t}\right) = \text{ceil}\left(\frac{2L_t}{\lambda}\right)$ transmit resolution cells. The l_r^{th} receive resolution cell spans

$$\hat{k}_{rx,lr} \in [-1 + (l_r - 1)\,\mu_r, -1 + l_r\mu_r] \tag{3.30}$$

and the l_t^{th} transmit resolution cell spans

$$\hat{k}_{tx,lt} \in [-1 + (l_t - 1)\,\mu_t, -1 + l_t\mu_t] \tag{3.31}$$

In bi-directional space, the transmit and receive resolution cells overlay to create a grid with $\eta_r\eta_t$ rectangular cells. The rectangular cell formed by the l_r^{th} receive cell and the l_t^{th} transmit cell can be isolated using the mask function

$$K_{lr,lt}\left(\hat{k}_{rx}, \hat{k}_{tx}\right) = \begin{cases} 1 & \text{if } \hat{k}_{rx} \in \hat{k}_{rx,lr} \text{ and } \hat{k}_{tx} \in \hat{k}_{tx,lt} \\ 0 & \text{otherwise} \end{cases} \tag{3.32}$$

For each rectangular cell, define an indicator function $G\,(l_r, l_t)$ which compares the maximum value of the bi-directional spectrum (from (3.21) or (3.22)) within that cell to a threshold Γ:

$$G\,(l_r, l_t) = \begin{cases} 1 \text{ if } \max\left(K_{lr,lt}(\hat{k}_{rx}, \hat{k}_{tx})\hat{S}(\hat{k}_{rx}, \hat{k}_{tx})\right) > \Gamma \\ 0 \text{ otherwise} \end{cases} \tag{3.33}$$

An estimate for the rank of the covariance matrix can be formed by summing the

indicator functions $G(l_r, l_t)$ for each of the $\eta_r \eta_t$ rectangular resolution cells:

$$\hat{\rho} = \sum_{l_r=1}^{\eta_r} \sum_{l_t=1}^{\eta_t} G(l_r, l_t) \tag{3.34}$$

3.4 Example Scenario and Clutter Rank Estimation

To illustrate the estimation of clutter rank, consider a forward-looking radar parallel to a long, specular reflector, as shown in Fig. 3.2. The specular reflector is assumed to be infinite in extent, and have a height that is equal to or greater than the height of the radar. The ground is assumed to be a rough surface. The radar is a MIMO system with both a forward-looking transmit and receive array. In Cartesian coordinates, define the receive array to be centered at $(x = 0, y = 0, z = z_r)$. Define the transmit array to centered at $(x = 0, y = 0, z = z_t)$ and the diffuse ground to be the plane of $(z = 0)$. The specular reflector at $(x = x_s)$ is assumed infinite extent in the y-domain, and in the z-domain runs from the ground $(z = 0)$ to a height greater than or equal to maximum height of the arrays $(z \geqslant \max(z_r, z_t))$. It will also be assumed that the transmit antennas, the receive antennas, or both set of antennas have significant attenuation in their backlobes and therefore no energy will be transmitted or received to/from the area behind the radar. Define the transmit azimuth angle ϕ_t and receive azimuth angle ϕ_r to the be the angles relative to the line $(x = 0)$ in the xy plane. In this frame of reference, the azimuth angle $(\phi = 0)$ refers to the $+y$ direction, the azimuth angle $(\phi = +\frac{\pi}{2})$ refers to the $+x$ direction, and the azimuth angle $(\phi = -\frac{\pi}{2})$ refers to the $-x$ direction. The vehicle is assumed to be traveling in the $+y$ direction at a constant velocity of v.

Clutter can be divided into direct-path clutter and multipath clutter, as in (3.6). Direct path clutter is the simplest to characterize, as the transmit and receive azimuth angles are equal to each other: $\phi_{rx} = \phi_{tx}$. However, direct-path clutter only exists when the departing ray scatters off of the rough ground. If the departing ray reflects

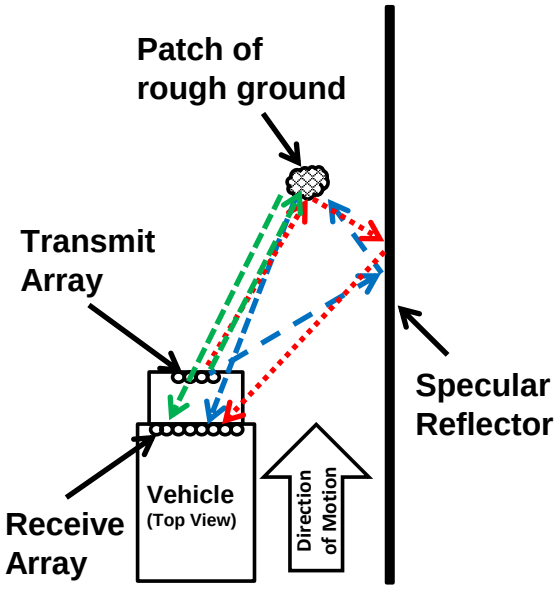

FIGURE 3.2: Vehicle Driving Next to a Specular Reflector

off of the specular reflector, then it will not arrive at the receiver along the same path, as the specular reflector only scatters forward and there is no backscatter. Direct-path clutter will exist when the following condition is met:

$$\sin(\phi_{tx}) \leqslant \frac{4x_s r}{\sqrt{\left((2r)^2 - (z_r - z_t)^2\right)\left((2r)^2 - (z_r + z_t)^2\right)}} \tag{3.35}$$

In locations where direct-path clutter exists, and assuming $(z_r - z_t)$ small, the Doppler shift of the clutter is:

$$f_d = 2\frac{v}{\lambda}\cos(\phi_{tx})\sqrt{1 - \frac{\left(\frac{z_t + z_r}{2}\right)^2}{r^2}} \tag{3.36}$$

Multipath clutter that first reflects off of the specular reflector and then scatters off of the rough ground exists when the conditions $(\phi_{tx} > 0)$ AND $(\phi_{rx} < \phi_{tx})$ AND $(\phi_{rx} > -\phi_{tx})$ are met, and is described by:

$$r = \frac{x_s\sqrt{1+\frac{z_t^2\cos^2\phi_{tx}}{4x_s^2}\left(\tan\phi_{rx}+\tan\phi_{tx}\right)^2}}{\left|\cos\phi_{tx}\left(\tan\phi_{rx}+\tan\phi_{tx}\right)\right|} \tag{3.37}$$

$$+\frac{1}{2}\sqrt{4x_s^2-\frac{8x_s^2\tan\phi_{tx}}{\tan\phi_{rx}+\tan\phi_{tx}}+\frac{4x_s^2}{\cos^2\phi_{rx}\left(\tan\phi_{rx}+\tan\phi_{tx}\right)^2}+z_r^2}$$

exists for $(\phi_{tx} > 0)$ AND $(\phi_{rx} < \phi_{tx})$ AND $(\phi_{rx} > -\phi_{tx})$

In locations where this type of multipath exists, the Doppler shift of this type of multipath clutter is:

$$f_d = \frac{v}{\lambda}\left(\frac{2x_s\cos\phi_{tx}}{\sqrt{4x_s^2+z_t^2\cos^2\phi_{tx}\left(\tan\phi_{rx}+\tan\phi_{tx}\right)^2}}\right. \tag{3.38}$$

$$\left.+\frac{\cos\phi_{rx}}{\sqrt{1+\frac{z_r^2\cos^2\phi_{rx}\left(\tan\phi_{rx}+\tan\phi_{tx}\right)^2}{4x_s^2\left(\cos^2\phi_{rx}\left(\tan\phi_{rx}+\tan\phi_{tx}\right)^2-2\tan\phi_{tx}\cos^2\phi_{rx}\left(\tan\phi_{rx}+\tan\phi_{tx}\right)+1\right)}}}\right)$$

Multipath clutter that first scatters off of the rough ground and then reflects off of the specular reflector exists when the conditions $(\phi_{rx} > 0)$ AND $(\phi_{rx} > \phi_{tx})$ AND $(\phi_{rx} > -\phi_{tx})$ are met, and is described by:

$$r = \frac{1}{2}\sqrt{\frac{4x_s^2}{\cos^2\phi_{tx}\left(\tan\phi_{rx}+\tan\phi_{tx}\right)^2}+z_t^2} \tag{3.39}$$

$$+\frac{1}{2}\left|\frac{\left(\tan\phi_{rx}-\tan\phi_{tx}\right)}{\tan\phi_{rx}\left(\tan\phi_{rx}+\tan\phi_{tx}\right)}\right|\sqrt{x_s^2\left(\tan^2\phi_{rx}+1\right)+z_r^2\left(\tan\phi_{rx}+\tan\phi_{tx}\right)^2}$$

$$+\frac{1}{2}\sqrt{x_s^2+\frac{x_s^2+z_r^2\tan^2\phi_{tx}}{\tan^2\phi_{rx}}}$$

exists for $(\phi_{rx} > 0)$ AND $(\phi_{rx} > \phi_{tx})$ AND $(\phi_{rx} > -\phi_{tx})$

In locations where this type of multipath exists, the Doppler shift of this type of multipath clutter is described by:

$$f_d = \frac{v}{\lambda}\left(\frac{2x_s\cos\phi_{tx}}{\sqrt{4x_s^2 + z_t^2\cos^2\phi_{tx}\left(\tan\phi_{rx}+\tan\phi_{tx}\right)^2}} + \frac{x_s\cos\phi_{rx}}{\sqrt{x_s^2 + z_r^2\tan^2\phi_{tx}\cos^2\phi_{rx}}}\right) \tag{3.40}$$

Minimal energy loss occurs during reflections off of the specular reflector and thus these two dominant multipath clutter paths will have almost the same energy as direct-path clutter scattering off of the ground with similar path lengths. Higher-order multipath paths involving multiple scatterings off of the ground have much less energy and are therefore ignored. In the examples illustrated here, the receive array is a uniform linear array with $N_r = 16$ elements and an element spacing of $\frac{\lambda}{2}$. The transmit array is a uniform linear array with $N_t = 8$ elements and an element spacing of $\frac{\lambda}{2}$. The locations of the specular reflector is $x_s = 5$ m. The height of the arrays above the ground are $z_t = 1.25$ m and $z_r = 1.5$ m. The velocity of the vehicle is $v = 11$ m/s (approximately 25 mph). Some example plots of the bi-directional clutter loci representing this multipath geometry are shown in Fig. 3.4 for ranges of 10 m, 15 m, 30 m, and 50 m. Observe that the clutter loci vary with range, which makes MIMO operation a good choice for clutter suppression.

With this unusual and range-varying geometry a simple estimate for clutter rank estimation can be obtained using the rank estimate from (3.34). The appropriate resolution cell gridlines from (3.32) have been imposed on Fig. 3.4 which show the clutter loci. In particular, the clutter rank estimate of (3.34) corresponds to counting the number of occupied resolution cells, with sizes defined by (3.32). The eigenspectra of the clutter covariance matrix corresponding to the loci of Fig. 3.4 is shown in Fig. 3.4. The rank estimates by counting the resolution cells are shown as vertical

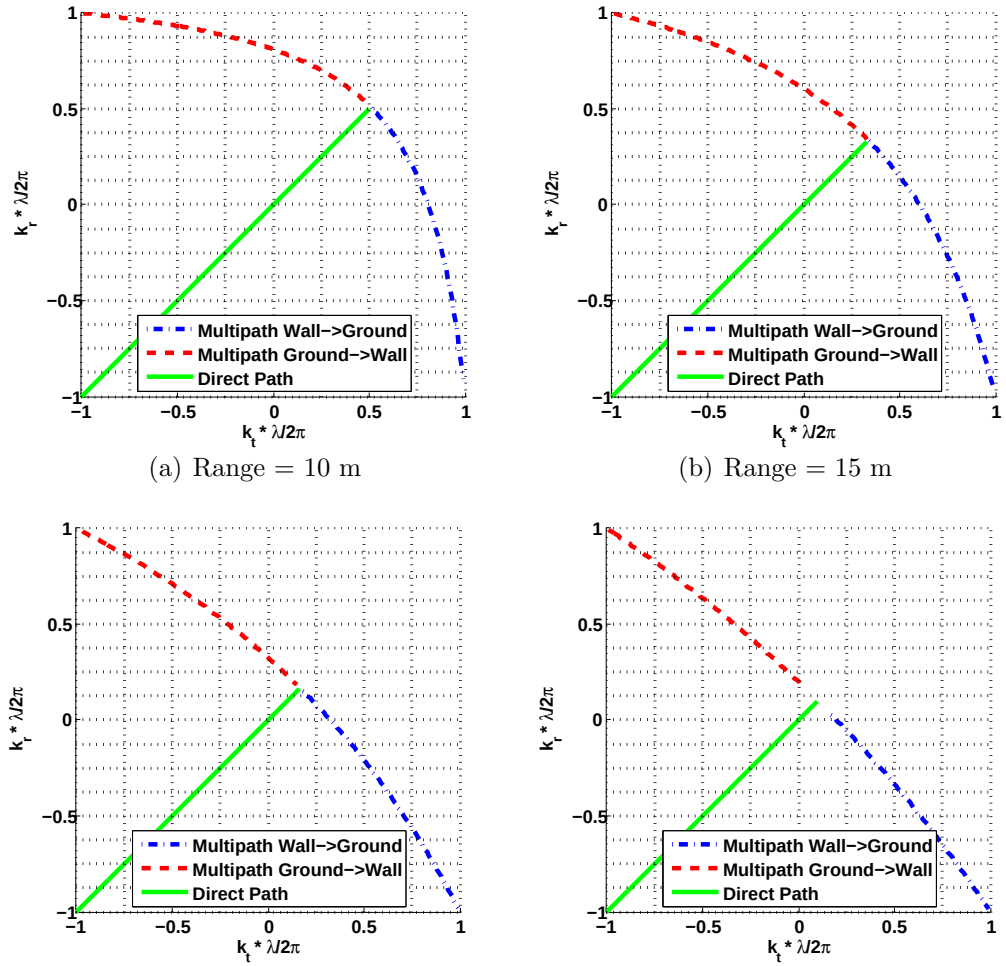

(a) Range = 10 m

(b) Range = 15 m

(c) Range = 30 m

(d) Range = 50 m

FIGURE 3.3: Bi-directional Clutter Loci

lines. Observe that for each range the rank estimate is very close to the number of significant eigenvalues. Note that for each range the number of significant eigenvalues is less than 40 (out of a maximum 128) and therefore the clutter covariance matrix is approximately low rank. However, the rank is higher than the degrees of freedom that would be available if transmit and receive beamforming were performed independently, which corresponds to a Kronecker MIMO beamformer of the form $\mathbf{w} = \mathbf{w}_t \otimes \mathbf{w}_r$. The number of degrees of freedom in the Kronecker beamformer is $N_r + N_t$. In this particular example, $N_r = 16$ and $N_t = 8$, and therefore $N_r + N_t = 24$,

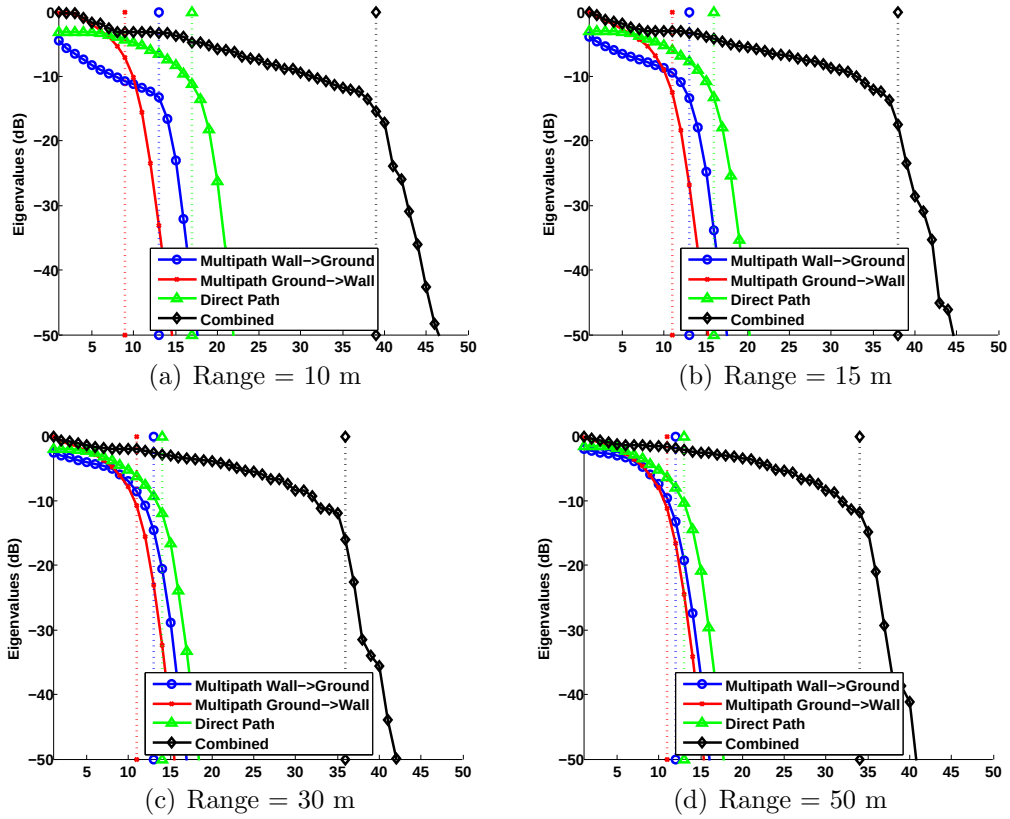

(a) Range = 10 m (b) Range = 15 m

(c) Range = 30 m (d) Range = 50 m

FIGURE 3.4: Clutter Eigenspectrum

which is less than the rank of the clutter covariance matrix. In this example, the low rank of the clutter covariance matrix indicates the number of partially adaptive bi-directional beamforming weights required to most effectively suppress clutter, i.e. greater than or equal to the rank of the clutter covariance matrix.

3.5 Summary

The MIMO signal model was defined. The concept of the MIMO bi-directional spectrum was introduced and defined, which allows for the characterization of multipath, and leads to a technique to estimate the rank of the clutter covariance matrix. In the next chapter, a partially adaptive algorithm will be developed to suppress multipath clutter, using the rank estimation developed here.

4

Partially Adaptive MIMO Bi-directional Beamforming for Multipath Clutter Suppression in Ground-Vehicle GMTI

Consider again the example problem described in Chapter 3, Section 4: a radar mounted on a ground vehicle driving parallel to a specular reflector. The illustrative figure of Fig. 3.2 is reprinted here in Fig. 4.1 for the reader's convenience. The goal of the radar is to perform GMTI (ground-moving-target-indicator) to detect moving targets, such as pedestrians. However, obstacles such as parked cars, highway guardrails, and building walls in combination with reflections off of the ground produce many multipath clutter returns. Since the vehicle is moving, these returns are spread in Doppler, and may mask a legitimate target or appear as false targets. However, the previous chapter that multipath returns can be separated from direct-path returns via the bi-directional spatial spectrum. Therefore, an adaptive bi-directional beamformer could be designed to suppress the multipath. One major issue with MIMO radar is the that the large number of degrees of freedom requires a large amount of training data to estimate interference statistics. This issue is especially exacerbated on moving platforms, since the environment rapidly changes and

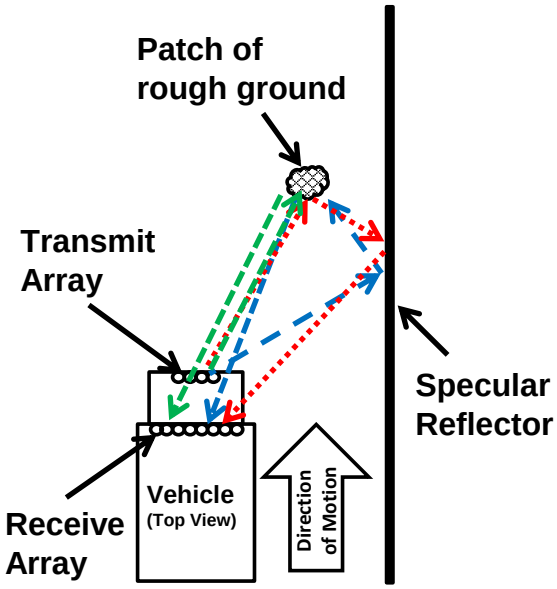

FIGURE 4.1: Vehicle Driving Next to a Specular Reflector

therefore there is limited available time to collect snapshots.. However, the previous chapter demonstrated that the clutter in this scenario is significantly rank deficient in the bi-directional spatial domain, and therefore not all the degrees of freedom are required to suppress the multipath clutter. This chapter proposes a partially adaptive bi-directional beamformer to suppress multipath returns, and simulation results are presented. (In Chapter 7, experimental results from a real radar testbed are shown).

4.1 Partially Adaptive Algorithm

From Chapter 3, we have the ability to estimate the rank of the clutter covariance matrix with the MIMO bi-directional spatial spectrum. Since this rank is significantly less than the dimension of the bi-directional clutter covariance matrix (also shown in Chapter), a partially adaptive algorithm for multipath clutter suppression is appropriate and will be developed here. If complete omniscient knowledge of the clutter and noise covariance matrices were available, then the optimum MIMO

beamformer would be:

$$\mathbf{w}_{opt} = \mathbf{R}_I^{-1}\mathbf{v} \tag{4.1}$$

where $\mathbf{R}_I$ is the target-free covariance matrix from (3.7). In practice, the target-free covariance matrix is not known. The covariance matrix must be estimated from data snapshots. As stated previously, in situations involving range-varying multipath clutter, the standard practice of training over adjacent range bins in not appropriate. Instead, slow-time pulses at the range bin under test will be used as training snapshots. The simplest approach would be to use the sample covariance matrix generated from slow-time pulses:

$$\hat{\mathbf{R}}_z = \frac{1}{M}\sum_{m=1}^{M}\mathbf{z}_m\mathbf{z}_m^H \tag{4.2}$$

where M is the number of pulses and $\mathbf{z}$ is the data vector from (3.5). Given the large size of the bi-directional covariance matrix (N_rN_t by N_rN_t), a very large number of snapshots would be needed to support this fully adaptive solution, which motivates the need for a partially-adaptive solution with reduced adaptive the degrees of freedom and hence fewer number of snapshots required. The proposed solution takes the form of a reduced-rank generalized sidelobe canceller. The generalized sidelobe canceller [65] consists of a set of non-adaptive quiescent weights to form the mainbeam and set of adaptive weights to cancel the interference. A blocking matrix is applied to the adaptive training data which removes the desired signal. Without a blocking matrix, training data formed from slow-time pulses will include the target signal, and therefore the blocking matrix is necessary. To reduce the number of adaptive degrees of freedom, a projection matrix is applied to transform the data into a lower-rank subspace. A block diagram of this structure in shown in Fig. 4.2. A similar approach has been proposed for partially adaptive algorithm for SIMO STAP in [66–68].

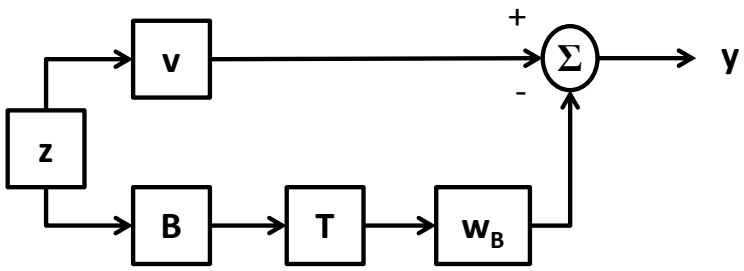

FIGURE 4.2: Reduced Rank Generalized Sidelobe Canceller Structure

To compute partially adaptive weights, consider the bi-directional steering vector defined in (3.3). The length of the bi-directional wavefront vector $\mathbf{v}(\mathbf{k}_r, \mathbf{k}_t)$ is $N_r N_t$-by-1. To avoid cancellation, the blocking matrix $\mathbf{B}$ must be chosen such that $\mathbf{Bv} = 0$. The dimension of the blocking matrix $\mathbf{B}$ is thus $(N_r N_t - 1)$-by-$N_r N_t$. At a minimum, the blocking matrix must be an orthonormal matrix which excludes the subspace of $\mathbf{v}$, however, more information can be used in its design, which is discussed in the next subsection. Without a transformation matrix, the fully adaptive two-dimensional generalized sidelobe canceller (GSC) beamforming weights [65] are given by :

$$\mathbf{w}_b = \left(\mathbf{B}\hat{\mathbf{R}}_z\mathbf{B}^H\right)^{-1}\mathbf{B}\hat{\mathbf{R}}_z\mathbf{v}$$

$$\mathbf{w}_{GSC} = \mathbf{v} - \mathbf{B}^H\mathbf{w}_b \tag{4.3}$$

The number of adaptive degrees of freedom in (4.3) is $N_r N_t - 1$. In the previous section, however, it was shown that the rank of clutter covariance matrix is much lower than $N_r N_t$, and a method was proposed to estimate this rank based on the environmental scenario. Assume it is known that the rank of the clutter covariance matrix is less than or equal to P. Then, the $(N_r N_T - 1)$-by-P transformation matrix $\mathbf{T}$ can be used to reduce the dimensionality of the data to P, the reduced number of adaptive degrees of freedom. Since the number of snapshots required for stable estimates of the weights is roughly twice the number of adaptive degrees of freedom, the partially adaptive weights save not only computation but also can be estimated with less training data than fully adaptive methods using (4.2).

The weights for the reduced subspace two-dimensional generalized sidelobe canceller are:

$$\mathbf{w}_t = \left(\mathbf{T}^H \mathbf{B}\hat{\mathbf{R}}_z \mathbf{B}^H \mathbf{T}\right)^{-1} \mathbf{T}^H \mathbf{B}\hat{\mathbf{R}}_z \mathbf{v}$$

$$\mathbf{w}_{GSC,P} = \mathbf{v} - \mathbf{B}^H \mathbf{T}\mathbf{w}_t \tag{4.4}$$

The transformation matrix $\mathbf{T}$ must be chosen to span the subspace of the clutter. In [66–68] it was shown that the optimum (in terms of signal-to-interference-plus-noise ratio) choice of the transformation matrix $\mathbf{T}$ consists of selecting eigenvectors of the blocked covariance matrix, $\mathbf{R}_b = \mathbf{B}\hat{\mathbf{R}}_z\mathbf{B}^H$, and the most effective adaptive cancellation is obtained using eigenvectors chosen which have the highest cross-spectral values, i.e. contribution to look direction components. The eigendecomposition of $\mathbf{R}_b$ is:

$$\mathbf{R}_b = \mathbf{U}\mathbf{\Lambda}\mathbf{U}^{-1} \tag{4.5}$$

The columns of $\mathbf{U}$ are the eigenvectors of $\mathbf{R}_b$, and $\mathbf{\Lambda}$ is a diagonal matrix containing the eigenvalues of $\mathbf{R}_b$. The ith cross-spectral value q_i is defined as:

$$q_i = \left| \frac{\mathbf{u}_i^H \mathbf{B}\hat{\mathbf{R}}_z \mathbf{v}}{\sqrt{\lambda_i}} \right|^2 \tag{4.6}$$

where $\mathbf{u}_i$and λ_i are the ith eigenvector and eigenvalue of the blocked covariance matrix, $\mathbf{B}\hat{\mathbf{R}}_z\mathbf{B}^H$. The cross-spectral values represent the strength of each interference eigenvector after taking the inner product with the steering direction vector. The columns of the projection matrix $\mathbf{T}$ are the P eigenvectors with the highest cross-spectral values:

$$\mathbf{T} = [\mathbf{u}_{q1}, \mathbf{u}_{q2}, \ldots, \mathbf{u}_{qP}] \tag{4.7}$$

To maintain optimality, the transformation matrix $\mathbf{T}$ of (4.7) must be re-calculated for each new set of training data. More discussion and a formal proof of the optimality of the cross-spectral values can be found in [66–68].

4.1.1 Blocking Matrix Choice

One way to calculate the blocking matrix $\mathbf{B}$ is to use the singular value decomposition (SVD) to find the projection matrix onto the orthogonal subspace $\mathbf{v}$:

$$[\mathbf{U}, \mathbf{S}, \mathbf{V}] = \text{svd}(\mathbf{v})$$
$$\mathbf{B} = [\mathbf{U}(:, 2 : N_r N_T)] \tag{4.8}$$

Note that the eigenvectors corresponding to null space of $\mathbf{v}$ are selected. In practice, the signal wavefront is imperfectly known so it may be necessary to use a more robust blocking matrix $\mathbf{B}$ to prevent nulling of the signal in the training data. If portions of the signal in the look direction remain after applying $\mathbf{B}$, the beamformer may attempt to place a null in the mainlobe. Additionally, if there are clutter components close to the desired transmit-receive look direction (which would by definition be direct-path or near direct-path clutter components), the adaptive beamformer will attempt to place nulls near the mainbeam, which may also null the signal. A more robust blocking matrix can be calculated from:

$$[\mathbf{U}, \mathbf{S}, \mathbf{V}] = \text{svd}([\mathbf{v}_1 \mathbf{v}_2 \dots \mathbf{v}_K])$$
$$\mathbf{B} = [\mathbf{U}(:, K + 1 : N_r N_T)] \tag{4.9}$$

where the steering vectors $\mathbf{v}_1, \mathbf{v}_2, \dots, \mathbf{v}_K$ are wavefront vectors at the desired steering point and at neighboring transmit and receive spatial frequencies "close" to the desired steering point. "Close" refers to transmit and receive spatial frequencies of neighboring transmit-receive resolution cells, defined in (3.32). Since all desired steering directions will be along the direct-path $\mathbf{k}_t = \mathbf{k_r}$, the additional vectors $\mathbf{v}_2, \dots, \mathbf{v}_K$ should have the property $\mathbf{k}_t \approx \mathbf{k}_r$. If there is mismatch, the original blocking matrix in (4.8) may allow the signal through to the adaptive calculation, causing nulls near or in the main beam. The same result will occur if there are clutter components very close to the desired transmit-receive look direction. The

matrix in (4.9), however, will be less sensitive to mismatch and will filter out nearby clutter components. By adding more constraints to the blocking matrix, the adaptive degrees of freedom are reduced by K, before the rank-reduction matrix. However, typically for MIMO applications the remaining number of adaptive degrees of freedom is still much larger than the clutter rank P.

4.1.2 Algorithm Summary

The complete algorithm will now be summarized. First, form the sample covariance matrix from slow-time pulses as shown in (4.2). For a given scenario, an estimate of the bi-directional spectrum can be obtained using (3.21) and the clutter rank, P, can be estimated using (3.34). For partially adaptive MIMO beamforming, the blocking matrix $\mathbf{B}$ of (4.8) or (4.9) can be used and the optimum transformation matrix $\mathbf{T}$ can be obtained using (4.5), (4.6), and (4.7). Finally, the partially adaptive weights $\mathbf{w}_{GSC,P}$ are computed using (4.4) and applied to the data $\mathbf{z}$ from (3.5).

4.2 Simulation Results

To demonstrate the performance of partially adaptive bi-directional MIMO beamforming, return to the multipath scenario described at the beginning of this chapter: a forward-looking radar above the ground next to a specular reflector. Let the radar be mounted on a ground vehicle driving parallel to the specular reflector, and let there be a pedestrian who is walking across the street. The goal of the radar is to detect the pedestrian and alert the driver of his position. Because the pedestrian is moving, he will be separated in Doppler from the direct-path clutter but is assumed to be at the same slant range (or delay). However, Doppler-spread multipath clutter can obscure the pedestrian and thus must be suppressed. For this simulation, to match the radar testbed that will be introduced in Chapter 6, the carrier frequency is 2.4 GHz, and therefore the wavelength is 12.5 cm. The receive array has 16 elements,

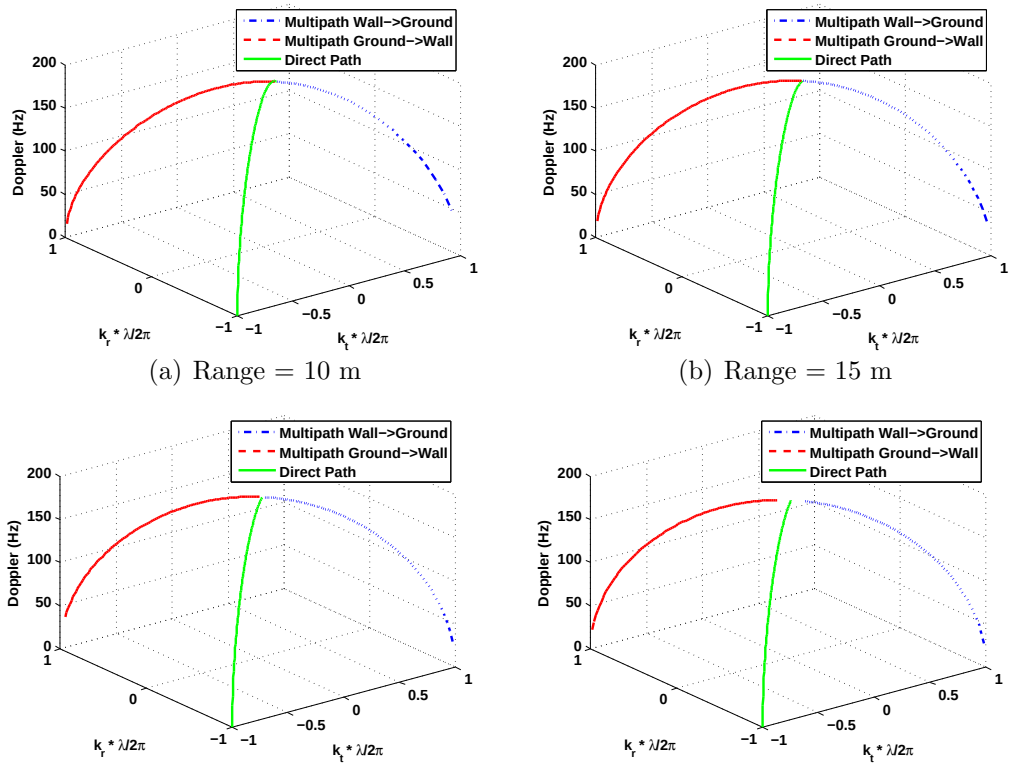

(a) Range = 10 m

(b) Range = 15 m

(c) Range = 30 m

(d) Range = 50 m

FIGURE 4.3: Bi-directional Spatial-Doppler Clutter Loci

spaced at $\frac{\lambda}{2}$, and is centered at $(x = 0, y = 0, z = 1.5 \text{ m})$. The transmit array has 8 elements, spaced at $\frac{\lambda}{2}$, and is centered at $(x = 0, y = 0, z = 1.25 \text{ m})$. The wall exists at $(x = 4 \text{ m})$. The vehicle is driving at a constant velocity of 11 m/s (approximately 25 mph) in the $+y$ direction. The transmit and receive antennas are assumed to have mainlobes which encompass $\pm 90^o$ from the forward direction, $\phi = 0$. For other radar parameters, assume that after MIMO channel separation, the effective waveform repetition frequency (WRF) is 400 Hz (if slow-time MIMO waveforms are the MIMO waveform choice, then the WRF before MIMO channel separation must be $N_t \times f_{wrf,ef}$ where $f_{wrf,ef}$ is the effective WRF. Refer back to Chapter 2 for more information). The coherent integration time (CIT) is 0.25 seconds. There is a moving target at a range of 15 m at an azimuth angle of -10 degrees ($k_x = \sin\phi = -0.1736$), moving at a slant velocity of 2.25 m/s (approximately 5 mph) away from the vehicle,

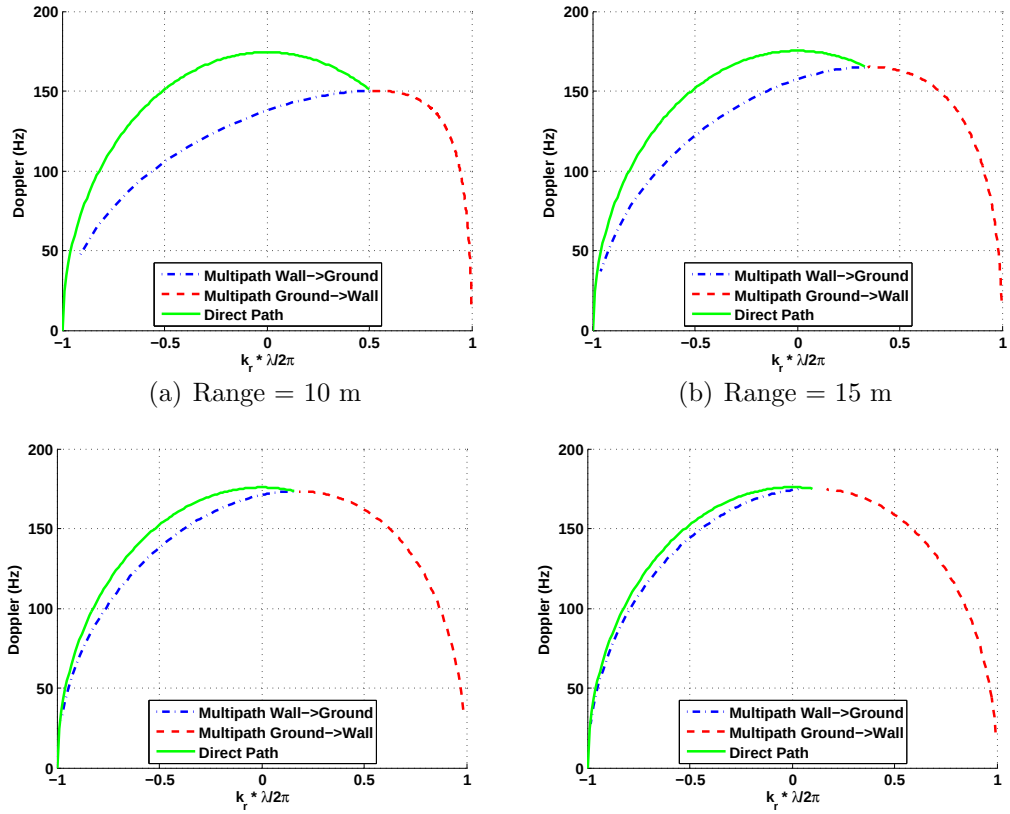

(a) Range = 10 m (b) Range = 15 m

(c) Range = 30 m (d) Range = 50 m

FIGURE 4.4: SIMO Uni-directional Spatial-Doppler Clutter Loci

for a net velocity relative to the vehicle of 8.75 m/s (which corresponds to a Doppler shift of 140 Hz). In the MIMO case, the clutter-to-noise ratio (CNR) is 30 dB and the signal-to-noise ratio (SNR) is 10 dB. In the SIMO case, to account for the MIMO SNR loss, the CNR increases to 39 dB and the SNR increases to 19 dB.

Define the transmit azimuth angle ϕ_t and receive azimuth angle ϕ_r to the be the angles relative to the line $(x = 0)$ in the xy plane. In this frame of reference, the azimuth angle $(\phi = 0)$ refers to the $+y$ direction, the azimuth angle $(\phi = +\frac{\pi}{2})$ refers to the $+x$ direction, and the azimuth angle $(\phi = -\frac{\pi}{2})$ refers to the $-x$ direction. The clutter bi-directional spatial spectrum for this scenario was previously shown in Fig. 3.3(b). Since the radar is now on a moving platform, the clutter is now Doppler spread. Fig. 4.2 illustrates the bi-directional-space-time relationship

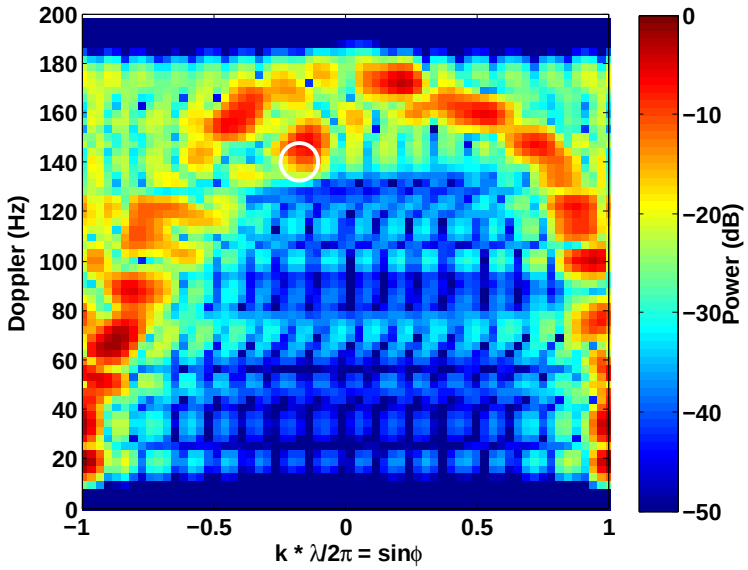

FIGURE 4.5: SIMO Doppler-azimuth with known covariance matrix

between transmit angle, receive angle, and Doppler shift for ranges of 10 m, 15 m, 30 m, and 50 m. Fig. 4.2 shows how a SIMO radar would see the SIMO-space-time relationship between receive angle and Doppler shift for the same set of ranges. Observe that the SIMO views of Fig. 4.2 are projections of the three-dimensional spaces of Fig. 4.2 onto a two-dimensional surface, and that in SIMO view there is no method to distinguish between direct-path and multipath clutter. Mathematical expressions for these curves were previously presented in Chapter 3, Section 4.

4.2.1 Known Covariance Matrices

First, for both MIMO and SIMO, bi-directional spectra and clutter suppression with known covariances are considered. Figure 4.5 shows the result from adaptive SIMO beamforming. For SIMO beamforming, a fully adaptive generalized sidelobe canceller [65] was employed on the receive side array only using the maximum number ($N_r - 1 = 15$) of adaptive degrees of freedom available. Observe that the target cannot be distinguished due to the multipath clutter components. Figure 4.6 shows the result from adaptive MIMO bi-directional beamforming with 40 adaptive degrees

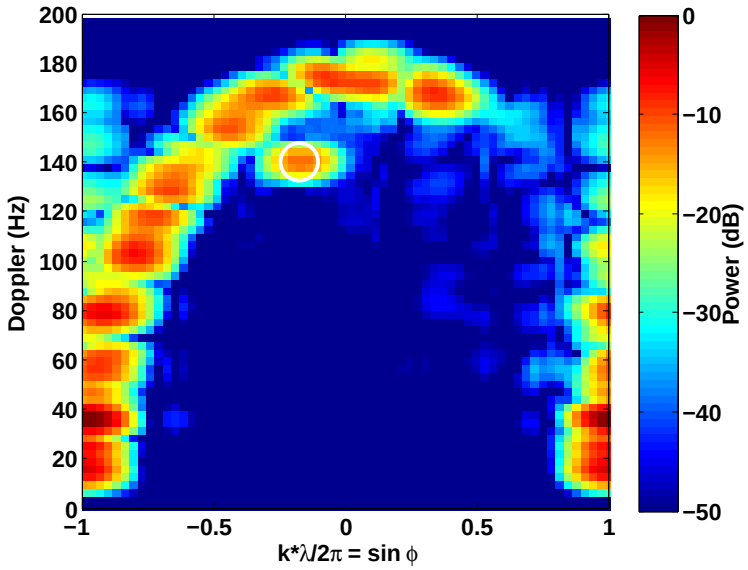

FIGURE 4.6: MIMO Doppler-azimuth with known covariance matrix

of freedom. 40 adaptive degrees of freedom were chosen because the clutter rank estimate of (3.34) predicted that the clutter rank would be less than or equal to 40. Note that the multipath clutter is suppressed and the target is detectable away from the direct-path clutter ridge. Comparing these two figures to the the clutter loci in Figure 4.4(b), note that the although target falls along one of the multipath clutter loci, the MIMO beamformer is able to discriminate it while the SIMO beamformer cannot.

In the MIMO case, the bi-directional spatial spectrum from (3.21) and the bi-directional spatial beampattern from (3.25), are shown in Fig. 4.2.1 and Fig. 4.2.1 respectively. Notice that Fig. 4.2.1 has the same shape as the clutter loci from Fig. 3.3(b). The bi-directional spatial beampattern is shown in Fig. 4.2.1. Observe that it places sharp nulls along the clutter loci.

4.2.2 Estimated Covariance Matrices

Here the more realistic case where the covariance matrix is unknown and must be estimated from the received data is considered. The covariance matrix is estimated

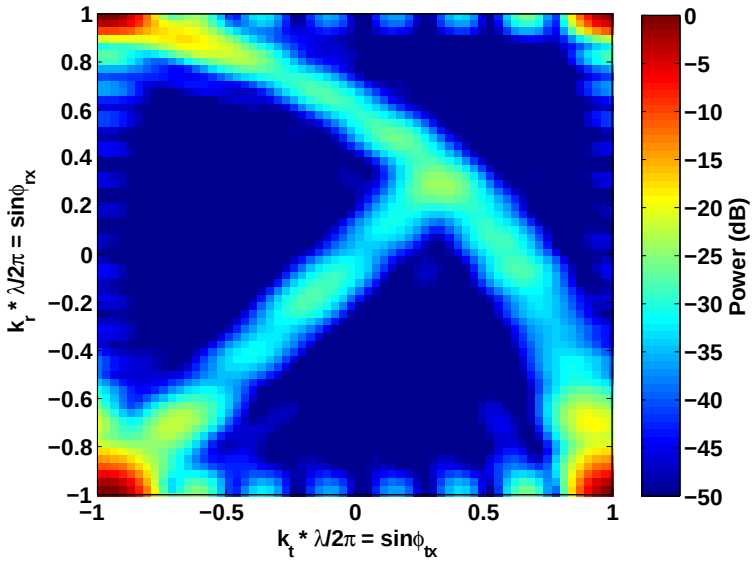

FIGURE 4.7: Bi-Directional Spatial Spectrum

by training over slow-time pulses as in (4.2). The full CIT of 0.25 seconds, providing $M = 100$ snapshots, is used as training data. Fig. 4.2.2 shows the SIMO result. Observe that the MIMO result is still able to identify the target. Fig. 4.2.2 shows the partially adaptive MIMO result. The clutter rank estimate P of (3.34) was computed to be approximately 40. Because of direct-path clutter near the target in the bi-directional spectrum, the robust blocking matrix $\mathbf{B}$ of (4.9) was used, choosing nearby direct-path steering vectors along with the target direction to block. The transformation matrix $\mathbf{T}$ was designed using the process from (4.5), (4.6) and (4.7) and with $P = 40$ adaptive degrees of freedom. The partially adaptive MIMO result still clearly discriminates the target, although the noise floor has been raised versus the known covariance case. The MIMO adaptive bi-directional beampattern from (3.25) is shown in Fig. 4.2.2. It is no longer able to place ideal nulls along the clutter, although it nulls the multipath clutter enough to get the result shown in Figure 4.2.2. However, the MIMO bi-directional beamforming still drastically outperforms SIMO beamforming.

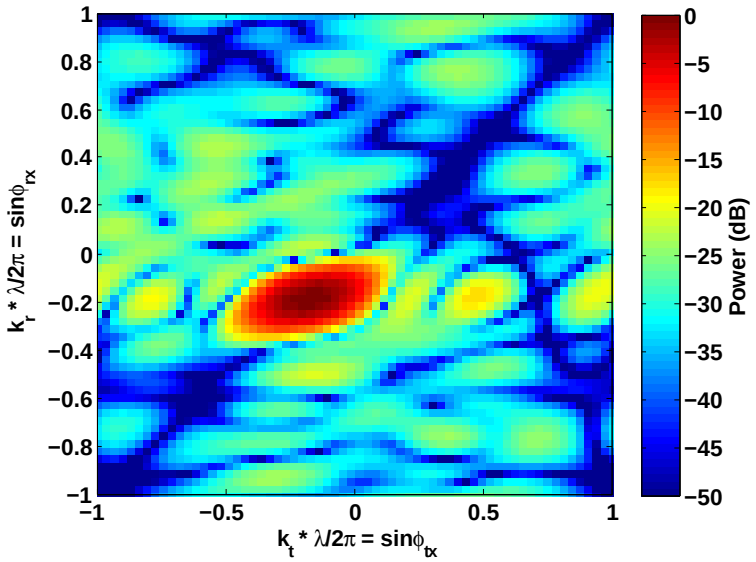

FIGURE 4.8: Bi-directional Beampattern: Known Covariance Matrix

4.2.3 Monte Carlo Detection Results

To statistically determine how the number of snapshots affects the performance of the MIMO bi-directional adaptive beamformer, and to compare the MIMO bi-directional beamformer to the SIMO beamformer, Monte Carlo trials were performed and receiver operating characteristics (ROCs) were generated. Four cases were run and 500 realizations were generated for each case. The first three cases tested the partially adaptive MIMO beamformer training over slow-time pulses. The CIT was varied to vary the number of snapshots available. Case 1 tested the performance with 100 snapshots (CIT = 0.250 s), case 2 tested the performance with 80 snapshots, (CIT = 0.200 s), and case 3 tested the performance with 50 snapshots (CIT = 0.125 s). As before, $P = 40$ adaptive degrees of freedom were used. The fourth case tested the fully adaptive SIMO beamformer with a known covariance matrix, as this should provide the upper-bound for SIMO performance. The full CIT = 0.250 s was used for the SIMO case. The resulting ROC curves are shown in Fig. 4.12. Observe how all of the MIMO cases perform much better than SIMO, even though the SIMO case

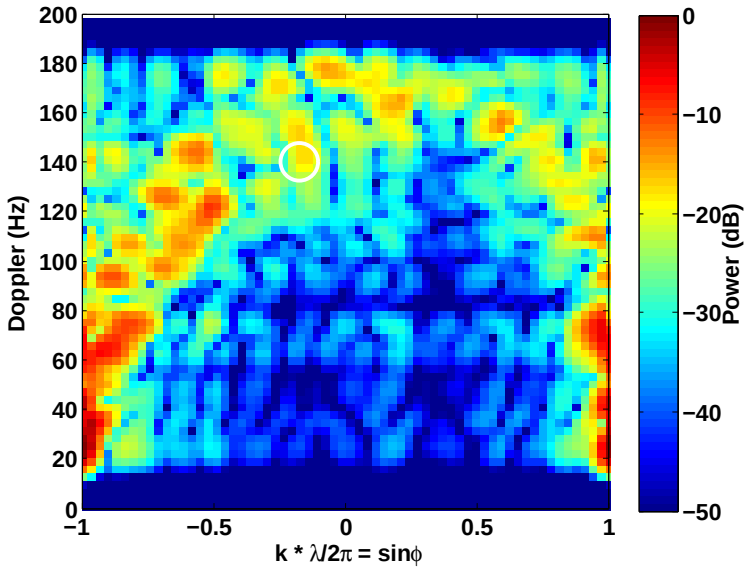

FIGURE 4.9: SIMO Doppler-Azimuth Plot with Estimated Covariance Matrices

had a known covariance matrix.

4.2.4 Output SCNR Loss Compared to the Fully Adaptive Solution

To determine the effect of the rank reduction on the output signal-to-clutter-plus-noise (SCNR), 500 Monte Carlo realizations were performed comparing the SCNR of the fully adaptive solution (i.e. the solution that does not contain a transformation matrix $\mathbf{T}$) to the SCNR of the partially adaptive solution. The known covariance matrices were used, as there would not be enough snapshots available to use the estimated covariance matrix with the fully adaptive solution. The result was an average SCNR loss of 0.51 dB incurred by dropping from the fully adaptive solution to the partially adaptive solution. The SCNR loss is small because the partially adaptive solution is sufficient to null the multipath clutter. Refer back to the beampattern of Fig. 4.2.1 and remember this beampattern was computed with the partially adaptive solution. Compare the partially adaptive beampattern to the bi-directional spatial spectrum of Fig. 4.2.1 and observe that it places deep nulls in the locations of the clutter. Since the partially-adaptive beampattern can adequately suppress the

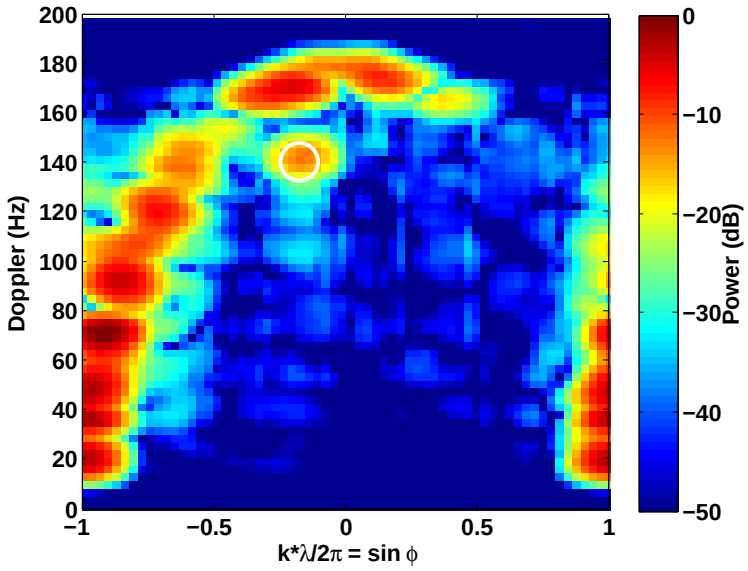

FIGURE 4.10: MIMO Doppler-Azimuth Plot with Estimated Covariance Matrices

clutter, there is not much of advantage of going to the fully adaptive solution.

4.2.5 Monte Carlo Detection Results with Random Target Statistics

To illustrate the more general superiority of MIMO over SIMO, Monte Carlo trials were performed and some of the target statistics were switched from deterministic values to random variables. The range of the target was kept constant at 15 m, but the target azimuth angle was made a uniform random variable ranging from -45 degrees to the azimuth angle with which it would intersect the wall (approximately +15 degrees). The target tangential velocity, *relative to the ground*, was made a uniform random variable from +2 miles per hour to +6 miles per hour (which corresponds to +0.88 m/s to +2.69 m/s). The SNR was unchanged (+10 dB for MIMO and +19 dB for SIMO), and the clutter statistics were unchanged. Fig. 4.13 shows the resulting ROC curves for MIMO and SIMO. For SIMO, the known covariance matrix was used to give it the best chance of working. Observe how MIMO performs drastically superior to MIMO. This results shows that, for a wide variety of target azimuth angles and tangential velocities, MIMO is superior to SIMO.

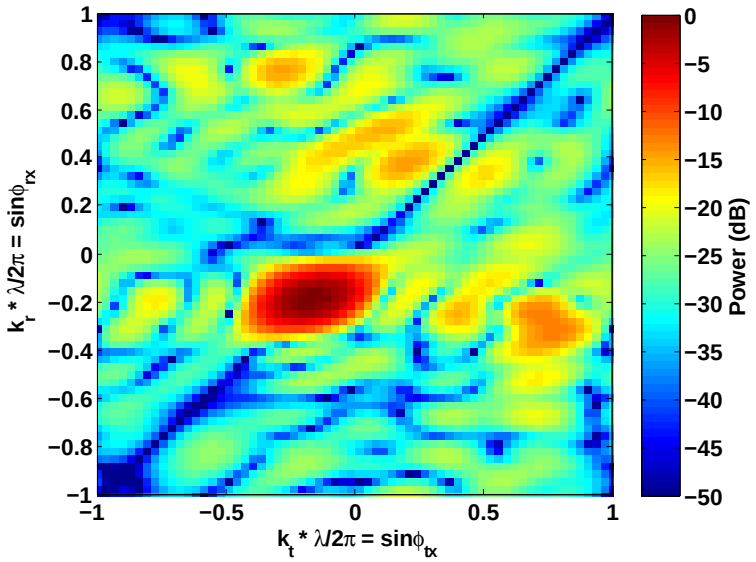

FIGURE 4.11: Bi-directional Beampattern of the Adaptive MIMO Beamformer: Estimated Covariance Matrix

4.3 Summary

Bi-directional adaptive MIMO beamforming has been shown to have the ability to suppress multipath clutter where SIMO beamforming cannot even in non-separable multipath scenarios. MIMO beamformers, unlike SIMO, have the ability to discriminate on both the receive side and the transmit side. With the rank of the MIMO covariance matrix being able to estimated from the method described in Chapter 3, a partially adaptive multipath clutter suppression algorithm was designed, and the number of partially adaptive degrees of freedom was chosen to be at least equal to the rank of the MIMO covariance matrix. Simulation results demonstrated that MIMO beamforming was able to successfully suppress multipath clutter in a non-separable multipath scenario.

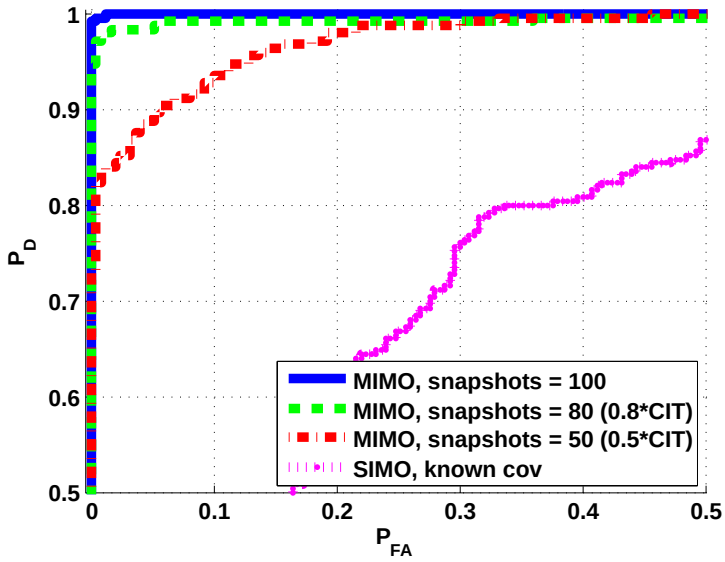

FIGURE 4.12: Receiver Operating Characteristic

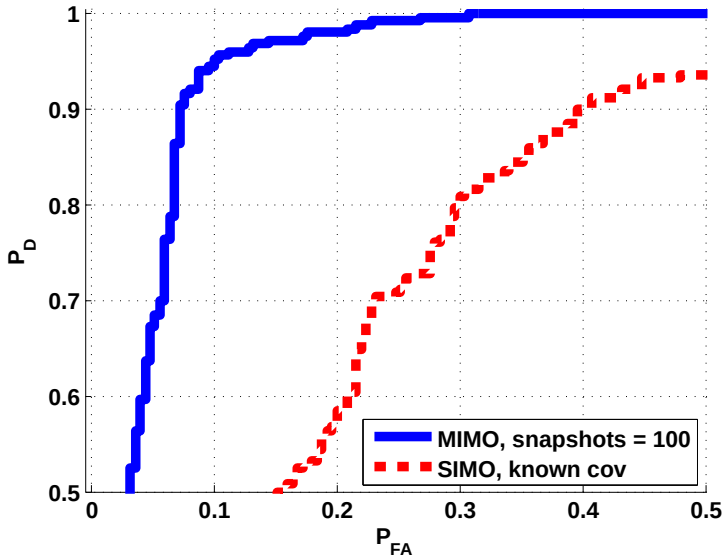

FIGURE 4.13: Receiver Operating Characteristic with Random Target Statistics

5

Clutter-based Adaptive MIMO Phased Array Calibration

Sensor array calibration has been a well-studied problem for several decades, with most papers focusing on estimating the gains, phases, and mutual coupling parameters of receive arrays [69–76]. Typically, the array calibration problem assumes the presence of one or more known or uncertain sources of opportunity and involves a combination of source direction-of-arrival (DoA) and calibration parameter estimation. A variety of sources-of opportunity have been used over the years including interferers [70], meteor-trails, space-based objects, and ground-clutter [71]. Auto-calibration techniques [77, 78] offer an alternative approach for array calibration without the need additional sources-of-opportunity. In essence, auto-calibration or "self calibration" methods seek to jointly estimate both target and array parameters simultaneously. Most approaches for auto-calibration use some sort of sub-space fitting [77] which fits the calibration factors to the dominant components of the measured field. Besides the important question of gain and phase error identifiability [78], most of these approaches do not directly optimize the sidelobe performance of the resulting calibrated array. This is despite the fact that sidelobe degradation due

to miscalibration often impacts detection performance much more than mainlobe mismatch.

MIMO radar non-causal transmit beamforming has been used successfully to calibrate a transmit array with a single receiver and a point source in the far field [19]. The approach proposed here differs from that in [79] in that a point source is not required for far-field calibration, rather, ground clutter is exploited as a source of opportunity. Most calibration methods require the presence one or point sources or point targets in the field. This can be problematic in many scenarios, as point targets of opportunity may not be available, and it can impractical to introduce artificial point sources. Additionally, the effects of miscalibration may vary as a function of look direction. The combination of ground clutter and MIMO radar present an opportunity to solve this problem. In most scenarios, ground clutter appears at all azimuth angles. However, with most radar systems, there is no ability to separate the ground clutter into individual point targets. One application of MIMO radar allows for this: non-causal transmit beamforming. Non-causal transmit beamforming, realized through MIMO radar, allows for one to virtually transmit beamform after signal reception. Steering a transmit beam virtually illuminates one patch of clutter at a time, thus creating a set of "point responses" for the receive array at every look direction, and a set of receiver weights *for each look direction* can be generated that optimizes the sidelobe response.

This chapter proposes to use signal processing of ground backscatter from MIMO radar signals in order to estimate direction-dependent array calibration factors. The key advantage of using MIMO illumination for calibration purposes is that it provides separable direction of arrival and departure information from clutter sources-of-opportunity over a wide set of angles with the ability to simultaneously optimize transmit and receive calibration factors using the same data observation.

5.1 Signal and Calibration Error Model Model

5.1.1 Signal without Calibration Errors

Consider a MIMO radar system with N_r receiver elements and N_t transmitter elements. A plane wave incident on the receiver array can be represented by the wavefront vector $\mathbf{v}_r$:

$$\mathbf{v}_r(\mathbf{k}_r) = \left[e^{j\mathbf{k}_r^T \mathbf{x}_{r1}}, ..., e^{j\mathbf{k}_r^T \mathbf{x}_{rN_r}} \right]^T \tag{5.1}$$

where $\mathbf{x}_{rn}$ is the position of the n^{th} receive element and $\mathbf{k}_r$ is the wavenumber of the incident received wave. Similarly, a plane wave originating from the transmitter array can be represented as the wavefront vector $\mathbf{v}_t$:

$$\mathbf{v}_t(\mathbf{k}_t) = \left[e^{-j\mathbf{k}_t^T \mathbf{x}_{t1}}, ..., e^{-j\mathbf{k}_t^T \mathbf{x}_{tN_t}} \right]^T \tag{5.2}$$

where $\mathbf{x}_{tl}$ is the position of the l^{th} transmit element. A negative sign compensates for the difference between incoming (receive) and outgoing (transmit) angles. In general, the radar return can be represented as a sum of individual wavefront vectors. The components of the return can be characterized as targets, clutter, and noise. In this technique, calibration is performed solely on clutter, and there are no targets. The clutter returns can be divided into types: direct-path clutter and multipath clutter. For direct-path clutter, the direction-of-arrival spatial frequency $\mathbf{k}_r$ of each clutter component equals the direction-of-departure spatial frequency $\mathbf{k}_t$, whereas for multipath clutter the two spatial frequencies are different. This calibration technique will consider the scenario in which only direct-path clutter exists, and there is no significant multipath. The receive data vector of direct-path clutter and noise is:

$$\mathbf{z}_r = \mathbf{z}_{r,c} + \mathbf{z}_{r,n} \tag{5.3}$$

where $\mathbf{z}_{r,c}$ represents the receiver clutter return and $\mathbf{z}_{r,n}$ represents uncorrelated noise. Assume each component is the sum of one or more bi-directional wavefront vectors with zero-mean complex Gaussian amplitudes. The receiver data covariance matrix is shown by:

$$\mathbf{R}_{z,r} = \mathbf{R}_{r,c} + \mathbf{R}_{r,n} \tag{5.4}$$

The receiver clutter covariance matrix can be expressed as:

$$\mathbf{R}_{r,c} = \int_{\mathbf{k}\in\mathbf{K}_c} \sigma_c^2(\mathbf{k})\mathbf{v}_r(\mathbf{k})\mathbf{v}_r^H(\mathbf{k})d\mathbf{k} \tag{5.5}$$

where σ_c^2 represents the RCS of the clutter patch at spatial frequency $\mathbf{k}$ and $\mathbf{K}_c$ is the set containing all spatial frequencies for which clutter exists. The noise is considered to be uncorrelated between all elements, and thus noise covariance matrix is:

$$\mathbf{R}_n = \sigma_n^2\mathbf{I} \tag{5.6}$$

On the transmit array, after separating the transmitter channels (via the waveform orthogonality property), a transmit data vector can be formed:

$$\mathbf{z}_t = \mathbf{z}_{t,c} + \mathbf{z}_{t,n} \tag{5.7}$$

where $\mathbf{z}_{t,c}$ represents the transmitter clutter return and $\mathbf{z}_{t,n}$ represents uncorrelated noise. Likewise, the transmitter data covariance matrix can be broken down into clutter and noise:

$$\mathbf{R}_{z,t} = \mathbf{R}_{t,c} + \mathbf{R}_{t,n} \tag{5.8}$$

Expressions for the transmitter clutter and noise covariance matrices are analogous to (5.5) and (3.11) respectively, with the transmit wavefront vector $\mathbf{v}_t$ of (5.2) replacing

the receive wavefront vectors $\mathbf{v}_r$.

5.1.2 Signal with Calibration Errors

When calibration errors are present, the ideal wavefront vectors are perturbed. Sources of calibration errors can be roughly divided into three categories: gain errors on each element, phase errors on each element, and mutual coupling errors between elements. Gain and phase errors can be represented by a multiplication by a diagonal matrix $\mathbf{G}$:

$$\tilde{\mathbf{v}}_r = \mathbf{G}_r \mathbf{v}_r \tag{5.9}$$

where

$$\mathbf{G}_r = \text{diag}\left[(1+g_{r1})e^{j\phi_{r1}}, (1+g_{r2})e^{j\phi_{r2}}, \ldots, (1+g_{rN_r})e^{j}\phi_{rN_r}\right] \tag{5.10}$$

where g_{rn} is the real gain error on the n^{th} receiver element and ϕ_{rn} is the phase error on the n^{th} receiver element. Mutual coupling can be represented by a multiplication by a non-diagonal matrix $\mathbf{C}_r$:

$$\mathbf{C}_r = \begin{bmatrix} 1 & c_{r1,2} & \cdots & c_{r1,(N_r-1)} \\ c_{r2,1} & 1 & \cdots & c_{r2,(N_r-1)} \\ \vdots & \vdots & \ddots & \vdots \\ c_{r(N_r-1),1} & c_{r(N_r-1)m2} & \cdots & 1 \end{bmatrix} \tag{5.11}$$

where $c_{rn,m}$ is the complex mutual coupling coefficient between the n^{th} and the m^{th} receiver element. As there is no mutual coupling between an element and itself, the diagonal of $\mathbf{C}_r$ is unity. The mutual coupling parameters are dependent of the physical characteristics of the antenna elements, the RF equipment associated with each antenna element, and the environmental scenario and thus is difficult to predict. One proposed model for the mutual coupling matrix subdivides the mutual coupling

matrix into the Hadamard product of four submatrices [76]. In general, it can be said that the magnitude of the mutual coupling between any pair of antenna elements is inversely proportion to the distance between them [80]. Because the mutual coupling matrix is difficult to model, a method that does not assume a mutual coupling model or is robust to the mutual coupling model assumptions is desirable.

$$\tilde{\mathbf{v}}_r = \mathbf{C}_r \mathbf{G}_r \mathbf{v}_r \tag{5.12}$$

Likewise, the same factors affect the transmit array. Transmit gain and phase errors can be gathered into a matrix $\mathbf{G}_t$, similar to (5.10), and transmit mutual coupling can be represented by a matrix, $\mathbf{C}_t$. Then, the perturbed transmit wavefront vector is now:

$$\tilde{\mathbf{v}}_t = \mathbf{C}_t \mathbf{G}_t \mathbf{v}_t \tag{5.13}$$

The receive clutter covariance matrix with the array perturbations is now:

$$\mathbf{R}_{r,c} = \int_{\mathbf{k} \in \mathbf{K}_c} \sigma_c^2(\mathbf{k}) \tilde{\mathbf{v}}_r(\mathbf{k}) \tilde{\mathbf{v}}_r^H(\mathbf{k}) d\mathbf{k} \tag{5.14}$$

and the transmitter clutter covariance matrix is now:

$$\mathbf{R}_{t,c} = \int_{\mathbf{k} \in \mathbf{K}_c} \sigma_c^2(\mathbf{k}) \tilde{\mathbf{v}}_t(\mathbf{k}) \tilde{\mathbf{v}}_t^H(\mathbf{k}) d\mathbf{k} \tag{5.15}$$

5.2 Clutter-based Adaptive MIMO Phased Array Calibration

This section introduces the algorithm for clutter-based adaptive MIMO phased array calibration (CAMPAC). The central concept of CAMPAC is as follows: for each desired steering direction, utilize the transmit beamformer to isolate a patch of clutter. For each direction, there will be a receiver data vector containing one clutter patch.

From these receive data vectors, form a complete set of estimated receive steering vectors. Then, for each receive look direction, design beamforming weights to minimize the power in sidelobe regions, using the estimated receive steering vectors.

5.2.1 Steering Vector Estimation

Define the k^{th} snapshot of the MIMO data matrix, $\mathbf{Z}_k$, as the N_r-by-N_t matrix containing the data from the N_r receiver elements and the N_t transmitter elements. The K data snapshots are taken over range bins. For each look direction $\mathbf{k}_i$, the assumed transmitter steering vector $\mathbf{v}_t(\mathbf{k}_i)$ of (5.2) is used to transmit beamform the data to the desired look direction. Then, the receiver sample covariance matrix for direction $\mathbf{k}_i$ is then:

$$\hat{\mathbf{R}}_z(\mathbf{k}_i) = \frac{1}{K}\sum_{k=1}^{K} \mathbf{Z}_k \mathbf{v}_t^* \mathbf{v}_t^T \mathbf{Z}_k^H \tag{5.16}$$

where $\mathbf{A}^*$ represents the conjugate of $\mathbf{A}$, $\mathbf{A}^T$ represents the non-conjugate transpose of $\mathbf{A}$, and $\mathbf{A}^H$ represents the conjugate transpose (Hermitian transpose) of $\mathbf{A}$.

In theory, the receiver sample covariance matrix $\hat{\mathbf{R}}_z(\mathbf{k}_i)$ of (5.16) should contain one dominant clutter component and uncorrelated noise. However, this condition is only precisely true if the transmit array is identical to the receive array, as $\hat{\mathbf{R}}_z(\mathbf{k}_i)$ is formed from beams of the transmit array. To obtain a steering vector estimate, the projection scaling method proposed by [81] will be utilized, which is summarized here. The sample covariance matrix $\hat{\mathbf{R}}_z(\mathbf{k}_i)$ is broken down into its eigendecomposition:

$$\hat{\mathbf{R}}_z(\mathbf{k}_i) = \mathbf{U}(\mathbf{k}_i)\mathbf{\Lambda}\mathbf{U}^H(\mathbf{k}_i) \tag{5.17}$$

Assuming a relatively high clutter-to-noise ratio (CNR), the clutter eigenvalues can be separated from the noise eigenvalues via thresholding. The eigenvector matrix is divided into the clutter subspace and the noise subspace:

$$\mathbf{U} = [\mathbf{U}_c(\mathbf{k}_i) \quad \mathbf{U}_n] \tag{5.18}$$

The subspace projection matrix corresponding to the clutter patch subspace of $\hat{\mathbf{R}}_z(\mathbf{k}_i)$ is:

$$\mathbf{P}(\mathbf{k}_i) = \mathbf{U}_c(\mathbf{k}_i)\mathbf{U}_c^H(\mathbf{k}_i) \tag{5.19}$$

Finally, the estimated receive steering vector $\hat{\mathbf{v}}_r$ can be formed as the projection of the assumed receive steering of (5.1) onto the clutter patch subspace:

$$\hat{\mathbf{v}}_r(\mathbf{k}_i) = \mathbf{P}(\mathbf{k}_i)\mathbf{v}_r(\mathbf{k}_i) \tag{5.20}$$

A steering vector estimate $\hat{\mathbf{v}}_r(\mathbf{k}_i)$ for every desired look direction is calculated before moving on to the next segment of the algorithm.

5.2.2 Receiver Weight Calculation

With receive steering vector estimates for every look direction calculated, receive beamforming weights for each look direction can be generated. The desired weights will minimize the power in the sidelobe region, while not distorting the look direction. The optimization problem to solve is:

$$\min \mathbf{w}_r^H \mathbf{R}_{SL} \mathbf{w}_r \tag{5.21}$$

with the constraint

$$\left|\mathbf{w}_r^H \hat{\mathbf{v}}_r(\mathbf{k}_i)\right| = 1 \tag{5.22}$$

where $\mathbf{R}_{SL} = \mathbf{A}_{SL}\mathbf{A}_{SL}^H$ and the columns of the matrix $\mathbf{A}_{SL}$ are the estimated steering vectors of (5.20) corresponding to the locations of the sidelobes:

$$\mathbf{A}_{SL} = [\hat{\mathbf{v}}_{sl1}, \hat{\mathbf{v}}_{sl2}, \ldots] \tag{5.23}$$

The solution to this problem is the well known minimum variance distortionless response (MVDR) [82] solution:

$$\mathbf{w}_r = \frac{\mathbf{R}_{SL}^{-1}\hat{\mathbf{v}}_r(\mathbf{k}_i)}{\hat{\mathbf{v}}_r^H(\mathbf{k}_i)\mathbf{R}_{SL}^{-1}\hat{\mathbf{v}}_r(\mathbf{k}_i)} \tag{5.24}$$

The algorithm generates a unique set of beamforming weights for each look direction. Note that the algorithm itself assumes nothing about the miscalibration model. This is desirable, as miscalibration models that include mutual coupling parameters are complex and have a large number of unknowns. The algorithm directly calculates beamforming weights without needing the intermediate step of estimating each miscalibration term.

5.3 Simulation Results

Simulation results were performed to evaluate the performance of CAMPAC. The metric of interest is the maximum sidelobe level, as this will most limit detection performance. To compare performance, a Hamming window applied to the uncalibrated data will be used as the comparison standard. The desired mainlobe width selected for CAMPAC was selected to be twice the mainlobe width of a rectangular window applied to the assumed array manifold vector. This width is approximately equal to the mainlobe width of a Hamming window. The miscalibration model described in Section 5.1.2 will be used to generate the array perturbations. The gain errors, g_{rn} of (5.10) were chosen to be real uniform random variables on the interval $\left[\frac{\sqrt{2}}{2} - 1, \sqrt{2} - 1\right]$, such that the power gain of each element will range uniformly from -3 dB to +3 dB. The phase errors ϕ_{rn} of (5.10) were chosen to be real uniform random variables on the interval $\left[-\frac{\pi}{10}, \frac{\pi}{10}\right]$. The mutual coupling coefficients $c_{rn,m}$ of (5.11) were chosen to be complex zero-mean Gaussian random variables with vari-

ance $\sigma^2 = \frac{1}{100}\left(\frac{\lambda}{2}\right)^2 \frac{1}{L_{m,n}^2}$ where $L_{m,n}$ is the distance between the two elements. With this choice of variance, elements that have an inter-element spacing of $L_{m,n} = \frac{\lambda}{2}$ will have an expected mutual coupling magnitude of -20 dB, and the magnitude of the mutual coupling is inversely proportional to the inter-element spacing. Clutter is assumed to exist at all angles, with a random complex zero-mean Gaussian amplitude. The specific clutter-to-noise ratio (CNR) will be given for each test case.

Several test scenarios were selected to test the robustness of the algorithm. These were:

1. $N_r = N_t$, $dr = dt = \frac{\lambda}{2}$
2. $N_r = 2N_t$, $dr = dt = \frac{\lambda}{2}$
3. $N_r = 2N_t$, $dr = \frac{\lambda}{2}$, $dt = \lambda$
4. $N_r = N_t$, $dr = dt = \frac{\lambda}{2}$, transmit miscalibration added
5. $N_r = 2N_t$, $dr = dt = \frac{\lambda}{2}$, transmit miscalibration added

For each case, after the receiver weights are generated, the weights were applied to a point target with a normalized spatial frequency $k_x \frac{\lambda}{2\pi} = 0.25$. The point target suffers from the array perturbation. Monte Carlo simulations as a function of number of snapshots and clutter-to-noise ratio (CNR) were performed. For every case performed here, the number of receivers $N_r = 16$.

5.3.1 Case 1 : Equal number of transmitters and receivers

In this case, both arrays have the same number of elements and both arrays are nominally spaced at the Nyquist interval. An example realization of the point target response with 100 snapshots and a CNR of 30 dB is shown in Fig. 5.1. Observe that the sidelobes produced by the CAMPAC weights are significantly lower than

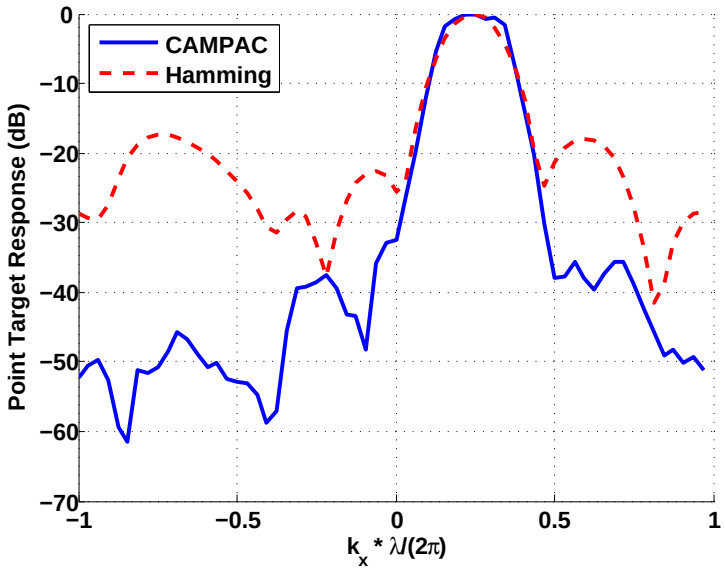

FIGURE 5.1: Case 1: Point Target Response

those produced for the Hamming window. Next, 100 Monte Carlo realizations were run with a CNR of 30 dB and the number of snapshots ranging from 10 to 300. For every Monte Carlo run, a new realization of both the random clutter amplitudes and the random miscalibration parameters were generated. Fig. 5.2 plots the maximum sidelobe level as a function of number of snapshots. The blue curves represent CAMPAC and the red curves represent the Hamming window. The solid lines with the circle markers are the mean value over the realizations, and the dotted lines with the triangle markers represent the 25% and the 75% percentiles of the Monte Carlo trials. Observe that CAMPAC rapidly improves with the number of snapshots, and even with a low number of snapshots, is significantly superior to the Hamming window.

Next, 100 Monte Carlo realizations were run with 100 snapshots and the CNR was varied from 30 dB to 0 dB. Fig. 5.3 plots the maximum sidelobe level as a function of snapshots. Again, the blue curves represent CAMPAC and the red curves represent the Hamming window, and the dotted lines are the the 25% and the 75% percentiles. Observe that initially CAMPAC performance increases as a function of CNR up until about 10 dB, and then begins to level off. Also note that the Hamming window

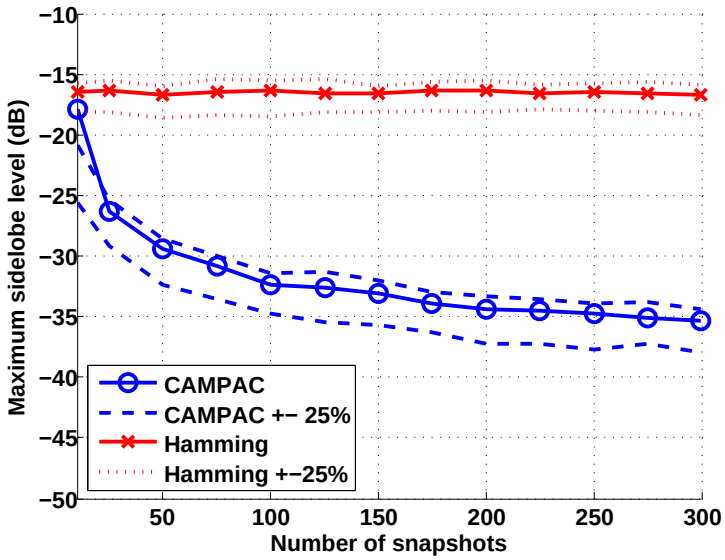

FIGURE 5.2: Case 1: Monte Carlo results for maximum sidelobe level as function of number of snapshots

performance is unchanged as the CNR increases, confirming that the problem with the Hamming window is not the noise but the miscalibration.

5.3.2 Case 2: Twice as many receivers as transmitters

In this case, the transmit array has half as many elements as the receive array, and both arrays are nominally spaced at the Nyquist interval. An example realization of the point target with 100 snapshots and a CNR of 30 dB is shown in Fig. 5.4. Observe that the sidelobes produced by the CAMPAC weights are significantly lower than those produced by the Hamming window. 100 Monte Carlo realizations were run with a CNR of 30 dB and the number of snapshots varying. The result is shown in Fig. 5.5. Then another set of 100 Monte Carlo realizations were run with 100 snapshots and the CNR varying. The result is shown in Fig. 5.6. Observe that, even with the number of transmitter elements half of the number of receiver elements, CAMPAC is significantly superior to the Hamming window, although not quite as good as CAMPAC in case 1. CAMPAC will eventually fail if the ratio of $\frac{N_r}{N_t}$ gets

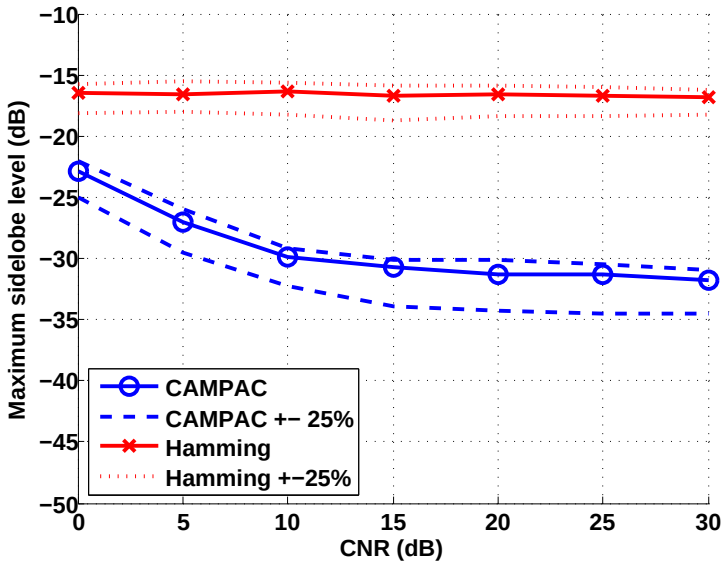

FIGURE 5.3: Case 1: Monte Carlo results for maximum sidelobe level as function CNR

too high. As a thought exercise, consider the case where $N_t = 1$. In this extreme case, the transmitter has no ability to discriminate and there is no ability to split the clutter into discrete patches. However, the result for this case shows CAMPAC is robust to less extreme differentials.

5.3.3 Case 3: Twice as many receivers as transmitters, and transmit array is undersampled

In this case, the transmit array has half as many elements as the receive array, but the transmit array elements are spaced at λ intervals whereas the receiver array elements are spaced at $\frac{\lambda}{2}$ intervals. This case would be one where CAMPAC would not be predicted to have difficulties. Remember, CAMPAC utilizes the transmit beamformer to isolate clutter patches, which are then used to estimate steering vectors. However, the transmit array is undersampled and thus its array pattern will have grating lobes. Thus, each clutter patch will also contain the return from a second, aliased clutter patch. An example realization is shown in Fig. 5.7. Observe the elevated sidelobes, especially around the region of $k_x \frac{\lambda}{2\pi} = -0.75$, which is the

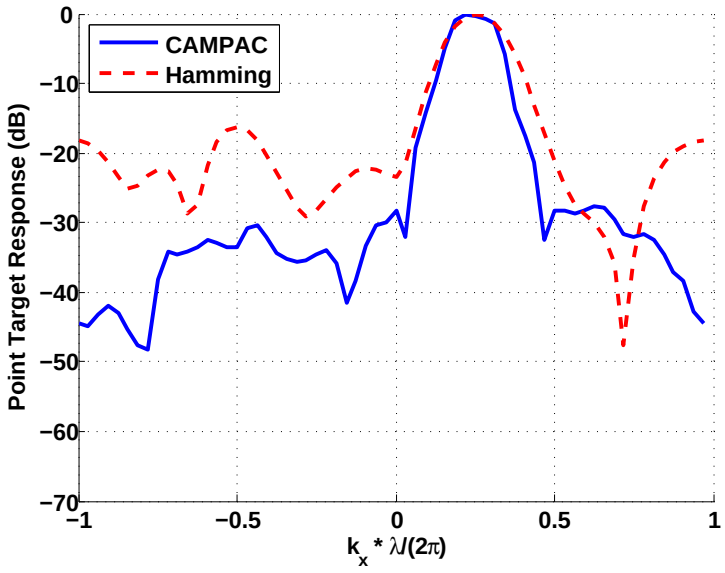

FIGURE 5.4: Case 2: Point Target Response

location of the transmitter grating lobe. 100 Monte Carlo realizations of this case were run with a CNR of 30 dB and the number of snapshots varying. The result is shown in Fig. 5.8. Then another set of 100 Monte Carlo realizations were run with 100 snapshots and the CNR varying. The result is shown in Fig. 5.9. Observe the elevated sidelobe levels compared to cases 1 and case 2. However, also observe that with sufficient snapshots, CAMPAC is superior to the Hamming window, but not my as much as in the previous cases.

5.3.4 Case 4: Equal number of transmitters and receivers, and transmit array miscalibration added

Case 4 is identical to case 1 such that both arrays have the same number of elements and Nyquist spacing. However, in this case, array perturbation was added to both the transmit and receive arrays. The same model described in Section 5.1.2 was used to generate transmit array perturbation, and the miscalibration parameters were chosen to be random variables with the same statistics as the receiver miscalibration random variables . (Refer to the beginning of section for the miscalibration statistics). No

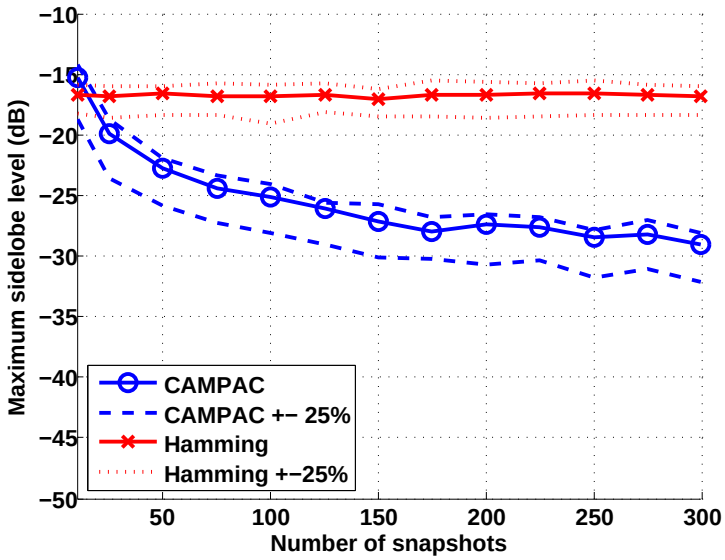

FIGURE 5.5: Case 2: Monte Carlo results for maximum sidelobe level as function of number of snapshots

attempt is made to correct for the transmit calibration errors. The purpose of this case is to prove CAMSAP is robust to errors in the transmit calibration. In many scenarios, a user will have the ability to provide their own beamformer weights to the received data but will have no ability to modify the transmitter. This case represents that scenario. An example realization is shown in Fig. 5.10. Observe that CAMPAC is still able to achieve much better sidelobes than the Hamming window. 100 Monte Carlo realizations of this case were run with a CNR of 30 dB and the number of snapshots varying. The result is shown in Fig. 5.11. Then another set of 100 Monte Carlo realizations were run with 100 snapshots and the CNR varying. The result is shown in Fig. 5.12. Again, observe that CAMPAC is robust to transmit miscalibration errors.

5.3.5 Case 5: Twice as many receivers as transmitters, and transmit array miscalibration added

Case 5 is a repeat of case 2, but with transmit miscalibration added. An example realization of the point target with 100 snapshots and a CNR of 30 dB is shown in

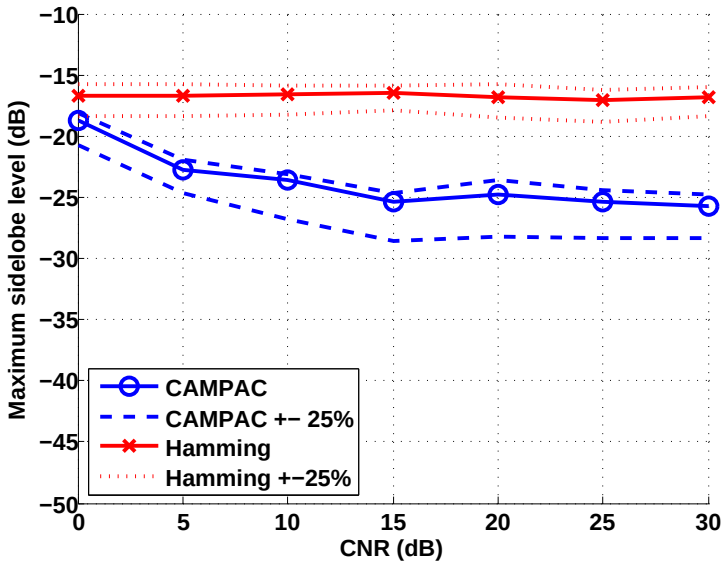

FIGURE 5.6: Case 2: Monte Carlo results for maximum sidelobe level as function CNR

Fig. 5.13. 100 Monte Carlo realizations were run with a CNR of 30 dB and the number of snapshots varying. The result is shown in Fig. 5.14. Then another set of 100 Monte Carlo realizations were run with 100 snapshots and the CNR varying. The result is shown in Fig. 5.15. Observe that, even with transmit miscalibration and half the number of transmitters as receivers, with sufficient snapshots CAMPAC offers superior performance to the Hamming window.

5.4 Summary

Array perturbation and calibration errors significantly increase the sidelobe level of phased arrays. This paper has shown, that by utilizing a MIMO radar system, beamforming weights can be generated which drastically reduce the sidelobe level. The key feature of the technique, as described here, is that relies on stationary ground clutter alone, and there is no requirement for point sources of point targets in the field. This chapter has shown the proposed technique, CAMPAC, can handle situations in which there are fewer transmitter than receivers and when the transmit

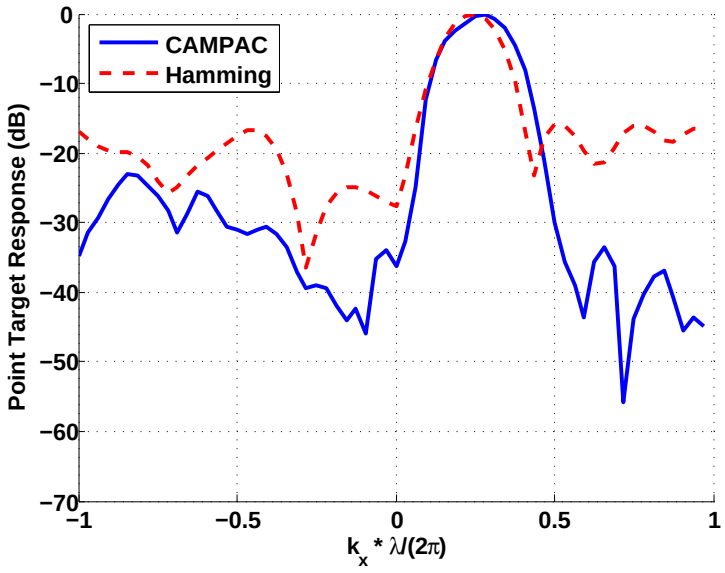

FIGURE 5.7: Case 3: Point Target Response

array itself has calibration errors.

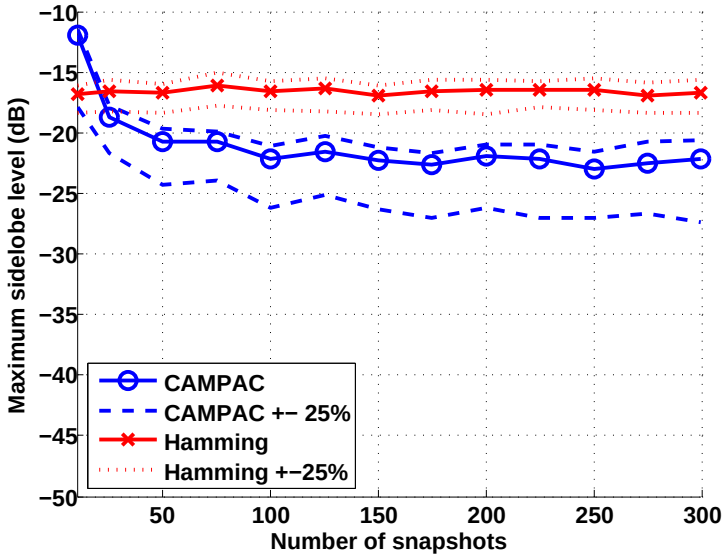

FIGURE 5.8: Case 3: Monte Carlo results for maximum sidelobe level as function of number of snapshots

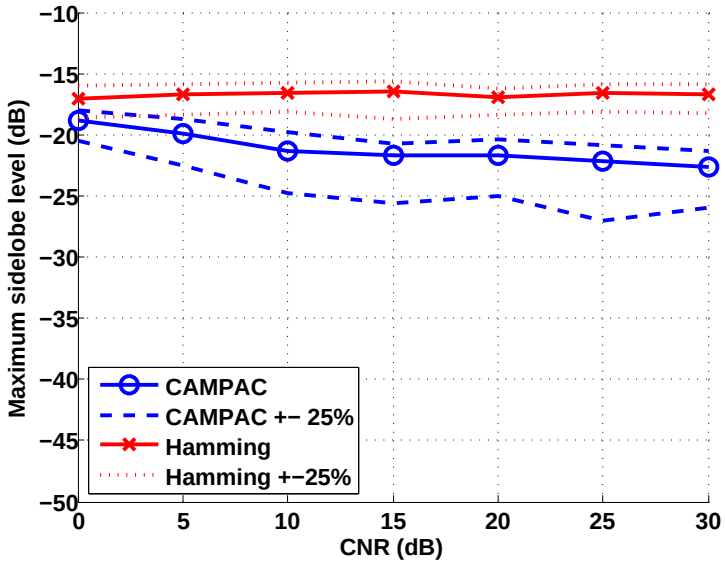

FIGURE 5.9: Case 3: Monte Carlo results for maximum sidelobe level as function CNR

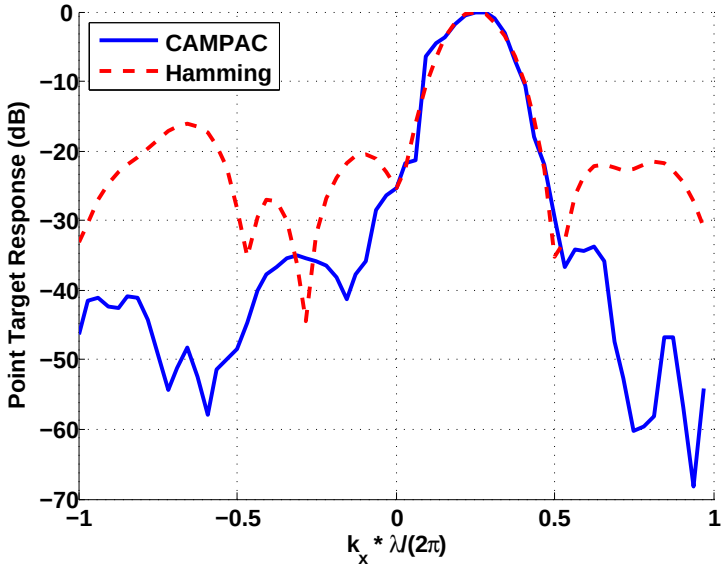

FIGURE 5.10: Case 4: Point Target Response

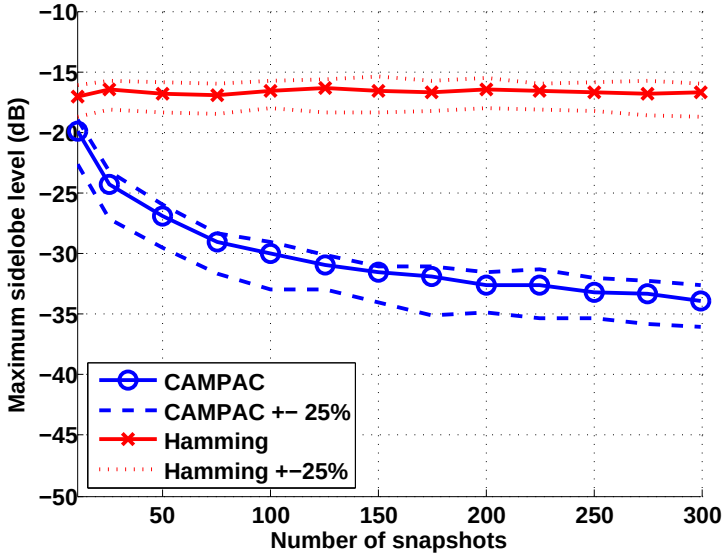

FIGURE 5.11: Case 4: Monte Carlo results for maximum sidelobe level as function of number of snapshots

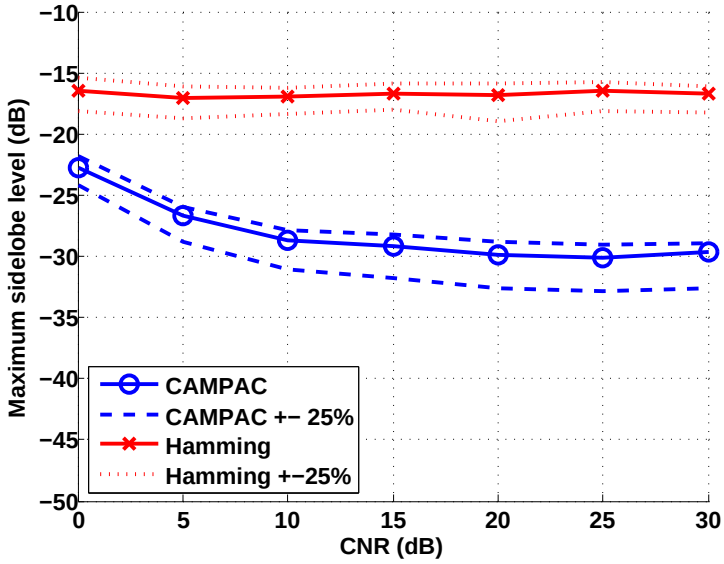

FIGURE 5.12: Case 4: Monte Carlo results for maximum sidelobe level as function CNR

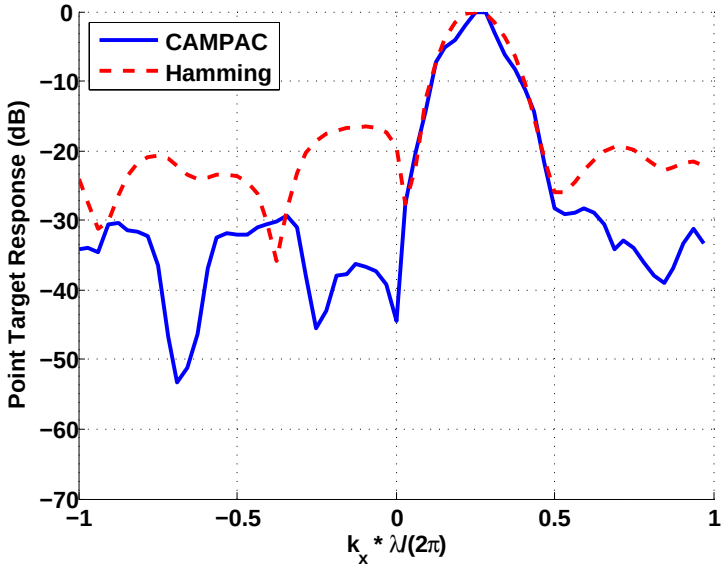

FIGURE 5.13: Case 5: Point Target Response

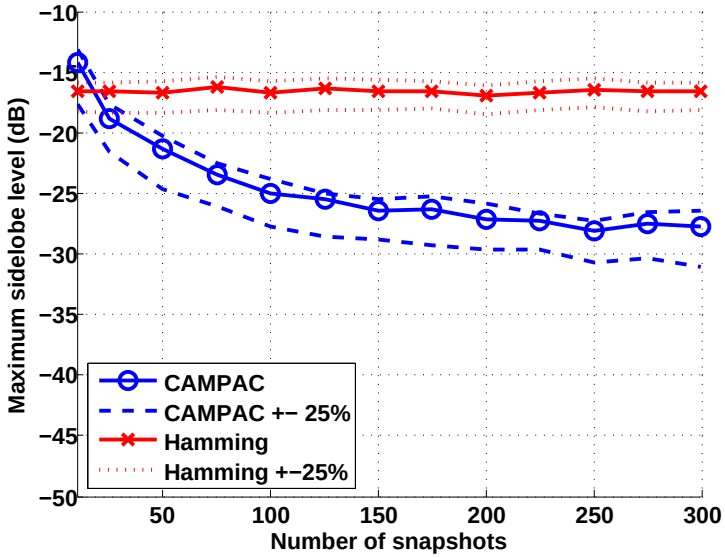

FIGURE 5.14: Case 5: Monte Carlo results for maximum sidelobe level as function of number of snapshots

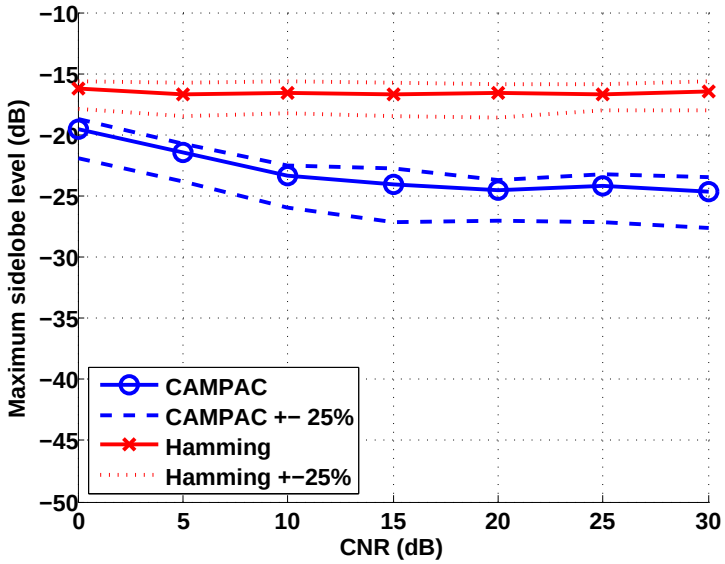

FIGURE 5.15: Case 5: Monte Carlo results for maximum sidelobe level as function CNR

6

The STRADAR MIMO Radar Testbed

To support MIMO radar research, an experimental low-power S-band MIMO radar was developed. The testbed was designed and fabricated by the author with a partnership with the STRAD Corporation in Chapel Hill, North Carolina. Additionally, professors Jeffrey Krolik and Matthew Reynolds at Duke University provided extensive consulting. The STRADAR testbed operates at frequency range of 2.1 GHz to 2.7 GHz and a power level of 25 mW. It has 16 coherent receiver channels. The receiver implements a technique called "stretch processing" (described in detail later in this chapter) in analog circuitry to drastically reduce the baseband bandwidth, and therefore the required baseband sampling frequency. On transmit, it has the ability to operate in either SIMO mode or MIMO mode. In MIMO mode, up to 4 coherent MIMO channels can be utilized. The testbed implements MIMO waveforms via the double-sideband and/or quadrature slow-time MIMO waveforms (explained later in this chapter), a variation of the SLO-MO waveforms described in Chapter 2. The STRADAR can be operated directly from MATLAB via the Data Acquisition Toolbox. The entire system is contained in portable, robust, attractive rectangular package with dimensions of 15.0 inches by 8.5 inches by 4.5 inches. A photo of the

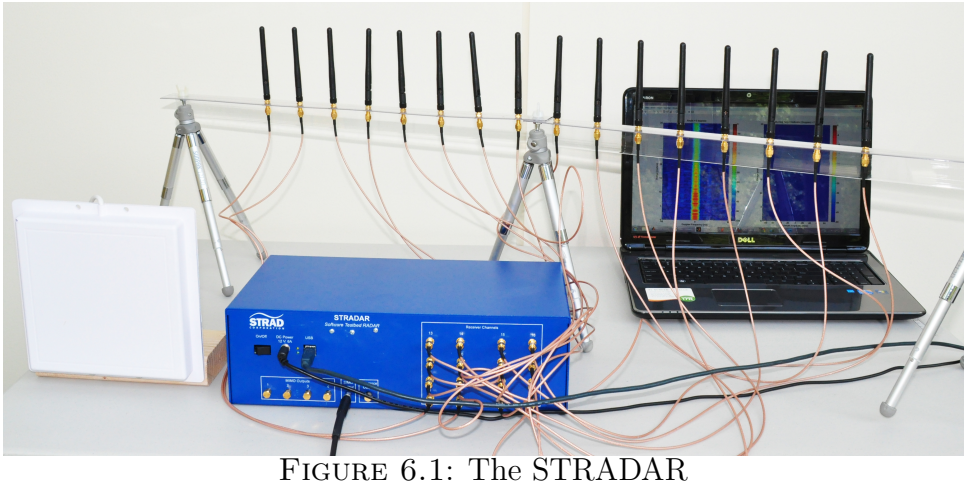

FIGURE 6.1: The STRADAR

STRADAR is shown in Fig. 6.1.

The author completed the following tasks in the development of the STRADAR.

- Design of a custom printed circuit board (PCBs) containing multiple RF receiver front-ends. The components populating the board were commercial-off-the-shelf (COTS), but the board itself was custom designed and fabricated.

- Design of a custom printed circuit board containing both the SIMO and MIMO RF transmitter front-ends. Again, the components were COTS, but the PCB design was custom.

- Design of a custom distribution/master printed circuit board that interfaced the transmitter front-end board and multiple receiver front-end boards with a National Instruments Data Acquisition (DAQ) board and power supplies

- Design of a custom, robust, portable enclosure to house all of the custom printed circuit boards listed above and a National Instruments Data Acquisition (DAQ) board

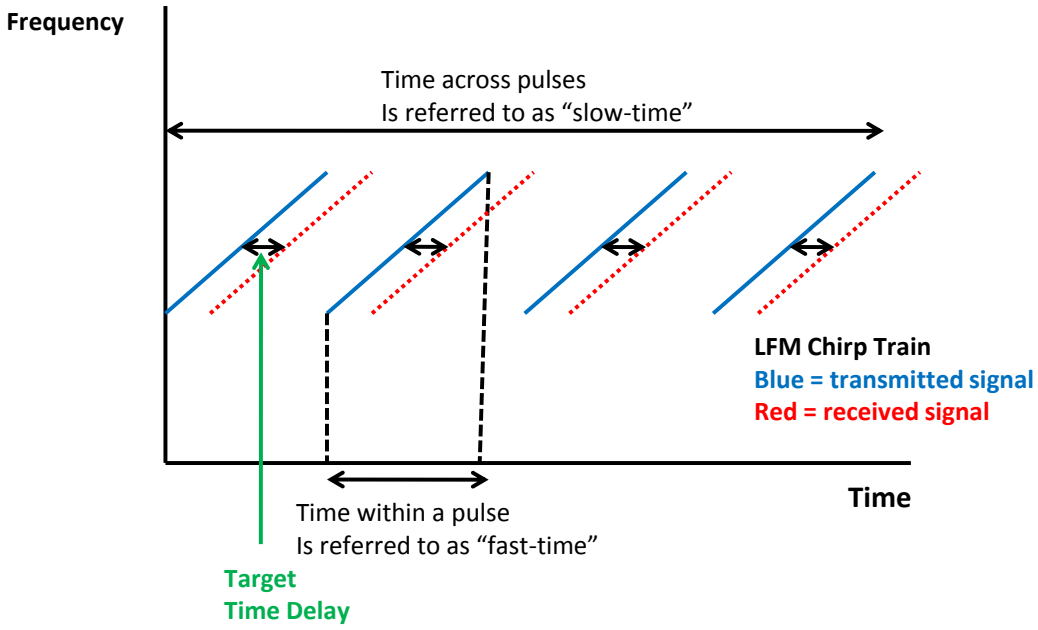

FIGURE 6.2: LFM Waveform in the Time-Frequency Domain

6.1 Stretch Processing with LFM chirps

Consider a radar system which transmits a train of LFM waveforms, as described in Chapter 2 in (2.2). Fig. 2.1 is re-displayed here as Fig. 6.2 for the reader's convenience. The optimal technique for processing the returns would be the matched filter, as in (2.4). However, implementing the matched filter directly in digital signal processing requires sampling at a rate greater than twice the bandwidth of the LFM chirp. The STRADAR transmits LFM chirps with a bandwidth of 600 MHz, and therefore would require sampling rates greater than 1.2 GHz to directly implement a matched filter.

A well known alternative technique [2] for processing LFM chirps is known as “stretch processing” or ”de-chirping”. Stretch processing multiplies the received signal by a copy of the transmitted signal. The received signal is offset in time from the time signal, as illustrated in Fig. 6.2. Because the LFM chirp has a constant slope in the time-frequency domain, a fixed time offsets corresponds to a

fixed frequency offset. Multiplying the a LFM chirp with a time-shifted version of the same chirp produces a single-tone sinusoid, and the frequency of this sinusoid is the "beat frequency" or "difference frequency". Fourier analysis can determine the "beat frequency", which is proportional to the time offset. Previously mentioned in Chapter 2, an LFM waveform takes the form:

$$x_p(t) = e^{j2\pi(f_c - \frac{B}{2})t + j\pi\frac{B}{T_0}t^2} \qquad 0 \leqslant t < T_0 \tag{6.1}$$

where f_c is the RF center frequency (Hz), B is the RF swept bandwidth (units of Hz), T_0 is the time duration of one chirp (units of s), and t is the time variable (units of s). An LFM chirp train takes the form:

$$x(t) = \sum_{m=0}^{M-1} x_p(t - mT_p) \tag{6.2}$$

where T_p is referred to as the waveform repetition interval (WRI, units of s). The ratio of $\frac{T_0}{T_p}$ is referred to as the duty cycle and often expressed as a percentage. In continuous wave (CW) systems the duty cycle is 100%, and thus $T_0 = T_P$. The quantity $\frac{1}{WRI}$ is referred to as the waveform repetition frequency (WRF, units of Hz). The quantity MT_p is referred to as the coherent processing interval (CPI, units of s) or the coherent integration time (CTI, units of s).

The received return can be modeled as the sum of many point scatterers. The return from each point scatterer is the transmitted waveform delayed and Doppler-shifted. The time delay is proportional to the slant range of the point scatterer. If the waveform is sufficiently narrowband ($B \ll f_c$), and the maximum scatterer velocity is much less than the speed of light, the Doppler shift can be modeled as a frequency modulation that is proportional to the scatterer's tangential velocity. The radar received signal is:

$$y(t) = \sum_i \alpha_i x(t - \tau_i) e^{j2\pi F_{Di} t} \tag{6.3}$$

where α_i is a complex amplitude coefficient that is proportional to the radar cross-section (RCS) of the i^{th} point scatterer, τ_i is the time delay of the return from the i^{th} point scatterer, and F_{Di} is the Doppler shift associated with i^{th} point scatterer. The range of the i^{th} scatterer is proportional to its time delay: $r_i = \frac{c\tau_i}{2}$, where c is the speed of light.

Now, instead of matched filtering (6.3) against (6.2), the received signal $y(t)$ of (6.3) will be multiplied by the conjugate $x^*(t)$, of the transmitted signal $x(t)$ of (6.2). The multiply operation is one that can be easily implemented in analog hardware. Now, neglecting edge effects, one "de-chirped" or "de-ramped" waveform takes the form:

$$\begin{aligned} z_p(t) = &\sum_i \alpha_i e^{-j2\pi f_c \tau_i + j2\pi\tau_i \frac{B}{2} + j\pi \frac{B}{T_0} \tau_i^2} e^{-j2\pi \frac{B}{T_0} \tau_i t} e^{j2\pi F_{Di} t} \\ &\sum_i \gamma_i e^{-j2\pi \frac{B}{T_0} \tau_i t} e^{j2\pi F_{Di} t} \qquad 0 \leqslant t \leqslant T_0 \end{aligned} \tag{6.4}$$

where the terms that are not a function of time are gathered into the complex coefficient γ. In most radar systems, it can be assumed that the Doppler shift values are much lower relative to $\frac{1}{\tau}$, and that within one pulse, i.e. within "fast-time", the term $e^{j2\pi F_{Di} t}$ is roughly constant. However, the Doppler modulation will be noticeable across pulses, i.e. across "slow-time". With this assumption, the dechirped LFM chirp train can be written as:

$$\begin{aligned} z_{p,i}(t) &= \gamma_i e^{-j2\pi \frac{B}{T_0} \tau_i t} \qquad 0 \leqslant t \leqslant T_0 \\ z(t) &= \sum_i \sum_{m=0}^{M-1} z_{p,i}(t - mT_p) e^{j2\pi F_{Di} m T_p} \end{aligned} \tag{6.5}$$

The expression of (6.5) is now a function of two time-scales, t and m, representing fast-time and slow-time, respectively. Notice each point target is a sinusoid with frequency of $f_b = -\frac{B}{T_0}\tau_i$. This is the "beat frequency" that is proportional to time delay. Given that range relates to time delay as $r = \frac{c\tau}{2}$, range as function of "beat frequency" can be expressed as:

$$r_i = -\frac{cT_0}{2B} f_b = -\frac{c}{2Bf_{WRF}} f_b \tag{6.6}$$

6.1.1 Effect of baseband sampling frequency on maximum range

It was noted in Chapter 2 that the maximum unambiguous range for an LFM waveform train was $r_{max} = \frac{cT_0}{2} = \frac{c}{2f_{WRF}}$. This maximum range constraint refers to returns from the first pulse arriving after the second (or greater) pulse was transmitted. When stretch processing is employed with an analog-to-digital (A-to-D) converter sampling the baseband signal, another constraint on maximum range occurs from the baseband sampling frequency. Recall stretch processing transforms range into beat frequency. The maximum unaliased beat frequency that can be observed is $\frac{f_s}{2}$, where f_s is the baseband sampling frequency. Therefore, in a stretch system, the maximum unambiguous range is:

$$r_{max} = \min(\frac{cT_0}{2}, \frac{cT_0 f_s}{4B}) = \min(\frac{c}{2f_{WRF}}, \frac{cf_s}{4Bf_{WRF}}) \tag{6.7}$$

This fact must be kept in mind when choosing radar parameters such as the RF bandwidth B and the waveform repetition frequency f_{WRF}.

6.2 The Receiver

Figure 6.3 provides a block diagram of one channel of the receiver-side of the system. The RF signal enters from an external antenna through an SMA port. The signal is

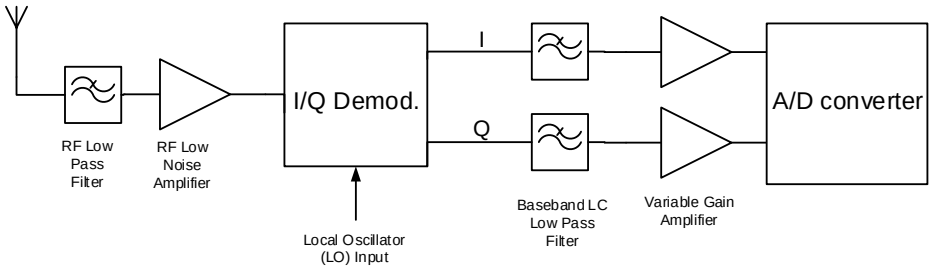

FIGURE 6.3: Block diagram of one of the receiver channels

passed through a passive low-pass filter with a cutoff frequency and then through a low-noise amplifier. After being amplified, the signal is demodulated, and the local oscillator port of the demodulator is fed with a copy of the transmitted signal to implement stretch processing. After de-chirping, the signal is low-passed filtered for anti-aliasing purposes, and then is amplified at baseband, before being fed to an analog-to-digital converter channel.

6.2.1 Receiver metrics

Several metrics were calculated to quantify receive board performance. They are:

- The **gain** of the receiver measures the ratio of the output signal power to the input signal power
- The **noise figure (NF)** defines the amount of noise the receiver circuitry adds. It is defined as the ratio of input signal-to-noise ratio (SNR) to output signal-to-noise ratio (SNR)
- The **input 1 dB compression point (input P1dB)** defines the the maximum power level of an input signal that will not saturate the receiver. It is defined as the input power level that produces an output power level 1 dB below the output of an ideal perfectly linear system.

These receiver metrics are shown in Table 6.1.

Table 6.1: Receiver metrics

Gain	+29 dB
Noise figure	+13.5 dB
Input P1dB	-25 dBm

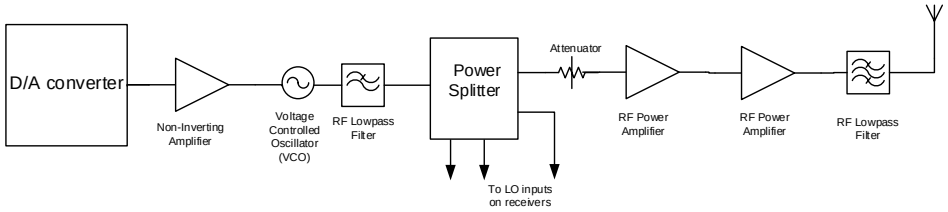

FIGURE 6.4: Block diagram of the transmitter

6.3 The Transmitter

Figure 6.4 provides a block diagram of the SIMO transmitter. The output of a digital-to-analog converter is scaled and then fed into a voltage controlled oscillator (VCO). Sending a ramp function to the input of the VCO results in a LFM waveform on the output. The output of the VCO is filtered to remove harmonics, and then is split. One of the branches is significantly amplified and then fed to the transmit antenna. The other branches are fed to the receiver channels to use for demodulation.

6.4 Double-sideband and Quadrature SLO-MO MIMO Waveforms

One issue with implementing MIMO radar is the waveform selection and generation. In theory, the minimal requirement for MIMO waveforms is that they are orthogonal to each other. However, in practice, it may be difficult or impossible to generate a desired set of waveforms in hardware. Additionally, the receiver must be set up to handle demodulation and pulse compression of the MIMO waveforms. There may also be VSWR problems on the transmitter with certain sets of waveforms. The slow-time MIMO (SLO-MO) waveforms described in Chapter 2 require no changes

on receiver hardware, as the different MIMO channels appear on traditional receivers as Doppler-shifted. Generating the SLO-MO waveforms, however, typically requires a multichannel arbitrary waveform generator, variable RF phase shifters, or using multiple carrier frequencies. This section describes a novel method of generating SLO-MO MIMO waveforms which requires only the addition of a power splitter and passive frequency mixers to existing radar transmit architectures. Passive frequency mixers are inexpensive and have been used for decades in communications applications. Additionally, a baseband sinusoid generator (with a frequency range only up to half the waveform repetition frequency) is needed to generate the mixing frequencies, but this is inexpensive and easily available. It is also possible to use the same mixing frequency on two different MIMO channels, if the sinusoids are 90 degrees out of phase, which allows for twice the number of channels in the same Doppler space. These methods have been tested in simulation and on the STRADAR testbed, and have shown to be successful in generating SLO-MO MIMO waveforms. The waveforms described here are the ones implemented on the STRADAR, using digital-to-analog converter channels as the baseband sinusoid generator.

Consider the LFM chirp train of (6.2), and its return (6.3). To achieve a MIMO radar system, a second transmit channel is added where the original transmitted waveform is mixed with a low-frequency cosine wave immediately before transmission. This waveform will be referred to as $x_c(t)$. Thus, $x_c(t) = x(t)cos(2\pi f_M t)$ where f_M is the frequency of the mixed cosine wave. A passive mixer will perform double-sideband modulation, so the multiplicative factor is a real cosine wave instead of a complex exponential. Define the return from this transmit channel as $y_c(t)$:

$$y_c(t) = \sum_{i=1}^{N} A_{ci} x(t - \tau_i) e^{j2\pi f_{Dci} t} \cos\left(2\pi f_M (t - \tau_{ci})\right) \tag{6.8}$$

Additionally, a third transmit channel can be added where the original transmit-

ted waveform is mixed with a low-frequency sine wave (as opposed to a cosine wave) immediately before transmission. This waveform will be referred to as $x_s(t)$, and $x_s(t) = x(t)\sin(2\pi f_M t)$. Define the return from this transmit channel as $y_s(t)$:

$$y_s(t) = \sum_{i=1}^{N} A_{si} x(t-\tau_i) e^{j2\pi f_{Dsi} t} \sin\left(2\pi f_M (t-\tau_{si})\right) \tag{6.9}$$

Other MIMO channels can be added by adding additional mixing frequencies. Each mixing frequency must be less than half of the radar's waveform repetition frequency ($f_M < \frac{1}{2T_0}$) to avoid slow-time aliasing. Additionally, the spacing between mixing frequencies must be greater than twice the greatest target Doppler shift that is expected to be observed. Otherwise high-Doppler targets from one MIMO channel will appear in another MIMO channel at a lower Doppler. For each mixing frequency added, two additional MIMO channels can be added, as both the cosine and the sine (in-phase and quadrature) of each mixing frequency can be used as a channel. To simplify the separation process on the receiver, it is recommended (but not required) to use mixing frequencies that are multiples of each other (f_M,$2f_M$,$3f_M$,...).

The radar return at the receiver will be the sum of all the radar returns from each of the transmitters, shown in (6.10). The channels can be separated by quadrature demodulation in slow-time.

$$y_{total}(t) = y(t) + y_c(t) + y_s(t) \tag{6.10}$$

It is not necessary to use both the in-phase and quadrature portions of mixing frequency. Performing this implementation of MIMO with a set of waveforms in which only the in-phase portion is used will henceforth be referred to as "DSB SLO-MO", since the waveforms are similar to DSB-AM waveforms. Using a set of waveforms in which both the in-phase and quadratures are used will henceforth be

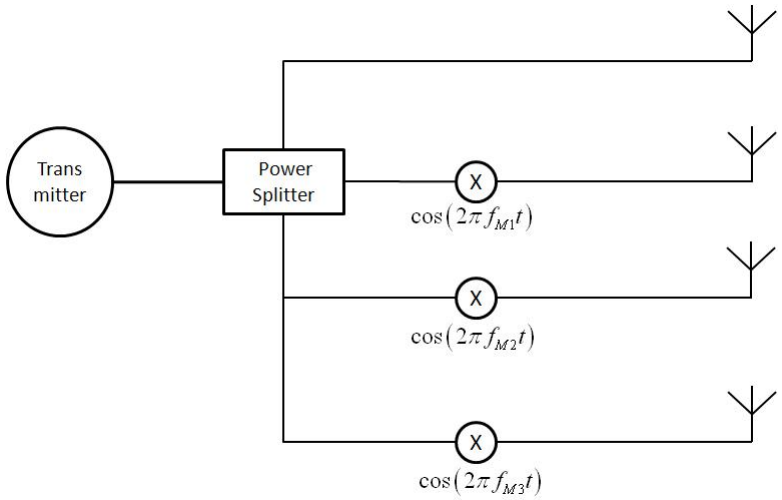

FIGURE 6.5: Block Diagram of DSB Slow-Time MIMO Setup

referred to as "Quadrature SLO-MO", since it uses quadrature multiplexing. DSB SLO-MO "wastes" Doppler space compared to traditional SLO-MO because every channel is split between a positive and negative Doppler component. To achieve the maximum clear range-Doppler area [12],[13], "Quadrature SLO-MO" must be used and every modulating frequency must be used twice (one on the in-phase and once on the quadrature).

Figure 6.5 shows a block diagram for a potential setup of DSB SLO-MO. Figure 6.6 shows a block diagram for a potential setup of Quadrature SLO-MO.

6.4.1 Recovering the MIMO channels at the receiver

The receiver receives the sum of the returns from all of the MIMO channels. To perform virtual transmit beamforming, the channels must be separated from each other. Assume the radar return described in (6.10). It is expanded in (6.11).

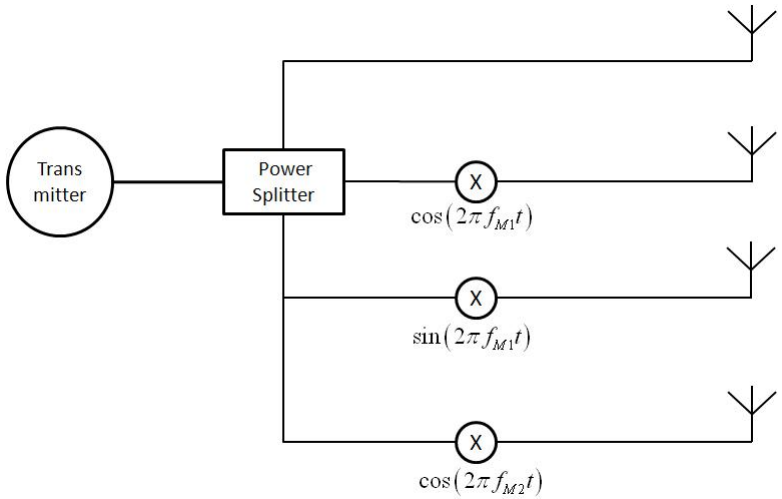

FIGURE 6.6: Block Diagram of Quadrature Slow-Time MIMO Setup

$$\begin{aligned} s_{total}(t) = &\sum_{i=1}^{N} A_i r_i(t) e^{j2\pi f_{Di} t} \\ &+ \sum_{i=1}^{N} A_{ci} r_{ci}(t) e^{j2\pi f_{Dci} t} \cos(2\pi f_M t) \\ &+ \sum_{i=1}^{N} A_{si} r_{si}(t) e^{j2\pi f_{Dsi} t} \sin(2\pi f_M t) \end{aligned} \tag{6.11}$$

There are 3 MIMO channels in this return. To separate, the combined return must be modulated and filtered. A slow-time low-pass filter with a cutoff frequency of $\frac{f_M}{2}$ is needed. The particular design of the filter does not matter much, but is it beneficial to choose a zero-phase filter or to employ forward-backward filtering to avoid corrupting phase information which may need to be preserved for other applications.

First and foremost, the slow-time aspect of the receiver return and the fast-time aspect of the receiver return must be separated and made independent. Typically, this is done by forming a data square (or cube, in the case of multiple receive channels) of fast-time versus slow-time. Otherwise, the slow-time low-pass filter will

destroy all of the fast-time (range) information. In the derivation below, it will be assumed that the fast-time components (the $r_i(t)$, $r_{ci}(t)$, and $r_{si}(t)$ terms) of the received return are treated as constants when passing through the slow-time low-pass filter.

The first MIMO channel is the easiest to recover. The received return in (6.11) is simply passed through the slow-time low-pass filter. The resulting MIMO channel is shown in (6.12).

$$z_0(t) = \sum_{i=1}^{N} A_i r_i(t) e^{j2\pi f_{Di} t} \tag{6.12}$$

To achieve the MIMO channel that was modulated with a cosine wave, first the received return in (6.11) is multiplied by a cosine wave with a frequency of f_M. The result is shown in (6.13).

$$\begin{aligned}
z_c(t) &= s_{total}(t)\cos(2\pi f_M t) \\
z_c(t) &= \sum_{i=1}^{N} A_i r_i(t) e^{j2\pi f_{Di} t}\cos(2\pi f_M t) \\
&\quad + \frac{1}{2}\sum_{i=1}^{N} A_{ci} r_{ci}(t) e^{j2\pi f_{Dci} t}\cos(-2\pi f_M \tau_{ci}) \\
&\quad + \frac{1}{2}\sum_{i=1}^{N} A_{ci} r_{ci}(t) e^{j2\pi f_{Dci} t}\cos(2\pi 2 f_M t - 2\pi f_M \tau_{ci}) \\
&\quad + \frac{1}{2}\sum_{i=1}^{N} A_{si} r_{si}(t) e^{j2\pi f_{Dsi} t}\sin(2\pi 2 f_M t - 2\pi f_M \tau_{si}) \\
&\quad + \frac{1}{2}\sum_{i=1}^{N} A_{si} r_{si}(t) e^{j2\pi f_{Dsi} t}\sin(-2\pi f_M \tau_{si})
\end{aligned} \tag{6.13}$$

Then, (6.13) is passed through the slow-time low-pass filter, resulting in (6.14).

$$z_c(t) = \frac{1}{2}\sum_{i=1}^{N} A_{ci} r_{ci}(t) e^{j2\pi f_{Dci} t} \cos(-2\pi f_M \tau_{ci})$$

$$+ \frac{1}{2}\sum_{i=1}^{N} A_{si} r_{si}(t) e^{j2\pi f_{Dsi} t} \sin(-2\pi f_M \tau_{si}) \tag{6.14}$$

The first term in (6.14) is the desired MIMO channel, with some amplitude attenuation due to the $\frac{1}{2}$ and $\cos(-2\pi f_M \tau_{ci})$ multiplicative factors. The τ_{ci} terms represents the target delays. In many radar applications, $f_M \tau_{ci} \approx 0$, so $\cos(-2\pi f_M \tau_{ci}) \approx 1$ and only the factor of $\frac{1}{2}$ remains. The second term in (6.14) is a cross-talk term from the MIMO channel that uses the same mixing frequency but is 90 degrees out of phase. However, as previously stated, in many radar applications, $f_M \tau_{si} \approx 0$, and therefore $\sin(-2\pi f_M \tau_{si}) \approx 0$ and the cross-talk term goes away. If this is not the case (which may happen with radars looking at targets hundreds of kilometers away), then cross-talk can be avoided by using only the in-phase (cosine) and not the quadrature (sine) of each mixing frequency at the transmitter, which will ensure there is zero cross-talk.

The MIMO channel that was modulated with a sine wave is recovered in a similar way. The received return in (6.11) is multiplied by a sine wave with a frequency of f_M. The result is shown in (6.15).

$$
\begin{aligned}
z_s(t) &= s_{total}(t)\sin(2\pi f_M t) \\
z_s(t) &= \sum_{i=1}^{N} A_i r_i(t) e^{j2\pi f_{Di} t}\sin(2\pi f_M t) \\
&\quad + \frac{1}{2}\sum_{i=1}^{N} A_{ci} r_{ci}(t) e^{j2\pi f_{Dci} t}\sin(2\pi 2 f_M t - 2\pi f_M \tau_{ci}) \\
&\quad + \frac{1}{2}\sum_{i=1}^{N} A_{ci} r_{ci}(t) e^{j2\pi f_{Dci} t}\sin(-2\pi f_M \tau_{ci}) \\
&\quad + \frac{1}{2}\sum_{i=1}^{N} A_{si} r_{si}(t) e^{j2\pi f_{Dsi} t}\cos(-2\pi f_M \tau_{si}) \\
&\quad + \frac{1}{2}\sum_{i=1}^{N} A_{si} r_{si}(t) e^{j2\pi f_{Dsi} t}\cos(2\pi 2 f_M t - 2\pi f_M \tau_{si})
\end{aligned} \tag{6.15}
$$

Then, (6.15) is passed through the slow-time low-pass filter, resulting in (6.16).

$$
\begin{aligned}
z_s(t) &= \frac{1}{2}\sum_{i=1}^{N} A_{ci} r_{ci}(t) e^{j2\pi f_{Dci} t}\sin(-2\pi f_M \tau_{ci}) \\
&\quad + \frac{1}{2}\sum_{i=1}^{N} A_{si} r_{si}(t) e^{j2\pi f_{Dsi} t}\cos(-2\pi f_M \tau_{si})
\end{aligned} \tag{6.16}
$$

Similar to the previous channel discussed, the second term in (6.16) is the desired MIMO channel with some attenuation, and the first term is a cross-talk term from the other MIMO channel that uses the same mixing frequency but is 90 degrees out of phase. As discussed above, in many radar applications the cross-talk term is negligible, and cross-talk can be completely avoided by using only the in-phase (cosine) of each mixing frequency at the transmitter.

This method also assumes that the initial phase of the cosine and sine mixing waveforms at the transmitter is known or can be accurately estimated. If it is not,

cross-talk can result. One way to completely avoid cross-talk is to only transmit on the in-phase of each mixing frequency at the transmitter.

The process to separate the MIMO channels is summarized below:

1. To recover the 1st MIMO channel:
    - Pass the receiver return through the slow-time low-pass filter
2. To recover the 2nd MIMO channel:
    - Multiply the receiver return by $\cos(2\pi f_M t)$
    - Pass the result through the slow-time low-pass filter
3. To recover the 3rd MIMO channel:
    - Multiply the receiver return by $\sin(2\pi f_M t)$
    - Pass the result through the slow-time low-pass filter

6.5 Baseband Interference and an Adaptive Suppression Algorithm

One issue that was discovered in the design of the STRADAR system was baseband interference causing "phantom" targets to appear. This interference was investigated and determined to have originated in a switching power supply circuit. Additional RF shielding and bypass capacitors were added to the printed circuit board, which drastically reduced the interference strength. At the same time, a parallel solution involving solely signal processing was investigated, and this signal processing solution is presented here. The signal processing solution hinges on the fact that the baseband interference does not have a 90 degree phase relationship between its "in-phase" (I) and "quadrature" (Q) channels.

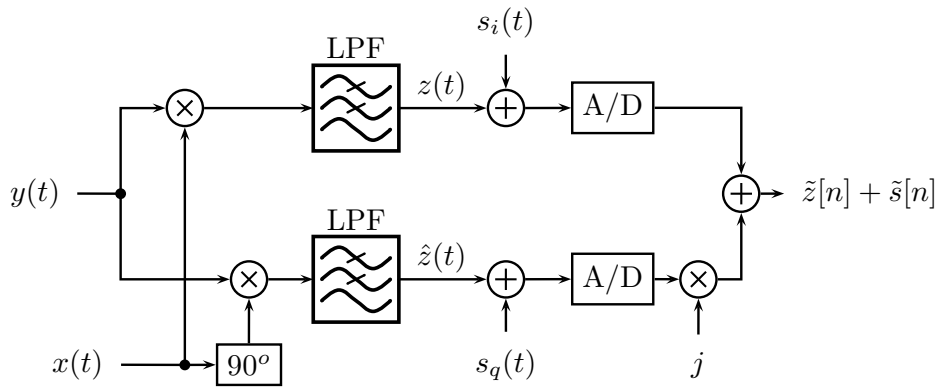

FIGURE 6.7: Heterodyne Radar Receiver with Additive Baseband Interference

Consider the block diagram in Fig. 6.7. This block diagram represents the radar I/Q demodulator. $x(t)$ is the original LFM-CW pulse-train, $y(t)$ is the sum of all the received backscatter, and $z(t)$ is the demodulated output without interference. $s(t)$ is the baseband interference. The baseband interference mixes in after I/Q demodulation, but before digital sampling. The baseband interference is a single tone sinusoid, whose frequency slowly drifts over time. It mixes into both the I and Q channels. The amplitudes and phases are not identical, but are very close. From channel to channel, the phases are very close, such that the interference appears to be coming from the "broadside" direction after beamforming. The interference signals on the I and Q channels are represented as:

$$\begin{aligned} s_i(t) &= A_1 \cos\left(2\pi f_s t + \pi\alpha t^2 + \theta_1\right) \\ s_q(t) &= A_2 \cos\left(2\pi f_s t + \pi\alpha t^2 + \theta_2\right) \\ \alpha &\ll f_s \end{aligned} \tag{6.17}$$

The terms A_1 and A_2 represent the amplitude of the baseband interference signal on the 'I' and 'Q' channels respectively. The term f_s represents the interference frequency. The term α represents the frequency walk rate. The terms θ_1 and θ_2 represent the initial phases of the signal on the 'I' and 'Q' channels. After digital sampling,

the 'I' and 'Q' signals are combined to form a complex signal. For a legitimate RF signal, the complex signal is analytic (one-sided in the frequency domain), because the I/Q demodulation performs the Hilbert transform operation. But, the baseband interference signals do not exhibit the 90 degree phase offset between 'I' and 'Q', and therefore the resulting complex signal is not analytic, but rather it is double-sided in the frequency domain. Because of differences in amplitude and phase between the 'I' and 'Q' signals, the frequency spectrum is not exactly conjugate symmetric.

The interference signals are continuous across radar pulses, which causes them to have a different initial phase on each pulse. This causes the "phantom targets" caused by the interference to appear to be Doppler-shifted. In addition, because of the frequency drift of the interference signals, the "phantom targets" appear to slowly drift in delay and Doppler over time. Finally, due to the fact that the initial phases of the interference signals across array channels is nearly identical, the "phantom targets" appear at broadside and their signal-to-noise ratio (SNR) is enhanced by beamforming.

The only differentiating factor between the "phantom targets" and legitimate scatterers is that the signals representing the legitimate scatterers are analytic and the signals representing the "phantom targets" are not. The spectrum of true targets, $Z_i(f)$, and of spurious "phantom" targets, $S_i(f)$, are shown in Equation (6.18).

$$\begin{aligned} Z_i(f) &= \tilde{A}_z \delta(f + \frac{\beta}{T}\tau_i) \\ S_i(f) &= \tilde{A}_{s1}\delta(f + f_s) + \tilde{A}_{s2}\delta(f - f_s) \end{aligned} \tag{6.18}$$

Note that the spectrum of the true targets is one-sided, and that the spectrum of the "phantom" targets is two-sided. This fact can be exploited to adaptively cancel the "phantom" targets. However, the amplitudes and phases of the two halves of the interference spectrum are not equal, and therefore an adaptive algorithm must

be employed to cancel it.

6.5.1 Adaptive Baseband Interference Cancellation Algorithm

The Wiener filter [83] is the adaptive method chosen to cancel the interference signal. By exploiting the fact that the desired radar signal is analytic and the interference signal is not, training data can be obtained. The data is pulse-compressed by taking the Fourier transform of each pulse, which transforms the intra-pulse dimension to physical time delay/slant range. Since the radar data is analytic, its spectrum is one-sided, which makes physical sense, as there can not be any negative ranges. But the interference signal is not analytic, and therefore its spectrum is two-sided. As stated in Section 6.5, due to small amplitude and phase discrepancies between the 'I' and 'Q' components, the interference signal spectrum is not exactly conjugate symmetric, so simply subtracting one side of the spectrum from the other will not completely suppress the interference. However, the conjugate halves of the interference signal spectrum are highly correlated, and therefore a 1-tap Wiener filter can suppress the interference. The half of the spectrum that only contains the interference signal is used as "training" data, and the half of the spectrum that contains both the true radar signals and the interference signal is the "testing" data. The Wiener filter is:

$$\mathbf{w} = \mathbf{R}^{-1}\mathbf{p} \tag{6.19}$$

.

The vector $\mathbf{w}$ contains the adaptive weights, the matrix $\mathbf{R}$ is the autocorrelation matrix of the interference signal, and the vector $\mathbf{p}$ is the cross-correlation of the interference signal and the radar signals. Since a 1-tap Wiener filter is being used, all of these components reduce to scalars. If the filter is unstable, then minimum-variance distortionless-response (MVDR) formulation with a small amount of diagonal loading may be used.

Since the frequency of the interference signal is not known a priori, the filter will have to be applied sequentially to each time delay/slant range, and are processed independent of each other. Since there should be nothing in the "negative range" half of the spectrum except for the interference signals, at ranges where there is no interference the Wiener filter should have no effect, except for very slightly increasing the noise (no more than 3 dB).

For the filter to work as intended, the interference signal must be the dominant signal in the training data. However, at any given range, the clutter will be the dominant feature. Theoretically, the clutter should not appear in the "negative range" half of the baseband spectrum. But, due to imperfect image rejection in the radar circuitry, an "echo" of the radar data will appear on the opposite side of the spectrum greatly attenuated (on the STRADAR, approximately 30-40 dB is typical). But since the clutter-to-interference ratio is high to begin with (typically anywhere between 30-60 dB on STRADAR) even the attenuated "echo" will appear in the training data. To compensate for this, a "clutter removal" filter must be applied on the training data. For stationary radar systems, this is relatively easy to implement (a high-pass filter across pulses). The steps of the algorithm are summarized below.

1. Range process the dechirped data by performing a discrete Fourier transform.
2. Designate the half of the spectrum that corresponds to "negative ranges" as the training data.
3. Apply a clutter-removal filter to the training data by filtering across pulses.
4. Apply a conjugate transform to the training data.
5. For each frequency, form the Wiener filter weight $\mathbf{w} = \mathbf{R}^{-1}\mathbf{p}$ and then apply the Wiener filter

6. If the above results in an unstable filter, use the MVDR weight formulation instead

6.5.2 Simulation and Real Data Results

Results of the algorithm are provided. Both simulation and real data results were collected. In both the simulation and the real data, a LFM-CW radar operating at a center frequency of 2.4 GHz, a swept bandwidth of 600 MHz, a waveform repetition frequency (WRF) of 100 Hz, and a coherent integration time (CIT) of 0.5 s were assumed. For the simulation data, Figure 6.8(a) shows an amplitude-range-Doppler (ARD) surface of the data before the interference suppression method is applied, and Figure 6.8(b) shows the ARD surface of the data after the interference suppression algorithm is applied. There are two legitimate targets, and a "phantom" target caused by the interference. The "phantom" target is circled to identify it. Note that in this plot of the ARD surface, there is no way to distinguish the true targets from the interference. Only by looking at the so-called "negative range" spectrum (not displayed here) can the interference be identified. From looking at these two surfaces, it is apparent that the interference is suppressed below the noise floor.

Real data from the STRADAR was also collected. Figure 6.9(a) the original ARD surface, with two "phantom" targets in the data, and Figure 6.9(b) after applying the interference suppression algorithm. Again, the "phantom" targets were distinguished from legitimate targets by examining the "negative ranges". Note that the interference signal is suppressed below the noise floor but the remaining data is unaffected.

6.6 Summary

The STRADAR tesbed was developed to support MIMO radar research. An overview of the system was provided, including the novel implementation of MIMO waveforms

via the double-sideband and quadrature MIMO waveforms. A technique for suppressing baseband interference is summarized, which is extendable to other heterodyne radar systems.

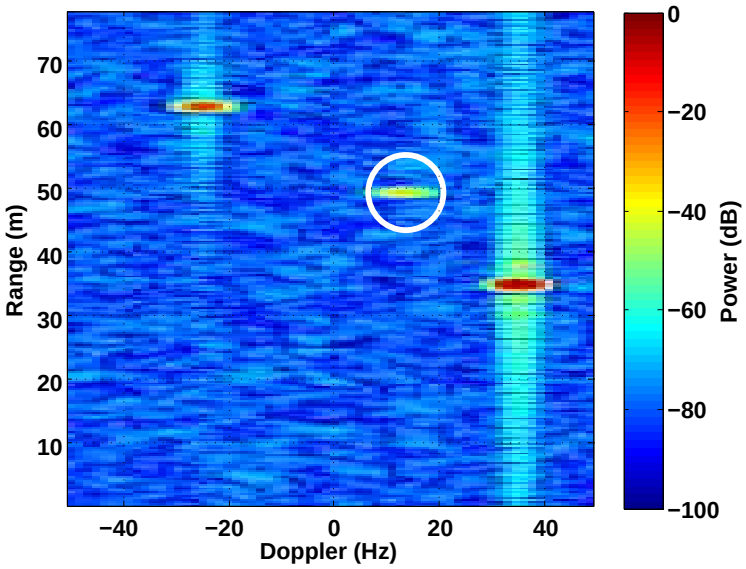

(a) Before spur removal

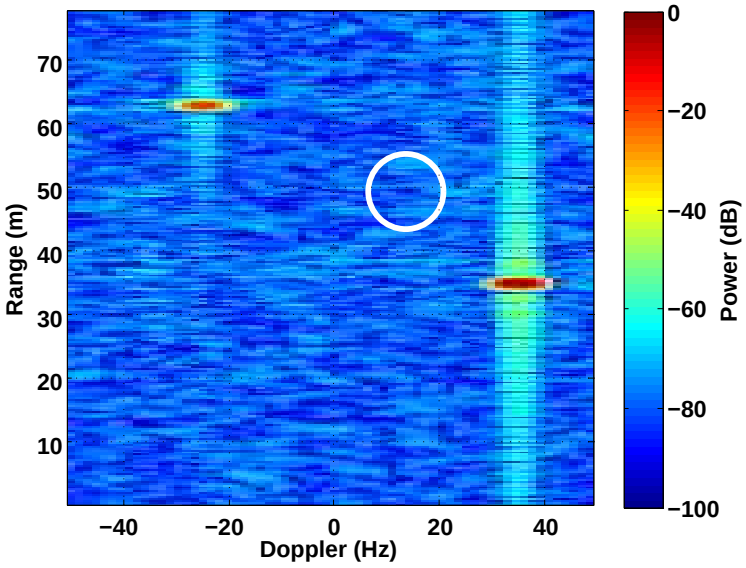

(b) After spur removal

FIGURE 6.8: Simulation results

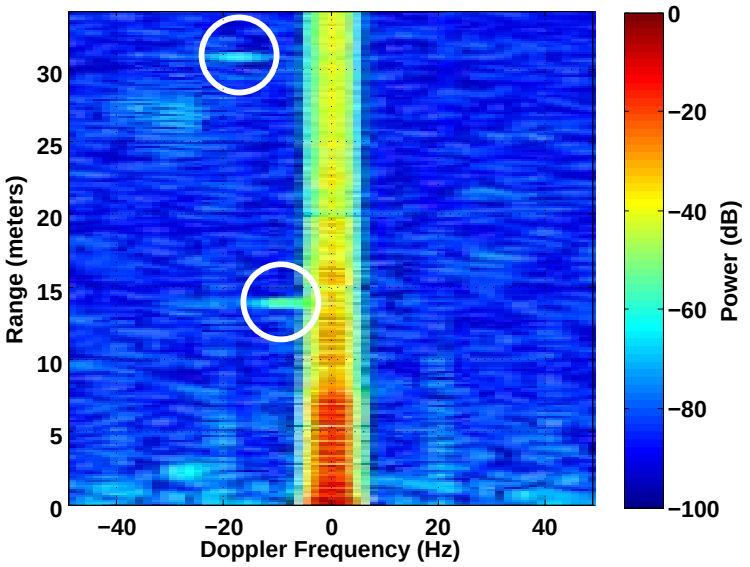

(a) Before spur removal

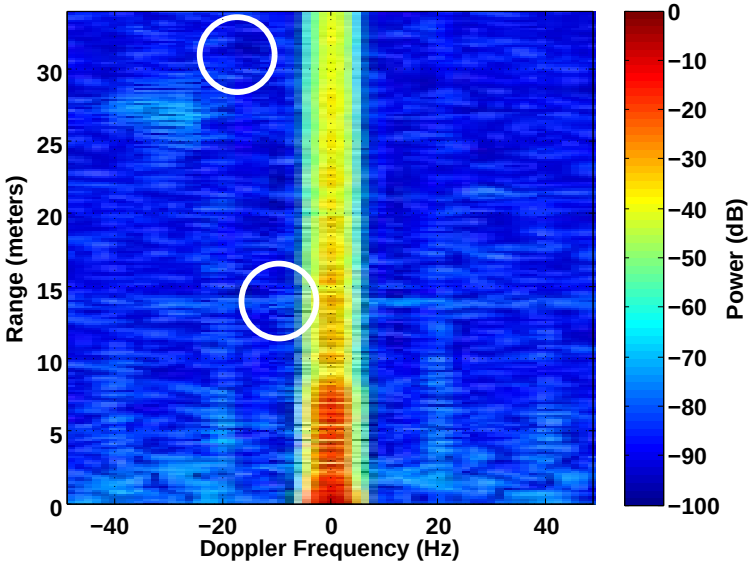

(b) After spur removal

FIGURE 6.9: STRADAR real data results

7

Experimental results from the STRADAR

This chapter includes some experimental results of the STRADAR.

7.1 MIMO GMTI

To test the ability to suppress spread-Doppler multipath clutter, the STRADAR was mounted to a passenger vehicle. To simulate the scenario described in Chapter 4, it was driven parallel to a long wall, at the Duke University Smith Warehouse. Photos of the STRADAR mounted to the vehicle are shown in Fig. 7.1 and Fig. 7.2. Fig. 7.3 shows the view from the car dashboard as it was driving along the wall.

The receiver array was mounted at a height of 2.46 m above the ground, and had 16 elements spaced at 0.05715 m. All of the receive antennas were 1/2 wave dipole antennas. The transmitter array was mounted at a height of 2.29 m above the ground, and had 4 elements spaced at 0.1143 m. All of the transmit antennas were patch antennas with a horizontal beamwidth of 75 degrees, a vertical beamwidth of 65 degrees, and a gain of 8 dBi. The transmit element spacing of 0.1143 m was the smallest possible, given the physical size of the antennas. This transmit spacing does result in the transmit array being sampled below Nyquist. The wall was 1.5

FIGURE 7.1: The STRADAR on a SUV

m to the left of the car. The radar center frequency was 2.4 GHz. The bandwidth was chosen to be 300 MHz (the full bandwidth of 600 MHz was not used to gain more range extent. See Chapter 6, section 6.1.1). The WRF was selected to be 400 Hz. MIMO channel 1 had a modulating frequency of 100 Hz and a phase offset of 0 degrees. MIMO channel 2 had a modulating frequency of 100 Hz and a phase offset of 90 degrees. MIMO channel 3 had a modulating frequency of 200 Hz and a phase offset of 90 degrees. MIMO channel 4 was not modulated. The car was driven at an extremely slow speed (approximately 5 mph). With these parameter, the Doppler-azimuth loci at a range of 10 m should theoretically take the form shown in Fig. 7.4.

To view the output as a SIMO system would, only one MIMO channel was used, and the other three ignored. A Doppler-azimuth plot at a range of 10 m is shown in Fig. 7.5. Observe the similarity to the theoretical clutter loci of Fig. 7.4. Compare

FIGURE 7.2: Side view of the STRADAR on a SUV

this to Fig. 7.6, which shows the MIMO beamformed result. Observe that much of the clutter has been suppressed, especially in locations the theoretical clutter loci would indicate correspond to multipath. Note however, that some clutter remains. This is most likely due to a small amount of direct-path clutter coming from the wall or the ground around it, due to the wall not being perfectly specular. Notice on both plots, some clutter appears at zero Doppler. This is due to reflections off of the car itself, which is moving at the same speed as the radar.

There were some issues that arose with this experiment. Initially, the goal was to detect a pedestrian. However, it was discovered that it was difficult to detect a pedestrian due to the height of both the transmit array and the receive array on the vehicle. The heights of both arrays were above the height of the pedestrian, and given the antenna beampatterns, this greatly reduced signal-to-noise ratio. Additionally, given the limitations to the maximum range due to the STRADAR's

FIGURE 7.3: View from the car dashboard

baseband sampling frequency, and to the available range-Doppler space due to using the double-sideband SLO-MO MIMO waveforms, the vehicle had to be driven very slowly to avoid Dopper aliasing.

7.2 Clutter-based Adaptive MIMO Phased Array Calibration

An experiment was performed to test the clutter-based calibration scheme proposed in Chapter 5. The experiment took place in the field between the Fitzpatrick Center and Hudson Hall at Duke University. First, a MIMO dataset of the ground clutter was collected, as shown in Fig. 7.7. The receiver beamforming weights were generated adaptively from this data. Next, a dataset of a point source aimed at the receive array was taken, as shown in Fig. 7.8. The receiver weights were then applied to this point source data as a test. For the MIMO case, the transmit array was a uniform linear array spaced

The same antennas arrays were used as the GMTI experiment. The receiver array had 16 elements spaced at 0.05715 m, and all of the elements were 1/2 wave dipole antennas. The transmitter array had 4 elements spaced at 0.1143 m, and all of the transmit antennas were patch antennas with a horizontal beamwidth of 75 degrees, a

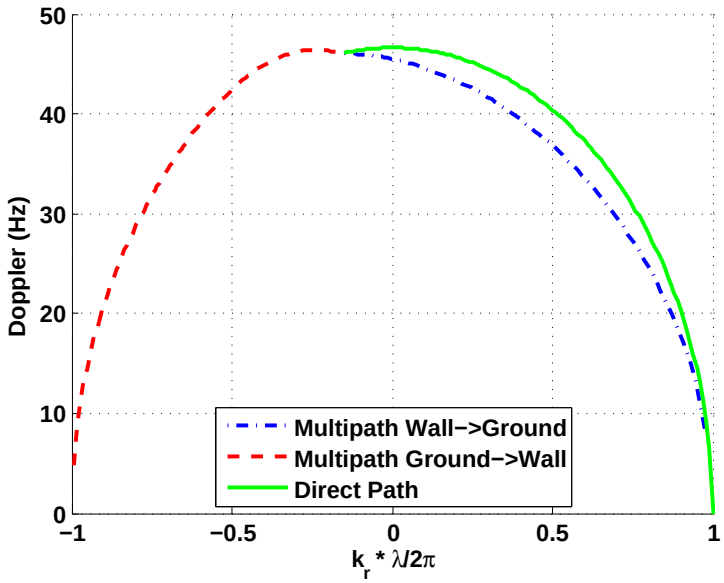

FIGURE 7.4: Theoretical Clutter Loci for the Experiment at a range = 10 m

vertical beamwidth of 65 degrees, and a gain of 8 dBi. Given the size of the transmit antennas, this is the closest they could be physically spaced.

It is important that note that initially good results could not be obtained with the algorithm as described in Chapter 5. This was determined to be because of a limited number of snapshots, given the STRADAR's ability to only illuminate a small range. Additionally, the transmit antennas were not omni-directional, but had a discrete beamwidth, further limiting data from some angles. However, the method was able to be slightly modified to achieve good results. The estimated receive wavefront vectors were generated as originally described. Recall, then, after generating the wavefront vectors, the next step is to generate the MVDR weights:

$$\mathbf{w}_r = \frac{\mathbf{R}_{SL}^{-1}\hat{\mathbf{v}}_r(\mathbf{k}_i)}{\hat{\mathbf{v}}_r^H(\mathbf{k}_i)\mathbf{R}_{SL}^{-1}\hat{\mathbf{v}}_r(\mathbf{k}_i)} \tag{7.1}$$

These weights are generated from an adaptively estimated steering vector $\hat{\mathbf{v}}$ and an adaptively estimately sidelobe matrix $\mathbf{R}_{SL}$. Replacing the adaptively estimated steering vector $\hat{\mathbf{v}}$ with the nominal steering vector $\mathbf{v}$, while keeping the adaptively

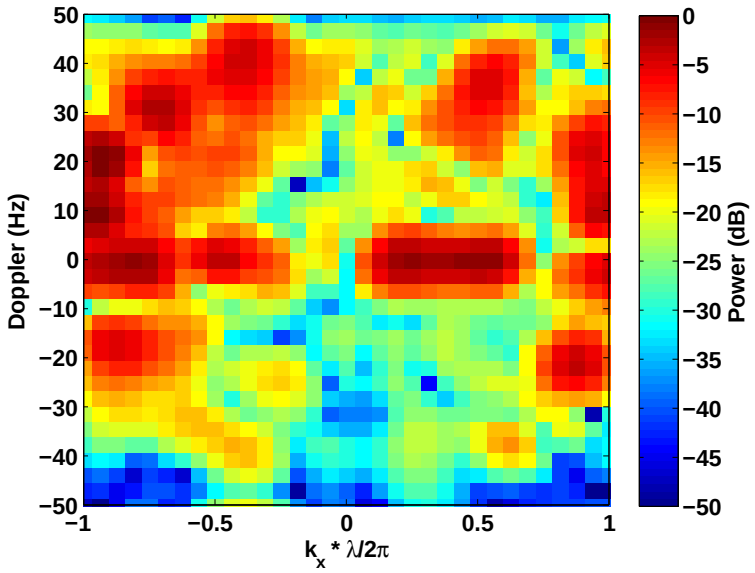

FIGURE 7.5: SIMO Doppler-azimuth plot at a range of 10 m

estimated sidelobe matrix, provides robustness. The result is shown in Fig. 7.9. Observe that the proposed algorithm, CAMPAC, achieves lower sidelobes than the Hamming window.

7.3 Summary

An experiment with the STRADAR on a moving vehicle was conducted, and it illustrates the multipath clutter model and the ability of MIMO beamforming to mitigate multipath clutter. A second experiment using the STRADAR in the presence of direct-path ground clutter to calibrate the array via the clutter-based adaptive MIMO phased-array calibration (CAMPAC) algorithm was conducted, and it demonstrates the CAMPAC algorithm.

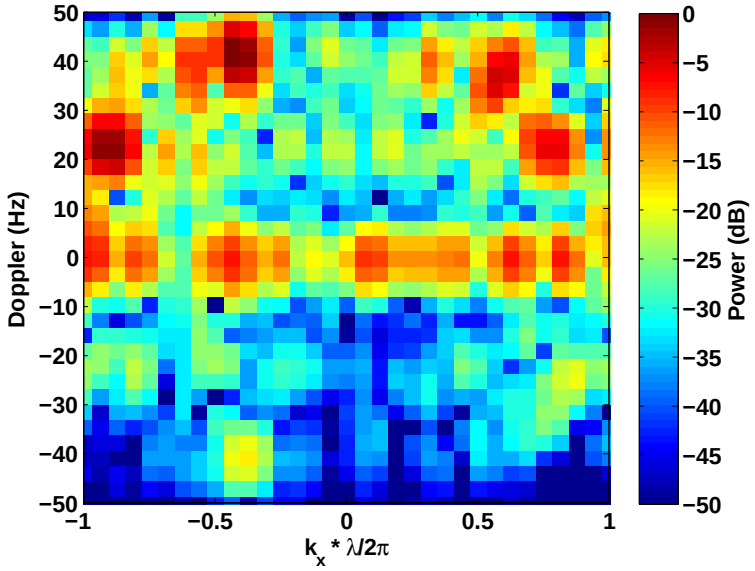

FIGURE 7.6: MIMO Doppler-azimuth plot at a range of 10 m

FIGURE 7.7: Setup of calibration experiment to obtain clutter training data

FIGURE 7.8: Setup of the calibration experiment to obtain point source testing data

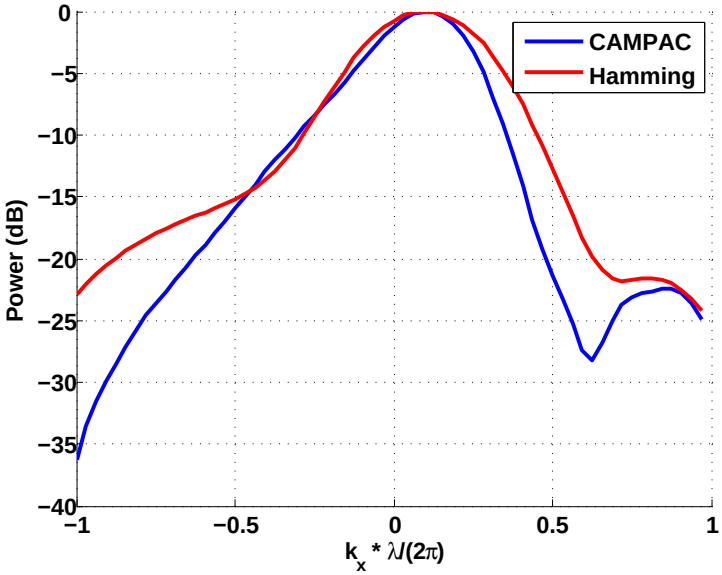

FIGURE 7.9: Results of the clutter-based calibration experiment

8

Conclusion and Future Work

Multipath propagation in radar systems is an important effect that is often neglected or overlooked. This is most likely because the first radar systems monitored the sky, where multipath is not significant. However, as radar expands to different applications, such as indoor radar and urban radar, multipath becomes a significant factor which cannot be ignored. Multipath propagations, especially Doppler-shifted and Doppler-spread multipath propagations, can appear as false targets or obscure legitimate targets. In the over-the-horizon radar community, MIMO radar can has shown to be successful to mitigate spread-Doppler multipath clutter. Over-the-horizon radar is unique in the sense that only limited modes can physically propagate, and therefore any multipath will come from discrete direction-of-departures angles and direction-of-arrival angles. The work presented in this dissertation considered a case in which multipath would appear along a continuum of direction-of-departure and direction-of-arrival angles.

The feature of MIMO radar that allows for multipath suppression is that MIMO radar allows for discrimination in both transmit angle (direction-of-departure) and receive angle (direction-of-arrival). This concept was mathematically formalized in

the MIMO bi-directional spatial spectrum, introduced in Chapter 3. This spectrum, which is a function of both transmit angle and receive angle, characterizes propagation paths for a given environment. Each discrete path appears as impulse in this domain. Paths along the diagonal of the spectrum, where $\mathbf{k}_r = \mathbf{k}_t$, can be classified as "direct-path" paths. Any path not on the diagonal, by definition, are multipath paths. It is only by going to this bi-directional spatial domain that multipath returns can be definitively discriminated from direct-path returns. In other traditional radar domains (range, velocity, and receive-angle only) there is the ability for multipath returns and direct-path returns to overlap and obscure each other. The bi-directional spatial spectrum, therefore, is crucial for suppressing multipath returns without also suppressing desired direct-path returns.

The ability of any adaptive algorithm to suppress interference is dependent upon the rank of the interference covariance matrix. The rank determines the number of adaptive degrees of freedom needed to suppress the interference. With a low interference rank, only a small number of adaptive degrees of freedom are needed, and with a high interference rank, many adaptive degrees of freedom are needed. In turn, then number of adaptive degrees of freedom determines the amount of training data that the adaptive algorithm requires. For the radar applications discussed in this dissertation, the interference is the radar clutter, and more specifically, the multipath clutter. The bi-directional spatial spectrum provides a method of estimating the rank of the clutter covariance matrix. The bi-directional spectrum decomposes a given MIMO data vector into a sum of orthogonal bi-directional basis vectors. Each basis vector represents one transmit-receive propagation path. By definition, the rank of a matrix is the number of orthogonal basis vectors required to span the subspace spanned by the columns of the matrix. Therefore, the number of components in the spectrum, or the number of "occupied" resolution cells, provides an estimate of the clutter rank. Simulation results included in this dissertation showed that this

method of rank estimation is accurate.

With the rank of the clutter covariance matrix able to be accurately estimated, a partially-adaptive multipath suppression algorithm was proposed. This technique, based off of techniques used for non-MIMO radar, finds the optimum dimensionality-reducing transformation matrix, in terms of the output signal-to-clutter-plus-noise (SCNR) ratio, for a given number of adaptive degrees of freedom. The number of adaptive degrees of freedom is a user-selected variable, however, the rank of the clutter covariance matrix determines this choice and this work presented an accurate technique to estimate the rank. The algorithm was applied to the scenario of a ground-vehicle-mounted MIMO radar system driving on the ground next to a large specular reflector, and a pedestrian is walking in front of the vehicle. The goal of the radar is to detect the pedestrian. However, this geometry creates multipath clutter returns that results from a continuum of transmit angles and receive angles, which is non-separable in the bi-directional spatial domain and obscures the pedestrian. SIMO (receive-only) adaptive beamforming is unable to distinguish the pedestrian from the multipath, as a portion of the multipath clutter appears at the same direction-of-arrival as the target. Simulation results showed that the proposed MIMO algorithm was able to successfully suppress multipath clutter returns, and distinguish the target, both in the case where the clutter covariance matrix was known a priori and in the case when the clutter covariance matrix was estimated from slow-time pulses. Monte Carlo simulations showed that this algorithm was able to achieve excellent detection performance with a realistic amount of training data. Another set of Monte Carlo simulations evaluated the case in which the target's azimuth angle and velocity were made into random variables, the proposed MIMO algorithm achieved vastly superior detection results than an adaptive SIMO algorithm.

In Chapter 5, a different application of MIMO radar was presented: calibration of a phased array from ground clutter. Electronically-steered phased arrays require

proper calibration to achieve the theoretically-predicted sidelobe performance. Traditionally phased arrays are calibrated by placing point sources or point targets in the field, and adjusting the calibration parameters to achieve the desired point response. However, in many instances it can be impractical or impossible to place point sources around a radar system, or if it is possible, only a few point sources can be placed. Some sources of miscalibration, such as mutual coupling, have effects that vary as a function of look direction, and thus would require a separate calibration for each look direction. MIMO radar offers the ability to calibrate using ground clutter. In a SIMO system, ground clutter appears at all azimuth angles, and is not useful. However, in the MIMO bi-directional spatial spectrum, ground clutter appears along the direct-path diagonal. The transmit array can be used to isolate a patch of ground clutter that would then appear as a point source to the receive array. MIMO beamforming after-the-fact allows the transmit array to be steered to all look directions, thus creating a set of clutter patches that approximates a point source to the receive array. With a virtual point target in every look direction, receive steering vectors for each look direction can be estimated. From this set of estimated look vectors, receive beamforming weights can be generated for every look direction. Simulation results showed that the proposed calibration approach achieved significantly lower sidelobes than from applying a Hamming window to the uncalibrated data, even when the number of transmitters was less than the number of receivers. Monte Carlo results evaluated the performance of the algorithm in terms of clutter-to-noise-ratio (CNR) and number of snapshots, and showed that in most instances the proposed method achieved superior sidelobes to the Hamming window.

To evaluate the algorithms presented in this work, as well as related radar and array processing algorithms, a low-power MIMO S-band radar testbed, named the STRADAR, was developed. This testbed has a center frequency of 2.4 GHz, a swept RF bandwidth of 600 MHz, 16 coherent receiver channels, and a transmitter than

can operate in SIMO or MIMO mode. In MIMO mode, up to 4 MIMO channels possible. In order to implement MIMO in a simple and cost-efficient manner, the double-sideband SLO-MO MIMO waveforms were proposed (and implemented). The double-sideband SLO-MO waveforms use passive RF mixers to mix in a baseband sinusoid, which shifts each MIMO channel in Doppler. The MIMO channels can then be separated by filtering in Doppler. One issue that came up in the development of this testbed was the presence of an interference signal from a switching power supply which appeared as false target. This problem was solved in two ways. The first way was to re-design the power supply board with more attention to RF shielding and bypass capacitors. The second way was a signal processing solution which exploited the fact that the baseband interference was not coherent across the in-phase and quadrature channels of the receiver. Simulation and real data results showed this algorithm was successful in suppressing this interference.

The STRADAR was then used experimentally to test the algorithms that were earlier proposed in this dissertation: multipath clutter suppression in ground-vehicle GMTI radar and clutter-based adaptive MIMO phased-array calibration. For the GMTI problem, the STRADAR was a mounted to the roof of a passenger vehicle (a sports-utility vehicle (SUV)) and was driven next to a large, long wall. Experimental results showed that MIMO radar significantly suppressed the multipath clutter. Thus, MIMO radar has the potential for ground-vehicle GMTI radar. However, there were some issues revealed by this experiment. Mounting the radar to the roof of a SUV made it difficult to detect a pedestrian, as the height of both the transmit array and receive array were above the height of the pedestrian. Additionally, due to the sampling frequency limitations of the STRADAR, which limits the maximum range, combined with the reduced range-Doppler space of MIMO, the vehicle had to be driven very slowly to avoid Doppler aliasing. Another experiment was performed to test calibration from clutter. This experiment involved taking a MIMO data set in

an open field to generate calibration parameters, and then placing a point target in the field as testing data. However, due to the low power of the STRADAR, there were not many range snapshots to train over and initially good results were not created. Additionally, the transmit antennas had a beampattern that was not uniform, resulting in returns that were not equal across angle. A slight modification to the calibration method, using the assumed steering vector instead of the adaptively-generated steering vector (while still using the adaptively-generated sidelobe matrix) was able to achieve a result that was improved over the Hamming window.

The results in this dissertation show that MIMO radar shows potential for ground-vehicle GMTI radar and for calibration from clutter. However, the limitations of MIMO radar, especially the reduction in available range-Doppler space, must be taken into account. The restrictions of these limitations became clear in the development and use of the STRADAR testbed. MIMO radar also results in a reduction of signal-to-noise ratio compared to an equivalent SIMO system. Given these limitations, it is important to evaluate whether MIMO radar is advantageous in a given scenario. Future work on this area includes:

1. An examination of the effectiveness of the MIMO adaptive multipath suppression algorithm in more complicated scenarios should be conducted. The scenario presented in this work involved a ground-vehicle driving at a constant velocity next to a perfectly specular reflector. This scenario, while informative, is not representative of all the scenarios encountered in an urban environment. Examination of scenarios with multiple non-ground reflectors (building walls, guardrails, lampposts, etc.). Another scenario that should be examined is multipath off of other moving cars. The work in this dissertation assumed that the only moving object was the vehicle with the radar. However, a realistic environment would have several moving cars, some moving in the same direction

as the moving vehicle and others moving in the opposite direction. Also, the case of a varying velocity on the primary vehicle must be considered.

2. Experiments for a variety of GMTI scenarios should be conducted. Given the problems that arose from mounting the radar to a roof of the car, due to the height of the arrays above pedestrians, other locations for the radar should be considered, such as the hood of the car. Additionally, perhaps instead of a pedestrian, a radar beacon or transponder could be mounted to a tripod and placed alongside the road. This would create a more consistent and repeatable target signal.

3. Regarding the calibration from clutter algorithm, cases should be considered in scenarios where the strength of the clutter is angle-dependent. In these cases, steering the transmit array in different directions will isolate clutter patches of varying strengths. The effect of this on the calibration algorithm needs to be determined.

4. Representations of the MIMO bi-directional spatial spectrum should be examined for the cases of two-dimensional and three-dimensional arrays. While the mathematical definition of the MIMO bi-directional spatial spectrum includes three-dimensional spatial frequency vectors, all of the examples considered in this dissertation had both arrays as one-dimensional line arrays. With multi-dimensional arrays, the bi-directional spectrum becomes a function of four variables: transmit azimuth angle, transmit elevation angle, receive azimuth angle, and receive elevation angle. Operating in this domain could open up new opportunities to further classify propagation paths and could potentially be used for channel modeling.

5. The development of an experimental testbed that has higher baseband sampling

frequencies, a higher RF bandwidth, and more elements on both transmit and receive would allow for the ability to perform a wider variety of experiments. Also, the existing software for the testbed requires one to collect data and process it offline, but with the appropriate processing chain could be re-written to implement real-time performance.

In summary, this work has shown MIMO radar can be used to be implement radar in applications that were previously precluded due to significant multipath, such as indoor and urban radar. The mathematical development of the MIMO bi-directional spatial spectrum creates a framework for many potential multipath classification, suppression, and modeling techniques to be developed. As the cost and size of RF circuitry and analog-to-digital converters continues to decrease, radar will be expanded to more and more applications. In some of these new applications, multipath will play a significant role, and MIMO can be used to solve the problems that arise.

Bibliography

[1] E. Fishler, A. Haimovich, R. Blum, D. Chizhik, L. Cimini, and R. Valenzuela, "MIMO radar: an idea whose time has come," in *Radar Conference, 2004. Proceedings of the IEEE*, pp. 71 – 78, Apr 2004.

[2] M. Richards, *Fundamentals of Radar Signal Processing*. McGraw-Hill, 2005.

[3] M. Skolnik, *Introduction to Radar Systems, Third Edition*. McGraw-Hill, 2001.

[4] M. Richards, J. Scheer, and W. Holm, *Principles of Modern Radar: Basic Principles*. SciTech Publishing, 2010.

[5] V. Mecca, D. Ramakrishnan, and J. Krolik, "MIMO radar space-time adaptive processing for multipath clutter mitigation," in *Sensor Array and Multichannel Processing, 2006. Fourth IEEE Workshop on*, pp. 249 –253, Jul 2006.

[6] Y. Yang and R. Blum, "MIMO radar waveform design based on mutual information and minimum mean-square error estimation," *Aerospace and Electronic Systems, IEEE Transactions on*, vol. 43, no. 1, pp. 330–343, 2007.

[7] Y. Yang and R. Blum, "Minimax robust MIMO radar waveform design," *Selected Topics in Signal Processing, IEEE Journal of*, vol. 1, no. 1, pp. 147–155, 2007.

[8] Y. Yang, R. Blum, Z. He, and D. Fuhrmann, "Mimo radar waveform design via alternating projection," *Signal Processing, IEEE Transactions on*, vol. 58, no. 3, pp. 1440–1445, 2010.

[9] B. Friedlander, "Waveform design for mimo radars," *Aerospace and Electronic Systems, IEEE Transactions on*, vol. 43, no. 3, pp. 1227–1238, 2007.

[10] G. San Antonio, D. Fuhrmann, and F. Robey, "MIMO radar ambiguity functions," *Selected Topics in Signal Processing, IEEE Journal of*, vol. 1, pp. 167 –177, Jun 2007.

[11] D. Fuhrmann and G. San Antonio, "Transmit beamforming for MIMO radar systems using signal cross-correlation," *Aerospace and Electronic Systems, IEEE Transactions on*, vol. 44, pp. 171 –186, Jan 2008.

[12] Y. Abramovich and G. Frazer, "Bounds on the volume and height distributions for the MIMO radar ambiguity function," *Signal Processing Letters, IEEE*, vol. 15, pp. 505 –508, 2008.

[13] Y. Abramovich and G. Frazer, "MIMO radar performance in clutter: Limitations imposed by bounds on the volume and height distributions for the MIMO radar ambiguity function," in *Sensor Array and Multichannel Signal Processing Workshop, 2008. SAM 2008. 5th IEEE*, pp. 441 –445, Jul 21-23 2008.

[14] H. Deng, "Polyphase code design for orthogonal netted radar systems," *Signal Processing, IEEE Transactions on*, vol. 52, pp. 3126 – 3135, Nov 2004.

[15] V. Mecca and J. Krolik, "Slow-time MIMO STAP with improved power efficiency," in *Signals, Systems and Computers, 2007. ACSSC 2007. Conference Record of the Forty-First Asilomar Conference on*, pp. 202 –206, Nov 2007.

[16] V. Mecca, J. Krolik, and F. Robey, "Beamspace slow-time MIMO radar for multipath clutter mitigation," in *Acoustics, Speech and Signal Processing, 2008. ICASSP 2008. IEEE International Conference on*, pp. 2313 –2316, 31 2008-Apr 4 2008.

[17] J. Krolik, V. Mecca, O. Kazanci, and I. Bilik, "Multipath spread-Doppler clutter mitigation for over-the-horizon radar," in *Radar Conference, 2008. RADAR '08. IEEE*, pp. 1 –5, May 2008.

[18] P. Stoica and J. Li, *MIMO Radar Signal Processing*, ch. 7, pp. 283–318. Hoboken, New Jersey: John Wiley & Sons, Inc., 2009.

[19] G. Frazer, Y. Abramovich, and B. Johnson, "Spatially waveform diverse radar: Perspectives for high frequency OTHR," in *Radar Conference, 2007 IEEE*, pp. 385 –390, Apr 17-20 2007.

[20] B. Johnson, Y. Abramovich, and G. Frazer, "HF skywave spatially diverse waveform radar: transmitter subsystem implementation issues," in *ARP '07: The Fourth IASTED International Conference on Antennas, Radar and Wave Propagation*, (Anaheim, CA, USA), pp. 208–213, ACTA Press, 2007.

[21] G. Frazer, B. Johnson, and Y. Abramovich, "Orthogonal waveform support in MIMO HF OTH radars," in *Waveform Diversity and Design Conference, 2007. International*, pp. 423 –427, Jun 4-8 2007.

[22] J. Li, L. Xu, P. Stoica, K. Forsythe, and D. Bliss, "Range compression and waveform optimization for MIMO radar: A Cramer-Rao bound based study," *Signal Processing, IEEE Transactions on*, vol. 56, no. 1, pp. 218–232, 2008.

[23] C.-Y. Chen and P. Vaidyanathan, "MIMO radar ambiguity properties and optimization using frequency-hopping waveforms," *Signal Processing, IEEE Transactions on*, vol. 56, no. 12, pp. 5926–5936, 2008.

[24] C.-Y. Chen and P. Vaidyanathan, "MIMO radar waveform optimization with prior information of the extended target and clutter," *Signal Processing, IEEE Transactions on*, vol. 57, no. 9, pp. 3533–3544, 2009.

[25] K. Forsythe and D. Bliss, "MIMO radar waveform constraints for GMTI," *Selected Topics in Signal Processing, IEEE Journal of*, vol. 4, no. 1, pp. 21–32, 2010.

[26] B. Tang, J. Tang, and Y. Peng, "MIMO radar waveform design in colored noise based on information theory," *Signal Processing, IEEE Transactions on*, vol. 58, no. 9, pp. 4684–4697, 2010.

[27] B. Tang, J. Tang, and Y. Peng, "Waveform optimization for MIMO radar in colored noise: Further results for estimation-oriented criteria," *Signal Processing, IEEE Transactions on*, vol. 60, no. 3, pp. 1517–1522, 2012.

[28] D. J. Rabideau, "MIMO radar waveforms and cancellation ratio," *Aerospace and Electronic Systems, IEEE Transactions on*, vol. 48, no. 2, pp. 1167–1178, 2012.

[29] G. Babur, O. Krasnov, A. Yarovoy, and P. Aubry, "Nearly orthogonal waveforms for MIMO FMCW radar," *Aerospace and Electronic Systems, IEEE Transactions on*, vol. 49, no. 3, pp. 1426–1437, 2013.

[30] E. Fishler, A. Haimovich, R. Blum, R. Cimini, D. Chizhik, and R. Valenzuela, "Performance of MIMO radar systems: advantages of angular diversity," in *Signals, Systems and Computers, 2004. Conference Record of the Thirty-Eighth Asilomar Conference on*, vol. 1, pp. 305 – 309, Nov 2004.

[31] E. Fishler, A. Haimovich, R. Blum, J. Cimini, L.J., D. Chizhik, and R. Valenzuela, "Spatial diversity in radars-models and detection performance," *Signal Processing, IEEE Transactions on*, vol. 54, pp. 823 – 838, Mar 2006.

[32] N. Lehmann, E. Fishler, A. Haimovich, R. Blum, D. Chizhik, L. Cimini, and R. Valenzuela, "Evaluation of transmit diversity in MIMO-radar direction finding," *Signal Processing, IEEE Transactions on*, vol. 55, pp. 2215 –2225, May 2007.

[33] A. Haimovich, R. Blum, and L. Cimini, "MIMO radar with widely separated antennas," *Signal Processing Magazine, IEEE*, vol. 25, no. 1, pp. 116 –129, 2008.

[34] V. Chernyak, "On the concept of MIMO radar," in *Radar Conference, 2010 IEEE*, pp. 327 –332, May 2010.

[35] D. Bliss and K. Forsythe, "Multiple-input multiple-output (MIMO) radar and imaging: degrees of freedom and resolution," in *Signals, Systems and Computers, 2003. Conference Record of the Thirty-Seventh Asilomar Conference on*, vol. 1, pp. 54 – 59, Nov 2003.

[36] K. Forsythe, D. Bliss, and G. Fawcett, "Multiple-input multiple-output (MIMO) radar: performance issues," in *Signals, Systems and Computers, 2004. Conference Record of the Thirty-Eighth Asilomar Conference on*, vol. 1, pp. 310 – 315, Nov 2004.

[37] F. Robey, S. Coutts, D. Weikle, J. McHarg, and K. Cuomo, "MIMO radar theory and experimental results," in *Signals, Systems and Computers, 2004. Conference Record of the Thirty-Eighth Asilomar Conference on*, vol. 1, pp. 300–304, 2004.

[38] D. Bliss, K. Forsythe, S. Davis, G. S. Fawcett, D. Rabideau, L. L. Horowitz, and S. Kraut, "GMTI MIMO radar," in *Waveform Diversity and Design Conference, 2009 International*, pp. 118–122, 2009.

[39] D. Bliss, "Coherent MIMO radar," in *Waveform Diversity and Design Conference (WDD), 2010 International*, pp. 1–1, 2010.

[40] J. Kantor and D. Bliss, "Clutter covariance matrices for GMTI MIMO radar," in *Signals, Systems and Computers (ASILOMAR), 2010 Conference Record of the Forty Fourth Asilomar Conference on*, pp. 1821–1826, 2010.

[41] B. Correll, J. Kantor, and D. Bliss, "Waveform-dependent bayesian cramer-rao angle-estimation bounds and threshold SNR estimates for MIMO radars," in *Radar Conference (RADAR), 2011 IEEE*, pp. 503–508, 2011.

[42] C.-Y. Chen and P. Vaidyanathan, "MIMO radar space time adaptive processing using prolate spheroidal wave functions," *Signal Processing, IEEE Transactions on*, vol. 56, no. 2, pp. 623–635, 2008.

[43] C. Y. Chong, F. Brigui, F. Pascal, and Y. K. Quek, "Clutter rank for slow-time MIMO STAP," in *Radar Conference (EuRAD), 2012 9th European*, pp. 54–56, 2012.

[44] G. Wang and Y. Lu, "Clutter rank of STAP in MIMO radar with waveform diversity," *Signal Processing, IEEE Transactions on*, vol. 58, no. 2, pp. 938–943, 2010.

[45] L. Sun, K. Jiang, B. cai Wu, and J. long Ge, "MIMO SAR/MTI system design and signal analysis for moving target indiction," in *Radar (Radar), 2011 IEEE CIE International Conference on*, vol. 1, pp. 116–121, 2011.

[46] L. Sun, K. Jiang, B. cai Wu, and J. long Ge, "MIMO SAR/MTI system design and signal analysis for moving target indiction," in *Radar (Radar), 2011 IEEE CIE International Conference on*, vol. 1, pp. 116–121, 2011.

[47] F. Ahmad, M. Amin, and Y.-S. Yoon, "Multi-input multi-output synthetic aperture radar technology for urban area surveillance," in *Synthetic Aperture Radar (APSAR), 2011 3rd International Asia-Pacific Conference on*, pp. 1–4, 2011.

[48] R. Hoctor and S. Kassam, "The unifying role of the coarray in aperture synthesis for coherent and incoherent imaging," *Proceedings of the IEEE*, vol. 78, pp. 735 –752, Apr 1990.

[49] F. Ahmad, G. Frazer, S. Kassam, and M. Amin, "Design and implementation of near-field, wideband synthetic aperture beamformers," *Aerospace and Electronic Systems, IEEE Transactions on*, vol. 40, pp. 206 – 220, Jan 2004.

[50] J. Li and P. Stoica, "MIMO radar with colocated antennas," *Signal Processing Magazine, IEEE*, vol. 24, pp. 106 –114, Sep 2007.

[51] G. Frazer, Y. Abramovich, B. Johnson, and F. Robey, "Recent results in MIMO over-the-horizon radar," in *Radar Conference, 2008. RADAR '08. IEEE*, pp. 1 –6, May 26-30 2008.

[52] G. Frazer, Y. Abramovich, and B. Johnson, "Use of adaptive non-causal transmit beamforming in OTHR: Experimental results," in *Radar, 2008 International Conference on*, pp. 311 –316, Sep 2-5 2008.

[53] G. Frazer, Y. Abramovich, and B. Johnson, "Multiple-input multiple-output over-the-horizon radar: experimental results," *Radar, Sonar Navigation, IET*, vol. 3, pp. 290 –303, Aug 2009.

[54] Y. Abramovich, G. Frazer, and B. Johnson, "Iterative adaptive kronecker MIMO radar beamformer: Description and convergence analysis," *Signal Processing, IEEE Transactions on*, vol. 58, pp. 3681 –3691, Jul 2010.

[55] V. Mecca and J. Krolik, "MIMO STAP clutter mitigation performance demonstration using acoustic arrays," in *Signals, Systems and Computers, 2008 42nd Asilomar Conference on*, pp. 634 –638, Oct 2008.

[56] G. Hickman and J. Krolik, "MIMO GMTI radar with multipath clutter suppression," in *2010 IEEE Sensor Array and Multichannel Signal Processing Workshop (SAM)*, pp. 65–68, Oct 2010.

[57] J. Ward, "Space-time adaptive processing for airborne radar," tech. rep., MIT Lincoln Laboratory, Dec 1994.

[58] L. Li and J. Krolik, "Vehicular MIMO SAR imaging in multipath environments," in *Radar Conference (RADAR), 2011 IEEE*, pp. 989–994, 2011.

[59] V. Mecca and J. Krolik, "MIMO enabled multipath clutter rank estimation," in *Radar Conference, 2009 IEEE*, pp. 1–6, 2009.

[60] D. Johnson and D. Dudgeon, *Array Signal Processing*. Prentice-Hall, 1993.

[61] D. Dudgeon and R. Mersereau, *Multidimensional Digital Signal Processing*. Prentice-Hall, 1984.

[62] S. Marple, *Digital Spectral Analysis with Applications*. Prentice-Hall, 1987.

[63] L. Brennan and F. Staudaher, "Subclutter visibility demonstration," tech. rep., Adaptive Sensors Incorporated, March 1992.

[64] V. Varadarajan and J. Krolik, "Joint space-time interpolation for distorted linear and bistatic array geometries," *Signal Processing, IEEE Transactions on*, vol. 54, no. 3, pp. 848–860, 2006.

[65] L. J. Griffiths and C. Jim, "An alternative approach to linearly constrained adaptive beamforming," *Antennas and Propagation, IEEE Transactions on*, vol. 30, no. 1, pp. 27–34, 1982.

[66] J. S. Goldstein and I. S. Reed, "Reduced-rank adaptive filtering," *Signal Processing, IEEE Transactions on*, vol. 45, no. 2, pp. 492–496, 1997.

[67] J. S. Goldstein and I. S. Reed, "Subspace selection for partially adaptive sensor array processing," *Aerospace and Electronic Systems, IEEE Transactions on*, vol. 33, no. 2, pp. 539–544, 1997.

[68] J. S. Goldstein and I. S. Reed, "Theory of partially adaptive radar," *Aerospace and Electronic Systems, IEEE Transactions on*, vol. 33, no. 4, pp. 1309–1325, 1997.

[69] F. Robey, D. Fuhrmann, and M. Koerber, "Array calibration and modeling of steering vectors," in *Conference Record of the Thirty-Fifth Asilomar Conference on Signals, Systems and Computers*, pp. 1121–1126, Nov 2001.

[70] I. Solomon, D. Gray, Y. Abramovich, and S. Anderson, "Receiver array calibration using disparate sources," *IEEE Transactions on Antennas and Propagation*, vol. 47, pp. 496–506, Mar 1999.

[71] E. Attia and B. Steinberg, "Self-cohering large antenna arrays using the spatial correlation properties of radar clutter," *IEEE Transactions on Antennas and Propagation*, vol. 37, pp. 30–38, Jan 1989.

[72] B. Ng and C. Samson, "Sensor-array calibration using a maximum likelihood approach," *IEEE Transactions on Antennas and Propagation*, vol. 44, pp. 827–836, Jun 1996.

[73] M. Viberg, M. Lanne, and A. Lundgren, "Calibration in array processing," in *Classical and Modern Direction-of-Arrival Estimation* (E. Tuncer and B. Friedlander, eds.), ch. 3, Academic Press, 2009.

[74] I. Gupta and A. Ksienski, "Effect of mutual coupling on the performance of adaptive arrays," *IEEE Transactions on Antennas and Propagation*, vol. 31, no. 5, pp. 785–791, 1983.

[75] A. Manikas and N. Fistas, "Modelling and estimation of mutual coupling between array elements," in *1994 IEEE International Conference on Acoustics, Speech, and Signal Processing (ICASSP-94)*, vol. 4, pp. 553–556, 1994.

[76] K. Stavropoulos and A. Manikas, "Array calibration in the presence of unknown sensor chracteristics and mutual coupling," in *2000 Proceedings of the European Signal Processing Conference (EUSIPCO)*, vol. 3, pp. 1417–1420, Sep 2000.

[77] A. Paulraj, T. Shan, V. Reddy, and T. Kailath, "A subspace approach to determining sensor gain and phase with applications to array processing," *SPIE Advanced Algorithms and Architectures for Signal Processing*, vol. 696, pp. 102–109, Aug 1986.

[78] D. Astley, A. Swindlehurst, and B. Ottersten, "Spatial signature estimation for uniform linear arrays with unknown receiver gains and phases," *IEEE Transactions on Signal Processing*, vol. 47, pp. 2128–2138, Aug 1999.

[79] G. Frazer, Y. Abramovich, and B. Johnson, "MIMO based spatial calibration of OTHR transmit arrays," in *2009 International Radar Conference - Surveillance for a Safer World*, pp. 1–5, Oct 2009.

[80] C. Balanis, *Antenna Theory: Analysis and Design*. Hoboken, New Jersey: John Wiley and Sons, Inc., third ed., 2005.

[81] C.-Y. Tseng, D. Feldman, and L. J. Griffiths, "Steering vector estimation in uncalibrated arrays," *Signal Processing, IEEE Transactions on*, vol. 43, no. 6, pp. 1397–1412, 1995.

[82] J. Capon, "High-resolution frequency-wavenumber spectrum analysis," *Proceedings of the IEEE*, vol. 57, no. 8, pp. 1408–1418, 1969.

[83] N. Wiener, *Extrapolation, Interpolation, and Smoothing of Stationary Time Series: With Engineering Applications*. Wiley, 1949.

[84] J. Yu and J. Krolik, "Multiband chirp synthesis for frequency-hopped fmcw radar," in *2009 Conference Record of the Forty-Third Asilomar Conference on Signals, Systems and Computers*, pp. 1315–1319, Nov 2009.

[85] J. Yu, M. Reynolds, and J. Krolik, "An indoor s-band radar receive array testbed," in *2010 IEEE Radar Conference*, pp. 712 –717, May 2010.

[86] J. Yu and J. Krolik, "Quadrature slow-time MIMO radar with experimental results," in *2010 Conference Record of the Forty-Fourth Asilomar Conference on Signals, Systems and Computers (ASILOMAR)*, pp. 2134–2137, Nov 2010.

[87] J. Yu and J. Krolik, "MIMO multipath clutter mitigation for GMTI automotive radar in urban environments," in *IET International Conference on Radar Systems (Radar 2012)*, Oct 2012.

[88] J. Yu, M. Reynolds, and J. Krolik, "Adaptive baseband interference suppression in multi-channel heterodyne radar receivers," in *IET International Conference on Radar Systems (Radar 2012)*, Oct 2012.

[89] J. Yu and J. Krolik, "Adaptive phase-array calibration using MIMO radar clutter," in *2013 IEEE Radar Conference*, May 2013.

[90] L. Li, J. Yu, and J. Krolik, "Software-defined calibration for FMCW phased-array radar," in *2010 IEEE Radar Conference*, pp. 877 –881, May 2010.

[91] J. Yu, M. Reynolds, and J. Krolik, "A software-defined MIMO radar testbed," in *14th ONR/GTRI Workshop on Target Tracking and Sensor Fusion*, Jun 2011.

[92] J. Yu and J. Krolik, "MIMO adaptive beamforming for non-separable multipath clutter mitigation," *submitted to IEEE Transactions on Aerospace and Electronic Systems*.

[93] J. Yu and J. Krolik, "Clutter-based adaptive MIMO phased array calibration," *to be submitted to IEEE Transactions on Antennas and Propagation*.

Biography

Jason Yu was born in Winchester, Massachusetts, United States, on January 18, 1985. He earned the B.S.E.E. degree from Tufts University in May 2007. Following his undergraduate career, he began graduate study at Duke University in the Department of Electrical and Computer Engineering under the direction of Dr. Jeffrey Krolik. He earned the M.S. degree from Duke University in May 2009, and the Ph.D. degree from Duke University in December 2013. He won the Charles Rowe Vail Memorial Outstanding Graduate Teaching Award for the 2009-2010 academic year from Duke University. In the summer of 2009, he worked at the Naval Research Laboratory in Washington, DC, as a student co-op in the Advanced Radar Systems Branch. Following his graduate career, he will begin a full-time technical staff position at the MIT Lincoln Laboratory in Lexington, Massachusetts.

His publications include six first author conference proceedings [84–89], one second author conference proceeding [90], one workshop presentation [91], and two journal publications pending review [92, 93].